INVESTIGATION OF ELECTROSTATICALLY DRIVEN MICRO ACTUATORS

Xiaohong Mu

A Thesis

in

The Department

of

Electrical and Computer Engineering

Presented in Partial Fulfillment of the Requirements

for the Degree of Master of Applied Science at

Concordia University

Montreal, Quebec Canada

November 2003

Your file Votre référence
ISBN: 0-612-91091-1
Our file Notre référence
ISBN: 0-612-91091-1

ABSTRACT

Investigation of Electrostatically Driven Micro Actuators

Xiaohong Mu

As the development of fiber optic communications, Micro electro mechanical system (MEMS) technology has been one of the most promising technologies to create optical components. MEMS devices have a number of advantages, such as small size, low power consumption, etc. However, more works and researches need to be done to improve the reliability, lifetime and functionality of these devices. The focus of this project is to investigate the fundamental mechanical and physical properties of simple microstructures utilized in typical MEMS devices.

In this project, an electrostatically driven micro actuator comprising a micro plate and a cantilever beam associated with thin film stresses is designed. The individual parts of the device are modeled and designed. First of all, the mechanical and physical effect of thin film stresses on the cantilever beam is modeled and simulated. Then the electrostatic and mechanical properties of the cantilever beam and the micro plate are investigated. In order to verify our results with practical devices, the proposed devices are fabricated using standard surface micromachining process, MUMPs technology, followed by post-processing technology. Experimental results and observations prove the modeling and simulation results are in good agreement with the experimental results. Furthermore some improvements and modifications of the fabricated devices are proposed for future research.

ACKNOWLEDGEMENTS

First of all I wish to express my sincere gratitude to my supervisors, Dr. Leslie Landsberger and Dr. Mojtaba Kahrizi, without their enlightenment, their knowledge, their encouragement and their invaluable instruction, I would never have completed this thesis.

Also I wish to express my truly appreciation to the faculty of Engineering and Computer Science at Concordia University, my schoolmates and my friends, specially Dr. Oleg Grudin for chip wire bonding, and Mr. Jun Chen for SEM photographing. All their assistances, their inspiration, their unselfish information sharing and valuable discussion made my project develop well.

Furthermore I want to thank Canadian Microelectronics Corporation (CMC) for MUMPs technology fabrication service, and financial support of National Sciences and Engineering Research Council of Canada (NSERC). Their generous help is essential to the completion of my project.

Finally I would like to thank my wonderful wife and my parents. Specially my wife, without her encouragement, her consistent patience and endless understanding, I would have never achieved my research and my study.

TABLE OF CONTENTS

List of Figures

List of Tables

Chapter 1 Introduction

1.1 The Introduction of Micro-Electro-Mechanical Systems (MEMS)

Micro-Electro-Mechanical Systems (MEMS) is a process technology used to create tiny integrated devices or systems that combine mechanical and electrical components. They are fabricated using microfabrication and micromachining process techniques and can range in size from a few micrometers to millimeters. MEMS has been identified as one of the most promising technologies for the 21st Century and has the potential to revolutionize both industrial and consumer products by combining silicon-based microelectronics with micromachining technology.

MEMS utilizes design, engineering and manufacturing expertise from a wide range of technical areas including integrated circuit (IC) fabrication technology, mechanical engineering, electrical engineering, material science, chemistry and chemical engineering, as well as optics, instrumentation and packaging. MEMS applications can be ranged from automotive, medical, electronic, communication and defence industry.

1.1.1 What is MEMS?

Micro-Electro-Mechanical Systems (MEMS) is the integration of mechanical elements, sensors, actuators, and electronics on a common substrate through the utilization of microfabrication and micromachining processes technology. MEMS, as an acronym, is originated in the United States. Now along with Microsystems Technology

(MST), started in Europe, MEMS is used everywhere. While the electronic devices are fabricated using IC technology, MEMS utilizes microfabrication and micromachining processes technology to produce complicated, multi-layer, three-dimensional (3D) structures which can range in size from a few micrometers to millimeters. MEMS system can interact with the physical and electronic world by MEMS devices such as sensors and actuators. While sensors have the ability to measure and acquire the physical properties categorized as mechanical, thermal, electrostatic, magnetic, acoustic and fluid energy domains, and then provide an electrical output signal in response to the information it acquired, actuators accept certain energy like electrical signals or thermal sources to actuate certain mechanical displacement, deflection or flexure. They can sense, actuate and control on the micro scale, but influence on the macro scale. While integrated circuits are designed to exploit the electrical properties of silicon, MEMS devices take advantage of both silicon's mechanical properties and its electrical properties. Fig. 1.1 shows the relationship between MEMS system and the physical world.

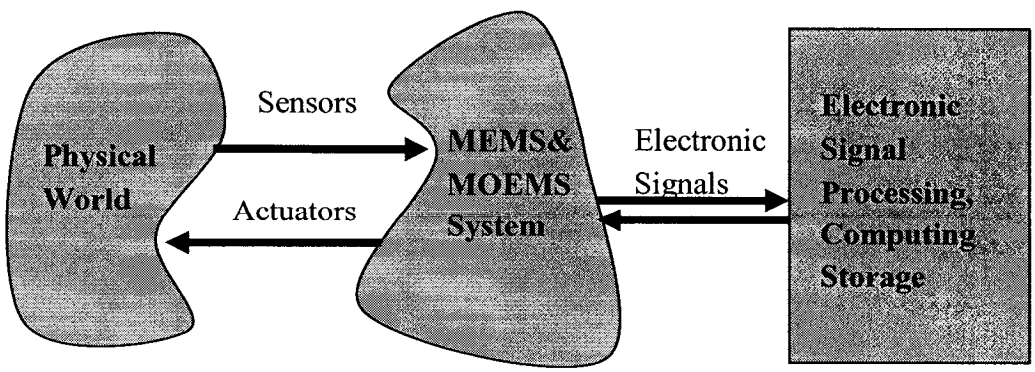

Fig. 1.1. MEMS system.

Figure 1.2 illustrates some of the key terminology and classifications associated with MEMS. MEMS is a technology used to create micro mechanical devices or systems. By definition, the term "MEMS" is more specific than MST. As a result, it is a subset of MST.

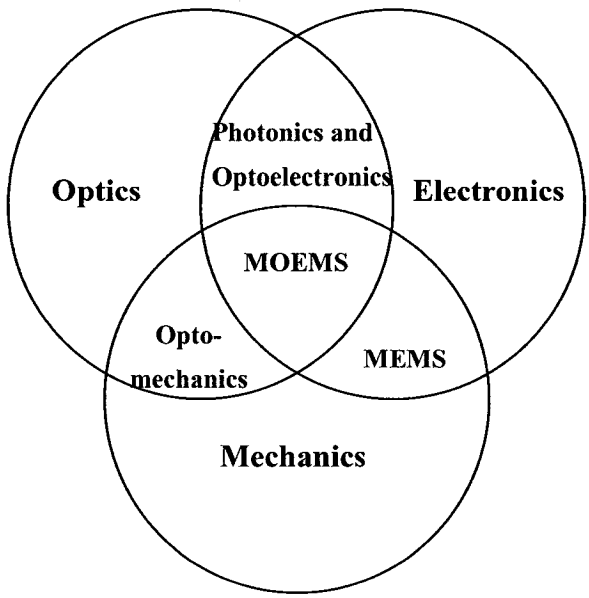

Fig. 1.2. Classifications of microsystems technology.

Micro-Opto-Electro-Mechanical Systems (MOEMS) is also a subset of MST and together with MEMS forms the specialized technology fields using miniaturized combinations of optics, electronics and mechanics.

1.1.2 MEMS System Design

The design of MEMS system requires several different levels of processes. On the one hand, the designer must define and document the applications and specifications for a proposed MEMS system, evaluate and compare the possibilities of different fabrication methods. On the other hand, for each proposed approach, one has to deal with details of

materials selection, corresponding fabrication sequence, packaging and assembly methods, and test and measurement means. A typical MEMS design flow is as follows:

(1) System requirements: the requirements include sensitivity, responsivity, reliability, frequency response, loss, and power consumption of the system. The modeling analysis is such simulation as optical simulation for optical systems.

(2) Device design: the designer selects different transduction mechanisms such as mechanical, electrostatic, thermal, magnetic and Electromagnetic, piezoelectric and fluidic mechanism for proposed devices. Meanwhile the devices should be verified to match system requirements. Analytical models and macro models could be built to simulate the designed devices.

(3) Implementation: this step focuses on how to fabricate the devices by such types of process techniques as bulk micromachining, surface micromachining, DRIE (Deep Reaction Ion Etching) or LIGA, whether custom process or standard foundry process will be used to fabricate, and what kind of materials will be chosen. Also, process integration should be decided. In this physical level, the designer can apply ANSYS or MEMSCAD software to implement Finite Element Analysis (FEA) or coupled domains FEA.

(4) Mask layout: build files to define technical properties including layers of materials, layer thickness, lithography, deposition or etching, and design rules; use layout tools, like Cadence, MEMSPro to layout masks by corresponding

technical files. Furthermore one can deploy design rules checking, 3D or cross section view and synthesis etc. process level simulation.

(5) Fabrication: when masks are ready, fabrication steps can be designed in cleaning room to fabricate the devices or devices are fabricated by industry foundry service. In addition, some postprocessing procedures must be performed for sacrificial layer release or other purposes.

(6) Test and reliability: the fabricated device will be observed and measured by specific test methods and test assembly. In addition, some experiments should be made to test the reliability of fabricated devices.

1.1.3 Developing History of MEMS

The developing history of MEMS illustrates its diversity, challenges and applications. The following list summarizes some of the key MEMS milestones[52].

- 1948: Invention of transistors (made from germanium).
- 1954: "Piezoresistive effect in Germanium and Silicon", C.S.Smith, Physical Review, 94.1, April 1954.
- 1959: "There's Plenty of Room at the Bottom" – Richard Feynman gives a milestone presentation at California Institute of Technology.
- 1961: First silicon pressure sensor demonstrated (Kulite).
- 1967: Invention of surface micromachining. Description of use of sacrificial

material to free micromechanical devices from the silicon substrate.

- 1970: First silicon accelerometer demonstrated (Kulite).
- 1971: First capacitive pressure sensor (Stanford).
- Early 1980's: first experiments in surface micromachined silicon. – First electrostatic comb actuators - micropositioning disc drive heads.
- Late 1980's: micromachining leverages microelectronics industry and widespread experimentation and documentation increases public interest.
- 1982: LIGA Process is patented.1988: First MEMS conference.
- 1992: First micromachined hinge is created in UCLA – Hinge features make 3D microstructures and assembly possible.
- 1992: MCNC started the Multi-User MEMS Process (MUMPs) sponsored by Defense Advanced Research Projects Agency (DARPA).
- 1994: Deep Reactive Ion Etching (DRIE) technology is patented.
- 2000: MEMS optical-networking components become big business.

1.2 MEMS Fabrication Techniques

MEMS fabrication techniques such as bulk micromachining and surface micromachining selectively remove parts of the silicon or add additional structural layers to form the mechanical and electromechanical components. They use high volume IC-style batch processing that involves the addition or subtraction of 2D layers on a substrate

(usually silicon) based on lithography and chemical etching. As a result, the 3D aspect of MEMS devices is due to patterning and interaction of the 2D layers. Additional layers can be added using a variety of thin-film and bonding techniques as well as by etching through sacrificial layers. The more addition of independent structural layers, the more complex of MEMS system will be.

1.2.1 Silicon Wafer Processing Flow

MEMS fabrication generally uses a silicon wafer for the substrate to build microscale structures. The typical silicon wafer processing cycle involves the following process flows:

(1) Thin film deposition: The different thin films like photoresist, polysilicon, SiO_2, Si_3N_4, Al, Au, etc., are deposited by a variety of technologies such as LPCVD (low- pressure chemical vapor deposition), PECVD (plasma-enhanced CVD), PVD (physical vapor deposition), and sputtering, evaporation, electrochemical, electroplating.

(2) Pattern definition: Photolithography, UV lithography, electron beam lithography and X-rays Lithography Mask making are exploited to pattern the different films by masks.

(3) Removal – etching: The etching technology generally is classified as wet etching and dry etching. Wet etching includes isotropic and anisotropic etching;

whereas dry etching includes plasma etching, RIE (Reactive Ion Etching), and DRIE (deep RIE). They remove selectively parts of the films to form the mechanical and electromechanical structures.

The cycle usually repeats several times to build the proposed structure step by step.

1.2.2 Bulk Micromachining

Bulk micromachining is one of the most popular silicon micromachining technologies. It has been used in the fabrication of different microstructures since early 1960s. This type of micromachining selectively removes parts of material (typically the bulk silicon wafer) to realize micromechanical structures. The microstructures fabricated using bulk micromachining may cover the thickness range from submicron to full wafer thickness (200–500 μm), and the lateral size range from submicron to the lateral dimensions of a full wafer.

The bulk micromachining technique allows selectively removing significant amounts of silicon from a substrate to form membranes on one side of a wafer, and a variety of trenches, grooves holes, or other structures (Figure 1.3). The bulk micromachining technique can be divided into wet etching and dry etching according to the phase of etchants. Liquid etchants, almost exclusively replying on aqueous chemicals, are referred to as wet etching. Vapor and plasma etchants are referred to as dry etching. Materials typically used for wet etching include silicon dioxide and quartz, while dry

etching is typically used with silicon, metals, plastics and ceramics.

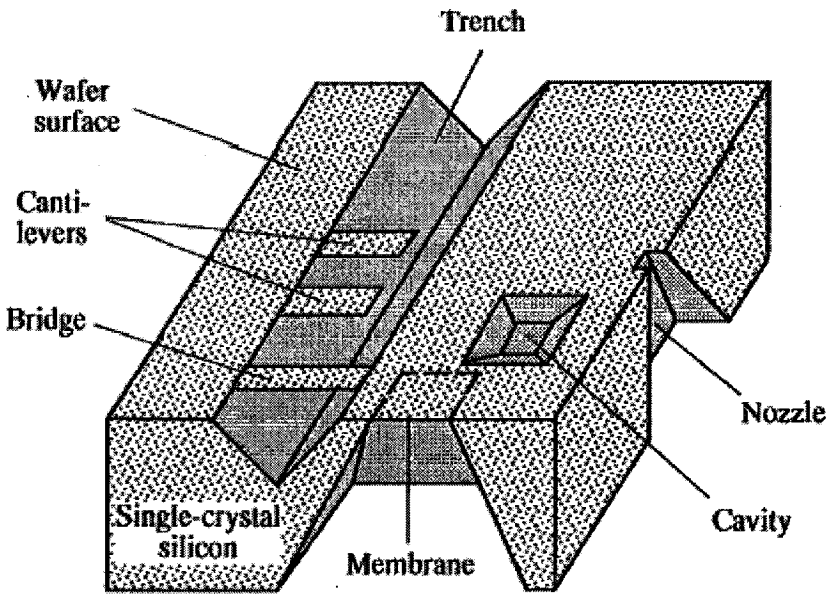

Figure 1.3. Various Bulk-micromachining structures [3].

Wet etching generally removes parts of silicon wafer through immersing it into an etching bath or spraying it with etchants. These etchants can either be isotropic or anisotropic depending on the structure of the materials or the etchants used.

Isotropic etching is always used when the material is amorphous or polycrystalline (Figure 1.4b). Isotropic etchants etch the material at the same rate in all directions, and consequently remove material under the etch masks at the same rate as they etch through the material. Isotropic etchants are limited by the geometry of the structure to be etched.

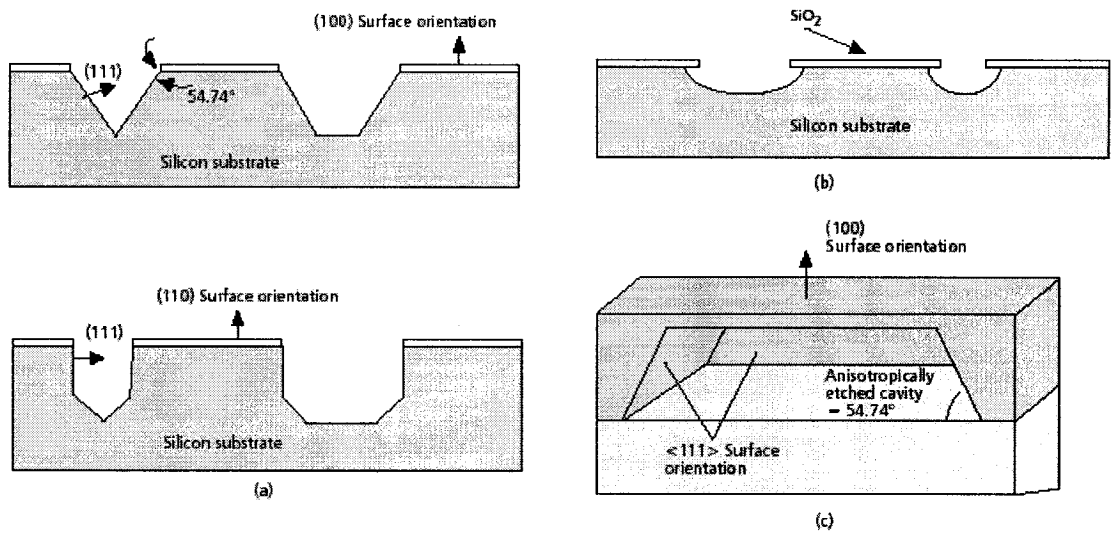

Figure 1.4. Bulk silicon micromachining. (a) Anisotropic wet etching of (100) and (110) silicon substrate, (b) Isotropical etching, (c) Deep cavity form in silicon by anisotropic etchants [28].

For etching thick silicon substrate, anisotropic etchants are typically chosen. Anisotropic etchants etch faster in a preferred direction (Figure 1.4a). Tetramethylammonium hydroxide (TMAH), Potassium hydroxide (KOH), ethylene diamine and pyrocatechol (EDP) are the most common anisotropic etchants. These etchants have different etch rates in different crystal orientation of the silicon [47,48], thus structural features formed in the substrate are dependent on the crystal orientation of the substrate. Most such anisotropic etchants progress rapidly in the crystal direction perpendicular to the (110) plane of silicon and less rapidly in the direction perpendicular to the (100) plane of silicon. Comparing with other planes, the etching slows down significantly at the (111) plane of silicon. With the chosen wafers with different crystal orientation, different bulk micromachined features can be achieved.

In most case wet etching is done from the backside of the wafer while the plasma etching is being applied to front side. In recent years, a vertical-walled bulk micromachining technique known as *SCREAM*, which is a combination of anisotropic and isotropic plasma etching, is used [49].

Dry etching occurs through chemical or physical interaction between the ions in the gas and the atoms of the substrate. It is classified as two methods: vapor phase etching and plasma-assisted etching.

Vapor phase etching uses vapor etchants such as xenon difluoride (XeF_2) or a mixture of interhalogen gases which provides highly selectivity for silicon, with no virtually attack of silicon dioxide, silicon nitride, metals (such as aluminum), and photoresist, etc.

The most common plasma-assisted etching is reactive ion etching (RIE). RIE utilizes external energy in the form of radio frequency (RF) power to drive the chemical reaction in low-pressure reaction chambers. The etching can occur at relatively low temperatures (typically 150° - 250°C, sometimes room temperature) than those usually needed (above 1000°C). RIE also has no silicon crystal planes limitation, thus deep trenches and pits, or arbitrary shapes with vertical walls can be etched [51].

The anisotropic dry etching processes are widely used in MEMS fabrication because of the geometrical flexibility and the less chemical contamination as compared with wet etching. Very deep silicon microstructures can be obtained by DRIE (deep

reactive ion etching) [50].

DRIE is a much higher-aspect-ratio etching method that involves an alternating process of high-density plasma etching and protective polymer deposition on side walls to achieve greater aspect ratios DRIE structures are featured as the increased capacitance for actuation and sensing, low-stress and highly stiff in vertical direction.

1.2.3 Surface Micromachining

Surface micromachining builds structures on the surface of the silicon by depositing thin films of 'sacrificial layers' and 'structural layers' and removing eventually the sacrificial layers to release the mechanical structures. The typical process steps of surface micromachining are shown in Figure 1.5. The dimensions of the surface-micromachined structures can be several orders of magnitude smaller than bulk-micromachined structures. Furthermore surface-micromachined structures are easy to integrate with IC components due to the same wafer working substrate and the compatible process technology for IC elements.

Surface micromachining requires a compatible set of structural materials, sacrificial materials, and chemical etchants. The structural materials must possess the physical and mechanical properties that are suitable for the desired application, for instances, high yield and fracture stresses, minimal fatigue, and good wire resistance. The sacrificial materials also need to have good mechanical properties to avoid device failure during

fabrication. These properties include good adhesion and low-residual stresses to eliminate device failure. The etchants used to remove the sacrificial materials must have excellent etch selectivity to etching off the sacrificial materials without affecting the structural ones. The common IC compatible materials used in surface micromachining are:

- Polysilicon / Silicon dioxide: LPCVD-deposited polysilicon as the structural material and LPCVD-deposited oxide as the sacrificial material. The oxide is readily dissolved in HF solution without affecting the polysilicon. Accompanying with this material system, silicon nitride is often used for electrical isolation. One of typical foundry services using this material system is MUMPs, which will be introduced later in this chapter.
- Polyimide / aluminum: polyimide is the structural material and aluminum is the sacrificial material. Acid-based etchants are used to dissolve the aluminum sacrificial layer.
- Silicon nitride / polysilion: Silicon nitride is used as the structural material, whereas polysilicon is the sacrificial material. For this material system, silicon anisotropic etchants such as KOH and EDP are used to dissolve polysilicon.

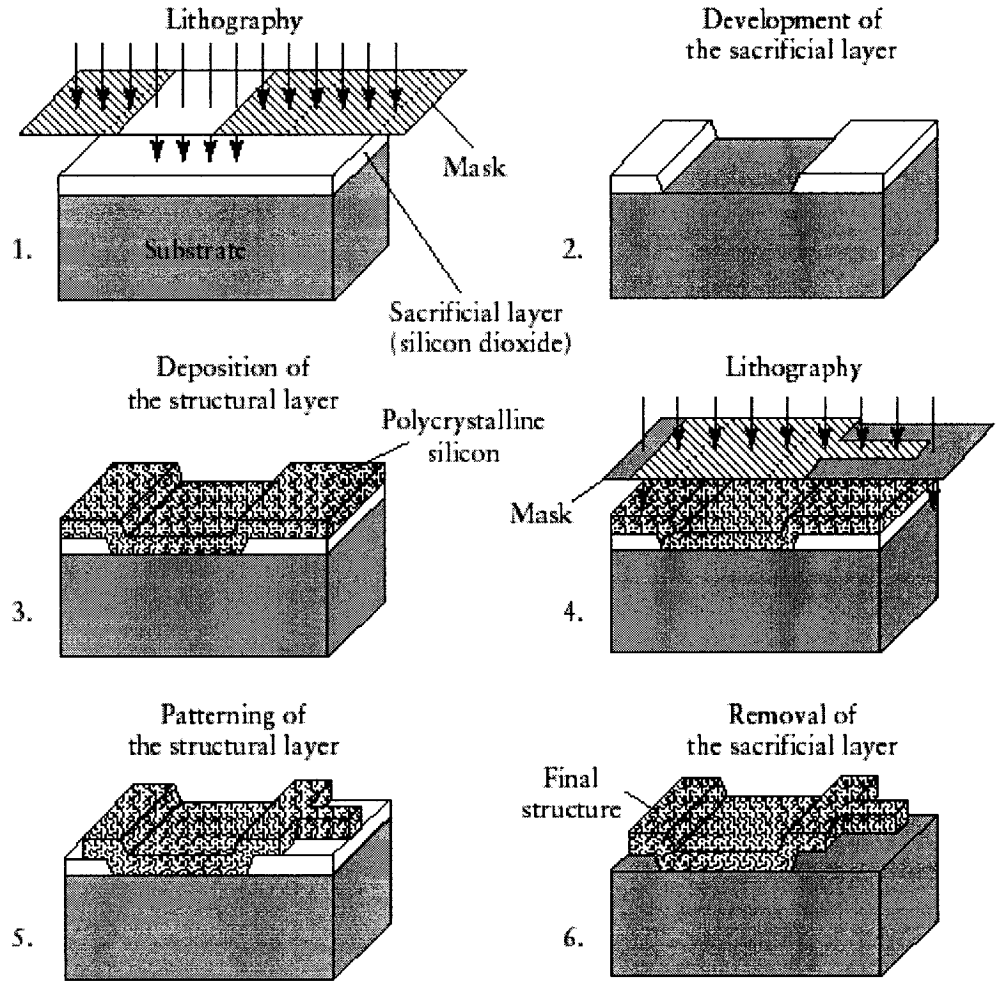

Figure 1.5. Process steps of typical surface micromachining [4].

Silicon microstructures fabricated by surface micromachining are usually planar structures (or two-dimensional). Other techniques involving the use of thin film structural materials released by the removal of an underlying sacrificial layer helps extending conventional surface micromachining into 3D dimension. By connecting polysilicon plates with substrate and with each other through microfabricated hinges [5], 3D micromechanical structures can be assembled after release. Another approach to 3D structures used the conformal deposition of polysilicon and sacrificial oxide films to fill

deep trenches previously etched in the silicon substrate. An example of the 3D-micromechanical structures fabricated using modified surface micromachining process is shown in Figure 1.6. These 3D microstructures are especially useful for optical microdevices without the requirement for contact power output.

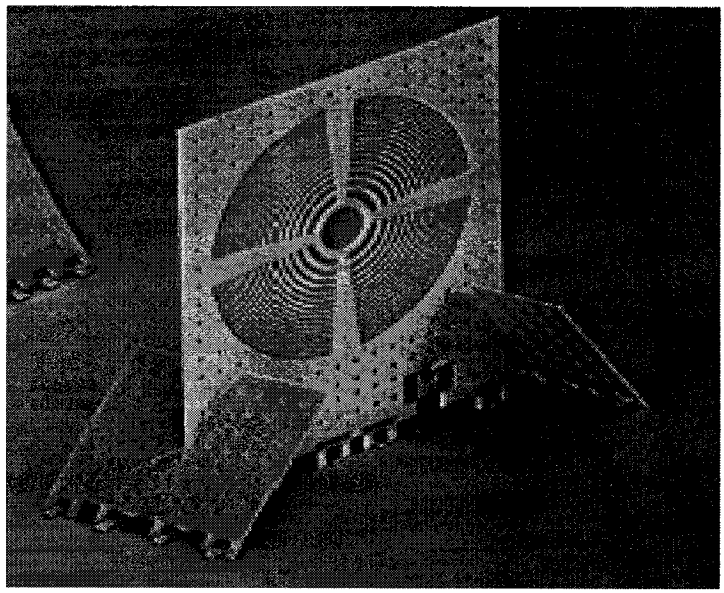

Figure 1.6. SEM of an out-of-plane micro-Fresnel lens [53].

In addition, wafer bonding technology can be used in forming multi-chip MEMS microstructures in a monolithic format which silicon micromachining has limitations in building [12]. Anodic bonding, intermediate-layer bonding-assisted bonding, and direct bonding are three major types of wafer bonding technology.

1.2.4 System Integration

Different approaches have been developed for the integration of the electronic

interface over the years. These include hybrid integration using conventional wire bonding and flip-chips and monolithic integration. Monolithic integration offers better system integration performance than hybrid systems although at an overall higher price in terms of involved technology and processing. Monolithic integration can be implemented in three ways:

- **IC fabrication before MEMS**

IC fabrication before MEMS integration system is relatively simple but mature. It relies mainly on bulk micromachining and the addition of new layers through electroplating (as shown in Fig. 1.7). The most challenge for this method is to reduce the residual stresses within the device materials. Thus refractory metals need to be used within the IC components in order to withstand the high temperature annealing cycles required to relieve the stress in polysilicon layer. An example using this technology is Texas Instrument's Digital Mirror Devices (DMD).

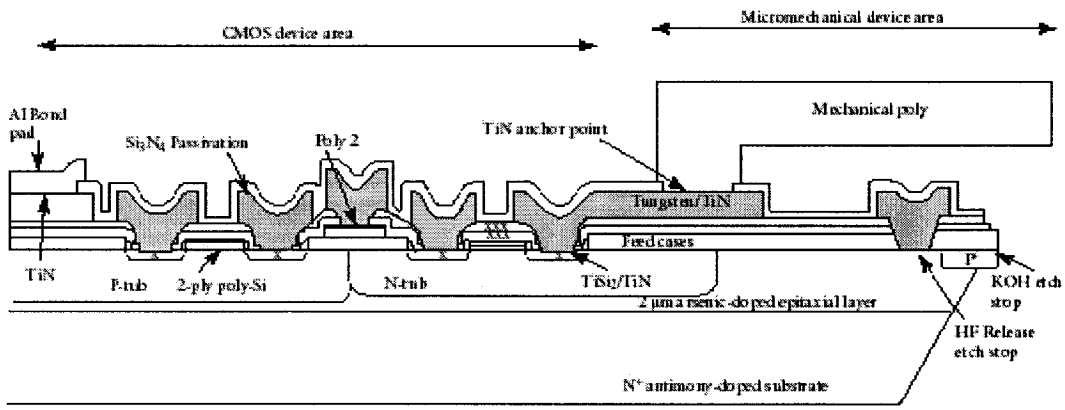

Figure 1.7. IC fabrication before MEMS [6].

- **Mixed MEMS-IC fabrication**

Monolithic mixed MEMS-IC fabricated process enables to build very compact but highly reliable structures at a very low cost. The tradeoff of this method lies within its complexity due to potentially rigid and constrained process flow which require very high volumes.

- **MEMS fabricated prior to IC**

The most promising monolithic integration technique includes fabricating the MEMS device prior to the microelectronics (as shown in Fig. 1.8). iMEMS (Integrated Microelectromechanical Systems) technology patented by Sandia National Laboratories, USA, is the technology by which MEMS components are fabricated in trenches on a silicon substrate and then the standard electronics are processed onto the same substrate.

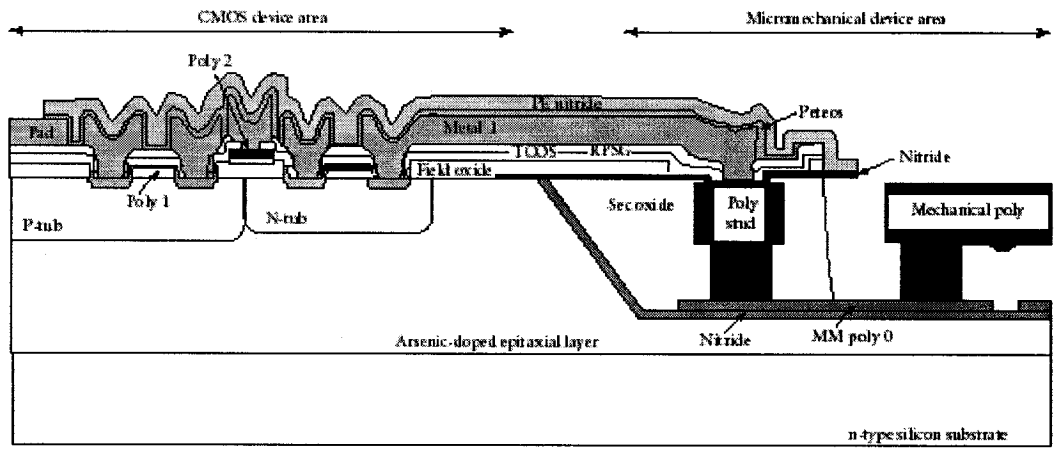

Figure 1.8. MEMS fabrication before IC [6].

1.3 MEMS Applications in Optical Communications

MEMS technology is extensively applied in a variety of fields. In communication fields, specifically optical communication field, MEMS has been a promising technology to create and build optical components and optical networking. In this field, MEMS technology generally is referred to be MOEMS.

As Internet rapidly prevails in recent years, demands on network resources are extremely increasing. Optical communications has emerged as the few practical means to resolve the issue of shortage of network capacity. Current data switching and routing technology restricts the information (or bit) flow by transforming optical signals into electronic information and then back into light before redirecting and transferring them. All optical networks offer far superior throughput capabilities and performance over traditionally electronic networks.

The most significant MOEMS device products include optical switches, VOA (Variable Optical Attenuators), cross connects, multiplexers, filters, modulators, detectors, and equalizers. Fig. 1.9 shows some optical MEMS devices applied in fiber optic communications. They are commonly featured as small size, low cost, low power consumption, mechanical durability, and high accuracy properties. That makes MOEMS technology an advanced solution to the problems of transfer, control and switching of optical signals in fiber optic communications.

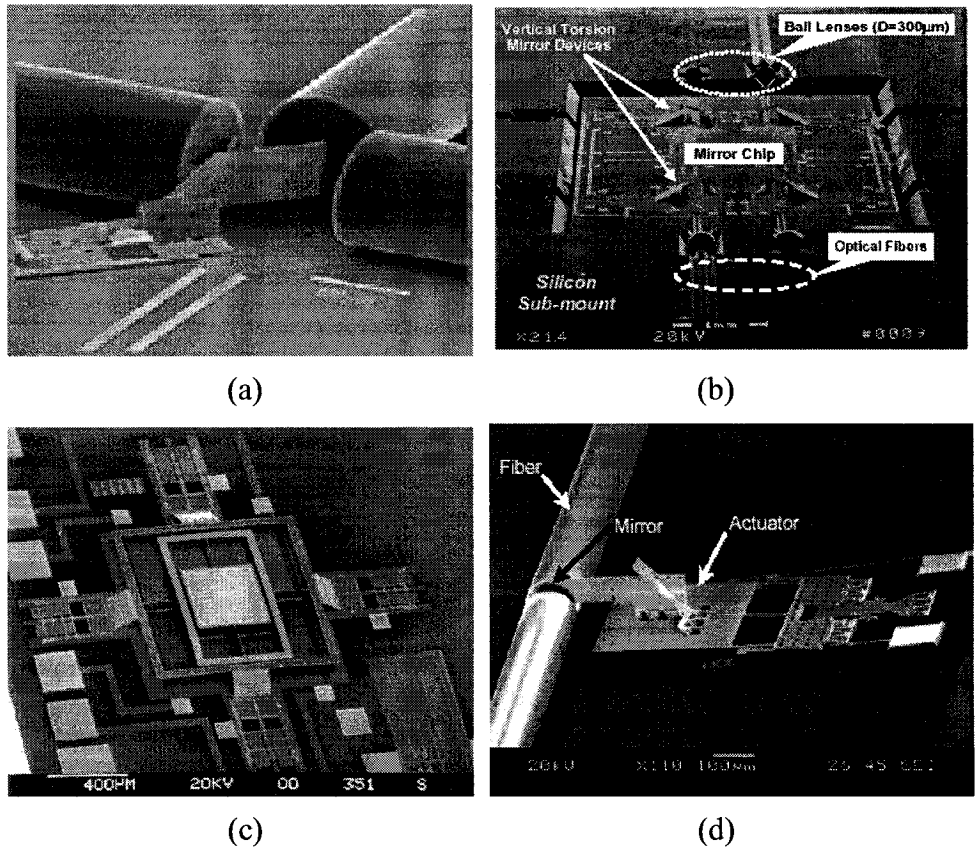

(a) (b)

(c) (d)

Figure 1.9. Some optical MEMS devices. (a) 1x2 optical switch [7], (b) 2x2 optical switch [8], (c) Bending switch for Variable optical attenuator (VOA) [9], (d) MEMS VOA [10].

VOA is one of the important components in fiber optic communications. Its main applications include power equalization in optical networks, shuttering and power control of Lasers and receivers, dynamic gain equalization (both channel or band level), and gain-tilt control in optical amplifiers. By far there are several technologies used to create the VOAs. They include MOEMS technology, liquid crystal technology [42], and acousto-optic technology [43][44]. Compared with other technologies, MEMS VOA devices can handle wide temperature variations encountered in the field, and have

advantages of low insertion loss, low power consumption, low polarization dependence loss, microsecond order switching speed (response time) and small package size.

1.4 MUMPs Foundry Services

Standard IC foundries perform one or two standard processes, whereas a MEMS foundry performs a wide variety of processes.

One of the most important MEMS foundries is called Multi-user MEMS Processes (MUMPs) technology, derived from Berkeley Sensors and Actuators Center (BSAC) at University of California in the late 80's and early 90's, developed by Cronos Integrated Microsystems of North Carolina sponsored by DARPA. In addition, there are some others including SUMMiT technology, developed and operated by Sandia National Laboratories, USA, and Metal Oxide Implementation Service (MOSIS) from the Information Sciences Institute at University of Southern California.

MUMPS is a three-layer polysilicon surface micromachining process. The process consists of 7 physical levels and 8 lithography levels. The physical levels are composed of a non-patternable nitride isolation layer, a ploysilicon ground (plane) layer (Poly 0), two structural ploysilicon layers (Poly 1 and Poly 2), two oxide release layers (PSG) and one metal layer for electrical connection and reflectivity enhancement. Table 1.1 lists MUMPs physical layers, thickness and lithography level name associated with those layers. Table 1.2 outlines 8 photomasks corresponding to 8 lithography levels and

purposes associated with these levels, and 4 hole masks for release convenience purpose. The light field indicates that the features drawn will stay after fabrication, whereas the dark field indicates that the holes drawn will be cut out during fabrication.

Table 1.1. MUMPs process layers, thickness and lithography level

Physical Layer	Thickness (μm)	Lithography level name
Nitride	0.6	--
Poly 0	0.5	POLY0 (HOLE0)
First Oxdie	2.0	DIMPLE and ANCHOR1
Poly 1	2.0	POLY1 (HOLE1)
Second Oxide	0.75	POLY1_POLY2_VIA and ANCHOR2
Poly 2	1.5	POLY2 (HOLE2)
Metal (Cr / Au)	0.5	METAL (HOLEM)

Table 1.2. MUMPs process photomask conventions and purposes

Mask name	Field type	Purposes
POLY0	Light	Patten ground plane
ANCHOR1	Dark	Open holes for Poly 1 to Nitride or Poly 0 connection
DIMPLE	Dark	Create dimple/bushings for Poly 1
POLY1	Light	Pattern Poly1 layer
POLY1_POLY2_VIA	Dark	Open holes for Poly 1 to Poly 2
ANCHOR2	Dark	Open holes for Poly 2 to Nitride or Poly 0 connection
POLY2	Light	Pattern Poly 2 layer
METAL	Light	Pattern metal layer
HOLE 0	Dark	Provide holes for Poly 0
HOLE 1	Dark	Provide release holes for Poly 1 layer
HOLE 2	Dark	Provide release holes for Poly 2 layer
HOLEM	Dark	Provide release holes for metal layer

Figure 1.10 (a) shows the cross section of an electrostatic motor fabricated by the MUMPs process. This device includes all the layers that are available in the MUMPs

process. In order to make the process as general as possible, MUMPs process defines all the layers' thickness and their functions. All MEMS designers have to follow these definitions and design rules. These definitions and design rules limit the designers to design more complex devices, but they make it possible for many different designs to be put on a single silicon wafer in one single fabrication process. Also, the standardization of the fabrication process reduces the fabrication cost and lets more and more designers submit their designs. All the microstructures presented in this thesis are fabricated by MUMPs technology. We will describe the details of MUMPs processes in Chapter 3.

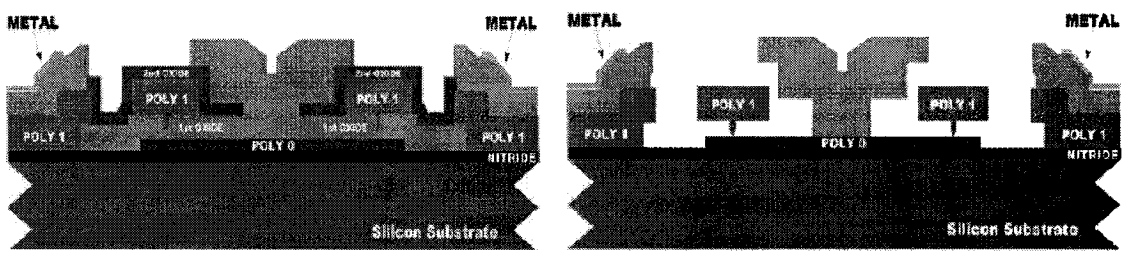

(a) (b)

Figure 1.10. Cross section of MEMS micromotor fabricated by MUMPs. (a) Before release, (b) After release [2].

The final unreleased structure is shown as Fig.1.10 (a). Then the chips can be performed post-processing – HF release to release the structural layers. Figure 1-10 (b) shows the device after sacrificial oxide release.

1.5 The Present Project

As mentioned in Section 1.3, MEMS technology has been extensively applied in

optical devices. A number of optical MEMS devices have been designed and fabricated under lab and industry environment. Although optical MEMS devices have lots of very competitive advantages over traditional optical devices, there also exist some problems in general MEMS devices, such as the stability, repeatability, and resistance against interference of outdoor environment.

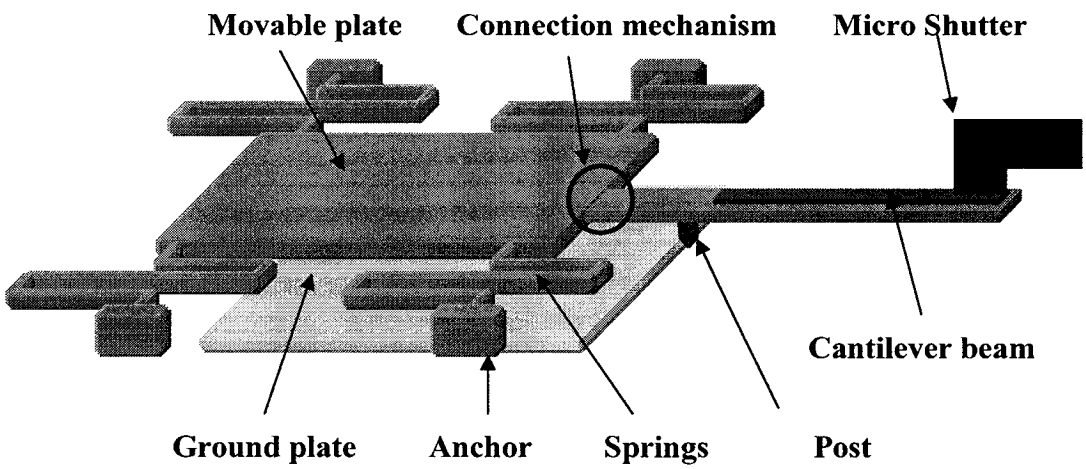

Figure 1.11. Schematic of electrostatically driven micro actuator.

In our project, we focus on the fundamental mechanical and physical properties of an electrostatically driven micro actuator, comprising a micro plate and a cantilever beam associated with thin film stresses. The minimum feature size of the proposed device will be a few microns. The device will be fabricated by a standard surface micromachining process - MUMPs process technology, followed by post-processing technology. Based on this constraint, all of the designs will have to follow the design rules of MUMPs process technology. Fig. 1.11 shows the schematic of the proposed device.

We will investigate and analyze the mechanical and physical properties of the electrostatically driven micro actuator and its individual parts, a cantilever beam and a micro plate. Chapter 2 will focus on the design, modeling and simulation of the electrostatically driven micro actuator comprising the micro plate and the cantilever beam associated with thin film stress. The modeling and simulations of the effect of thin film stresses on the cantilever beam will be performed. Also the electrostatic and mechanical modeling and simulations of the cantilever beam and the micro plate will be presented. In Chapter 3, fabrication and post-processing of the proposed devices will be presented. MUMPs main processes will be introduced in detail in this chapter. Release phenomena will also be represented and discussed. In Chapter 4, we will report functional experiment results and experimental observations. Some analyses and discussions will also be presented. Finally in Chapter 5, the conclusions will be presented, the contributions will be listed, and some modifications will be proposed for improvement of the designed devices for the future work.

Chapter 2 Design, Modeling and Simulation of The Micro Actuator

In this chapter, we focus on the research of fundamental mechanical and physical properties of the electrostatically driven micro actuator. Attention is paid on the design, modeling and simulation of the micro devices. First, the proposed devices are designed and described. Then the main functional parts, such as the cantilever beam with thin film stresses and the micro plate are modeled and simulated by FEM.

2.1 Design of The Electrostatically Driven Micro Actuator

Fig. 2.1 shows the schematic of designed electrostatically driven micro actuator (after release). As shown in Fig. 2.1, the electrostatically driven micro actuator is composed of a movable plate suspended by 4 similar micro springs, the ground plate, the cantilever beam connected with movable plate by the connection mechanism such as micro hinges [22], and the micro shutter erected at the end of the beam. In addition, a post is designed underneath the cantilever beam to be the lever support. The micro actuator employs electrostatic force between the movable plate and the ground plate to make the movable plate move down and up, and thus actuate the end of the cantilever beam to move up and down by lever amplification mechanism. The thin film residual stresses are also applied to the cantilever beam to achieve preload flexure of the cantilever beam. The preload flexure and the movement of the end of the cantilever beam

both lead to the vertical movement of the micro shutter connected to the beam end. The vertical movement of the micro shutter can potentially achieve the functions of optical switch or optical attenuator. Fig. 2.1 illustrates the designed device after release. Comparing with Fig. 1.11, one can notice that the cantilever beam is curved upward by the preload flexure.

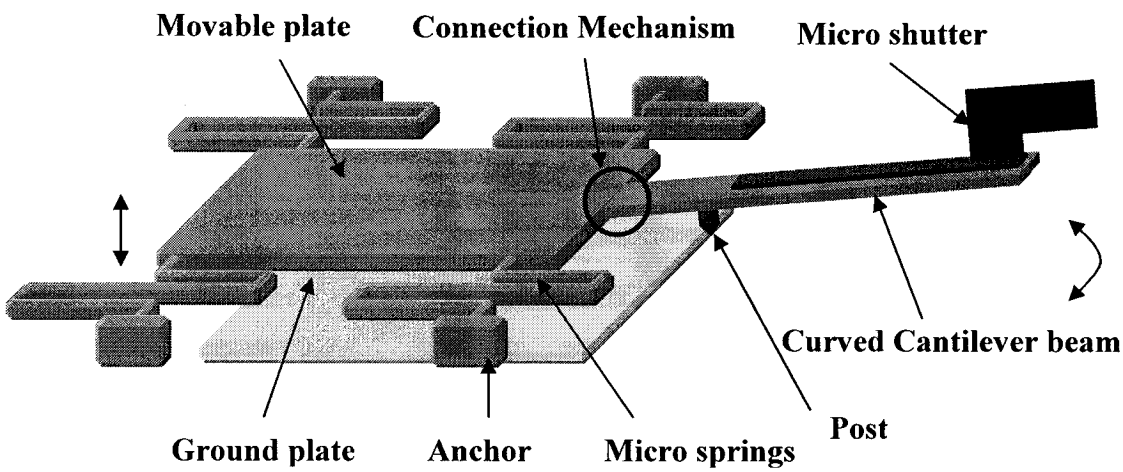

Figure 2.1. Schematic of electrostatically driven micro actuator (After release).

2.1.1 Design of The Micro Springs

Typically micro springs with lower spring constant are desired. From Equation (18) in Appendix A, we can realize that to make a spring with a lower spring constant, the spring has to be longer and thinner. Besides these, bending for torsion components and extra length and dimples can also lower spring constant. Unfortunately since the spring's bending motion is perpendicular to the substrate, according to the characteristics of MUMPs fabrication technology, its thickness can only have two alternatives, either 2 μm

thickness built by Poly1 or 1.5 μm thickness built by Poly2.

Based on above analysis, the micro springs have been designed as indicated in Fig. 2.2. Each micro spring is implemented as a couple of bars connected on alternating ends. At the beginning point and end of the spring is a "half-bar" so that the spring can be connected along its axis. All the spring bars are 4 μm wide, 4 μm gap spacing between the bars, and are structured by poly2 layer. The typical bar length of the spring is 120 μm.

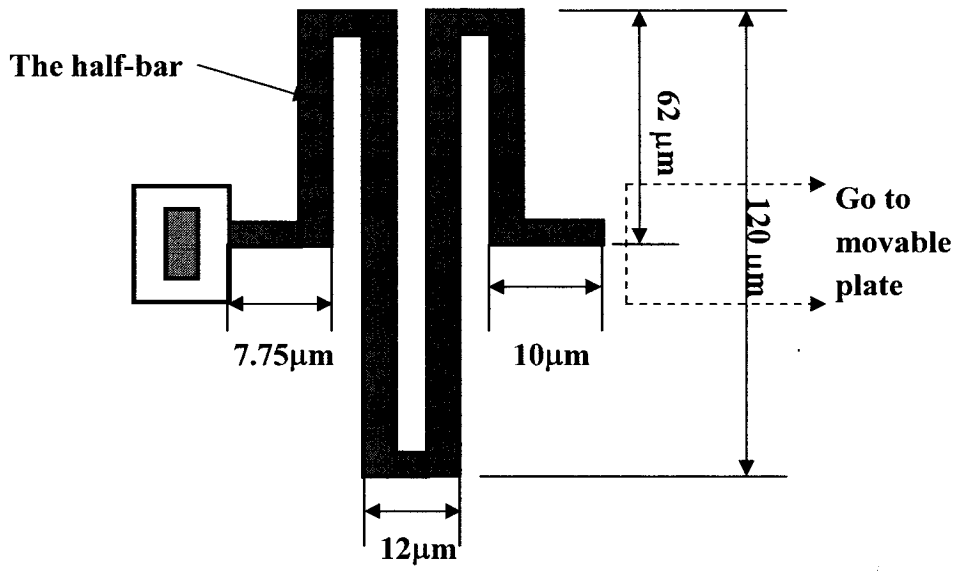

Figure 2.2. The typical geometry of designed micro springs (fabricated by Poly2 layer).

2.1.2 Design of Connection Mechanism Between plate and cantilever beam

As we described before, we tried to use lever amplification mechanism to amplify the end movement of the cantilever beam. The stiffer is the connection between the movable plate and the cantilever beam, the larger is the applied voltage needed to produce the initial actuation to move down the cantilever beam. Therefore, designing a

flexible connection mechanism is very necessary to effectively transfer the initial actuation of the movable plate to actuate the cantilever beam. In order to find out the better design method, several design methods were employed and presented for performance comparison.

The first design used three micro strips to connect the cantilever beam with the micro plate. The schematic of the micro strips is shown in Fig. 2.3. This design is simple and feasible but less flexible due to its fixed connection between the micro plate and the cantilever beam.

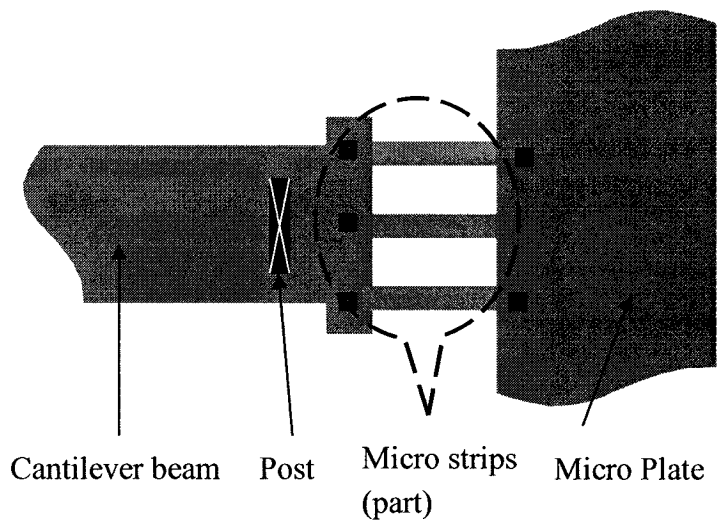

Figure 2.3. Micro strips designed for connection of micro plate and cantilever beam.

The second design used micro concaved-up scissor hinge [22] shown in Fig. 2.4. This design relatively separates the cantilever beam part from the micro plate part while it can flexibly pushes down the cantilever beam to effectively achieve the transfer of initial actuation. However the disadvantages of this design are the complexity and unsteadiness.

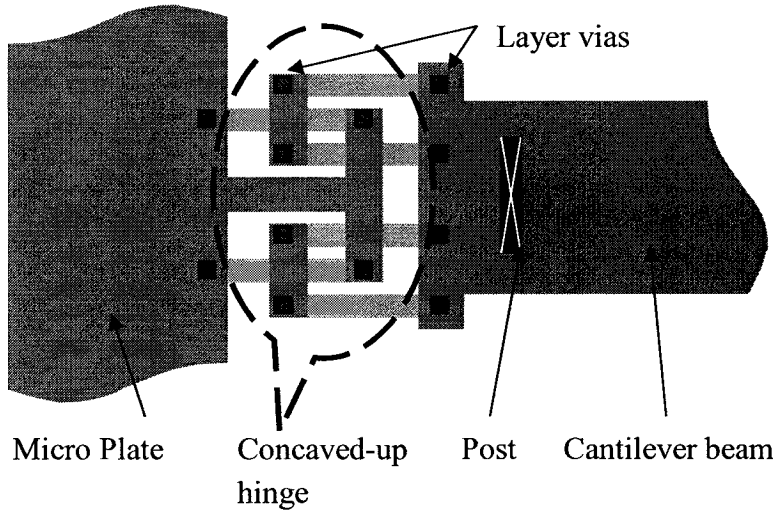

Figure 2.4. Concaved-up hinge designed for connection of micro plate and cantilever beam.

The third design is displayed in Fig. 2.5. It is simpler and less stiff than the first design, and reasonably lowers the weigh of the connections. However it is fragile and not very steady.

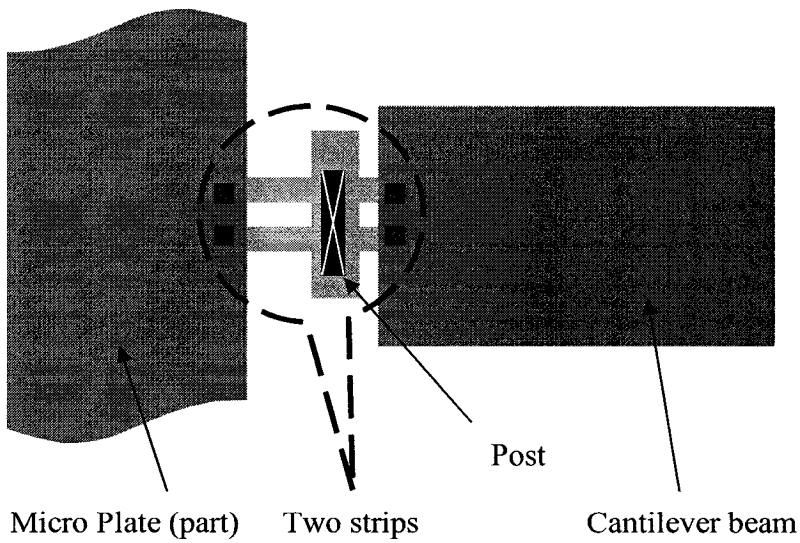

Figure 2.5. Two strips designed for connection of micro plate and cantilever beam.

2.1.3 Design of Connection Between Micro Shutter and cantilever beam

This part design is the challenging point of the whole design due to the technical constraints of MUMPs process technology. We use the same concaved-up micro hinge structure [22] as shown in Fig. 2.4 to connect the micro shutter with the cantilever beam. However, since this micro hinge structure will erect up to make the shutter stand up over the suspended cantilever beam after release, the geometries of the micro hinge should be small enough to prevent it from contacting the ground layer after it erects up. Meanwhile the design has to follow the MUMPs design rules. After trade-off between the MUMPs design rules and the basic functionality of the micro hinge, finally we complete this design. The micro shutter can be erected up by manual assembly, self-assembly, etc. different methods. Our micro shutter was designed to take manual assembly for its upright setup after release [26] [27].

2.1.4 Design of a Cantilever Beam with Thin Film Stress

In order to investigate the effect of thin film stresses on the cantilever beam, we design an independent cantilever beam associated with thin film stress. It is composed of a 1.5-μm thick poly structural layer and a 0.5-μm thick metal layer. Fig. 2.6 shows the 3-D view of the designed device.

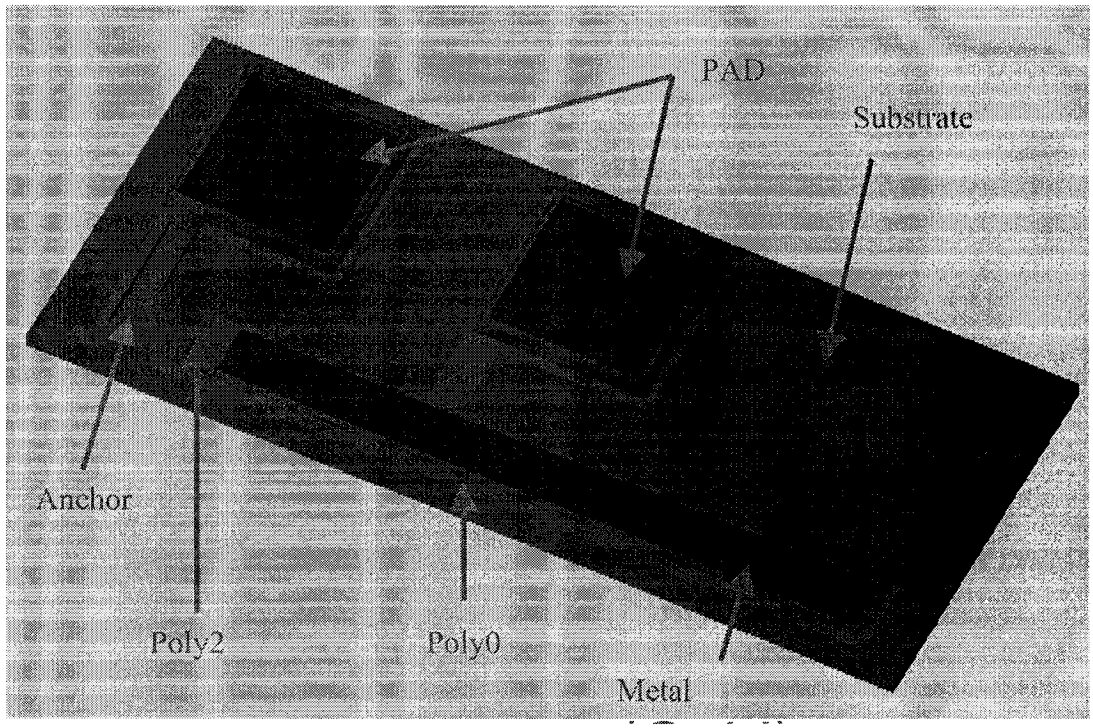

Figure 2.6. 3D view of designed cantilever beam from MEMSPro/L-edit.

The structure layer of the designed device is made of Poly 2 layer. A thin metal film is deposited atop the Poly 2 layer purposefully to investigate the effect of two thin film stresses. The whole structure layer is fixed on the Si substrate by an anchor. In order to electronically and mechanically isolate the main structure layer (Poly 2) from the ground layer (Poly 0), the dimples have also been designed. The schematic of the cross-section of the designed device is illustrated in Fig. 2.7.

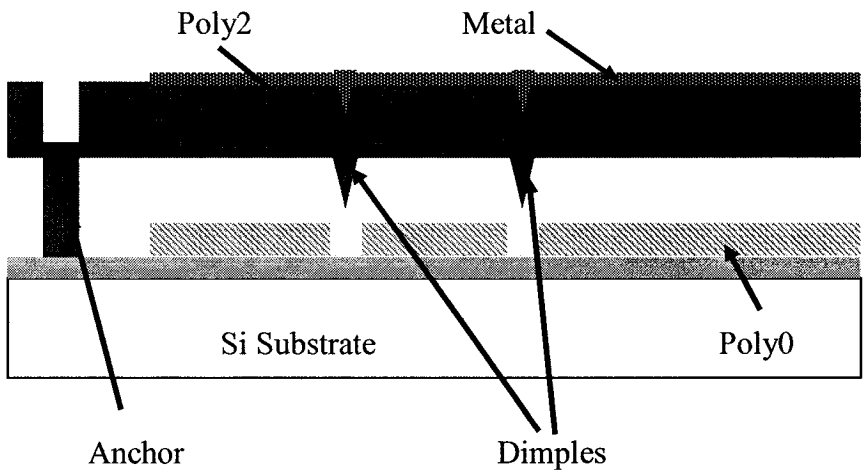

Figure 2.7. Cross-section of designed cantilever beam.

Table 2.1. Geometries matrix of the designed cantilever beam

Beam length (μm)	Beam width (μm)				
	30	40	50	60	80
400		Design			
455		Design			
505		Design			
555	Design	Design	Design	Design	Design
655		Design			
855		Design			

The designed geometries matrix of the cantilever beam is shown in Table 2.1. In total, we designed 10 cantilever beams with different geometric dimensions.

Finally we designed the micro plates with different geometric dimensions of length and width as 350 μm x 350 μm, 350 μm x 300 μm, 250 μm x 250 μm, 250 μm x 200 μm, 200 μm x 200 μm, 200 μm x 150 μm, and 150 μm x 200 μm.

2.2 Modeling and Simulation of the Cantilever Beam with Thin Film Stress

Due to typical features and microscopic scale of MEMS devices, thin film stresses could have severe influence on the functionality of the devices and on the reliability of MEMS structures. This section will model and simulate the effect of a cantilever beam associated with thin film stresses.

2.2.1 Thermal Expansion and Thin Film Stress [1]

Thermal expansion is an important thermomechanical effect. It indicates the tendency of a free body to increase in size as it is heated. The linear thermal expansion coefficient of a material is defined in terms of the rate of change of uniaxial strain with temperature, expressed as:

$$\alpha_T = \frac{d\varepsilon_x}{dT} \tag{2.1}$$

where α_T is thermal expansion coefficient, T is temperature.

When a thin film material is attached to a substrate, there will occur an extra strain, called thermal mismatch strain, which is the difference between the actual attached strain and strain the film would have if free. Accordingly, an in-plane stress is developed to achieve the special thermal mismatch strain.

If the thermal expansion coefficient of the film is smaller than that of the substrate, the net thermal mismatch stress has a negative sign, and is compressive stress; whereas,

when the thermal expansion coefficient of the film is larger than that of the substrate, the net thermal mismatch stress has a positive sign, is tensile stress. Tensile and compressive stresses simultaneously apply on the thin films of MEMS devices. If there is more tensile stress on the top surface of the thin film, it will curve upward; whereas, if there is more compressive stress on the top surface of the thin film, it will curve downward.

Thermal expansion mismatch is not the only source of in-plane stress. Chemical reactions occurring far from equilibrium can result in films that are highly stressed. In addition, modifications to a film's equilibrium structural properties by substitutional doping, mismatch of lattice spacing during epitaxial growth, or rapid deposition processes such as evaporation or sputtering can all result in thin film stress. Generally we call any stress in a thin film occurring after deposition a residual stress.

Residual stresses can have severe influence on the functionality of the devices and on the reliability of MEMS structures. For most MEMS devices we need to minimize or eliminate residual stresses in and between thin films, one of the methods is a thermal process called annealing. On the other hand, one can purposefully apply these differential stresses in adjacent thin films, such as polysilicon and metal layers, it can effectively lead to preload flexure of a micro cantilever beam, furthermore achieving dramatically out-of-plane microstructures by bending them into (potentially-desired) three-dimensional shapes.

2.2.2 Modeling of Thin Film Stress [15]

Provided there is a micro cantilever beam fabricated by MUMPs technology, whose polysilicon layers have a compressive residual stress while metal layers have a highly tensile residual stress. After post-processing, the released structure layer constructed by polysilicon and metal layers will bend upward.

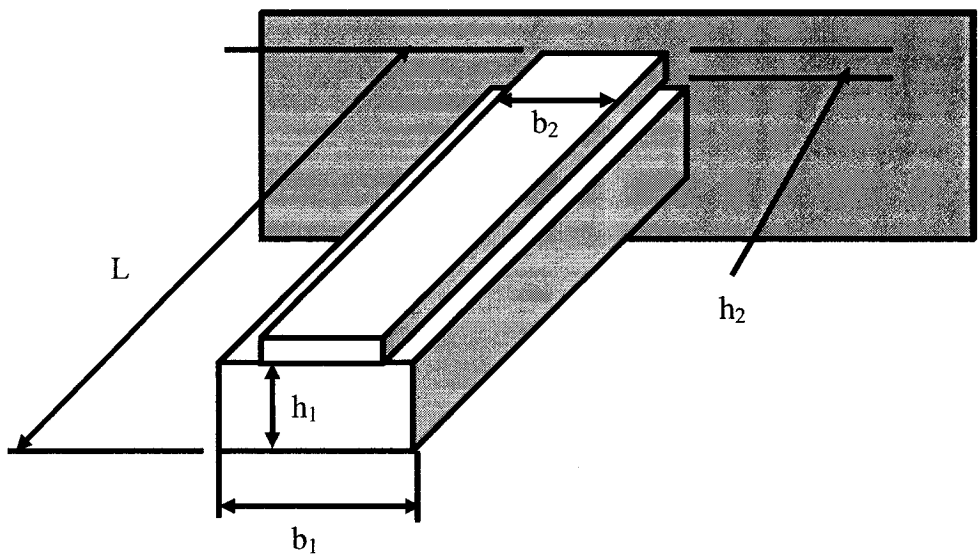

Figure 2.8. Schematic of a cantilever beam composed of two thin films.

Figure 2.8 shows a cantilever beam composed of two thin films with residual stress σ_1 and σ_2, and Young's modulus E_1 and E_2. The film thicknesses are h_1 and h_2, widths are b_1 and b_2, and the cantilever beam length is L.

Figure 2.9 shows the cross-section of a segment of cantilever beam along the length, and the forces and moments on two materials due to their internal stresses, where F_1 and F_2 are the stress induced forces.

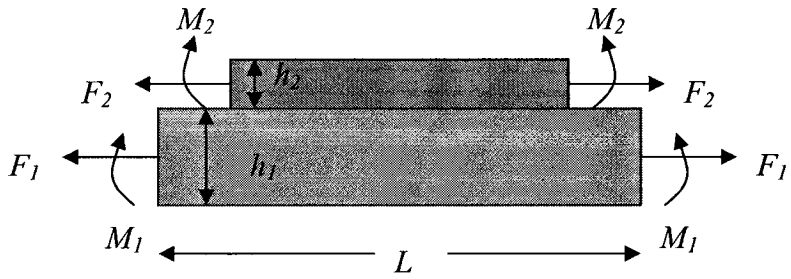

Figure 2.9. Cross-section of cantilever beam along length.

When two thin films with residual stresses share the same interface at equilibrium, the induced forces, F_1 and F_2, and the moments, M_1 and M_2, must balance:

$$F_1 = F_2 = F$$

$$\frac{F(h_1 + h_2)}{2} = M_1 + M_2 = M \tag{2.2}$$

Figure 2.10 shows the cross-section of the cantilever beam along the width. Considering two thin-film layers have no-uniform width values of b_1 and b_2 [16], a width factor $\beta = b_1/b_2$ is applied to modify the theoretical analysis. The moment of inertia can be derived from the parallel axis theorem [17]:

$$I = \frac{1 + 4m^*n + 6m^*n^2 + 4m^*n^3 + m^{*2}n^4}{12(1 + m^*n)} b_2 h_2^{\,3} \tag{2.3}$$

where $m^* = m \cdot \beta, m = E_1/E_2, \beta = b_1/b_2$, and $n = h_1/h_2$.

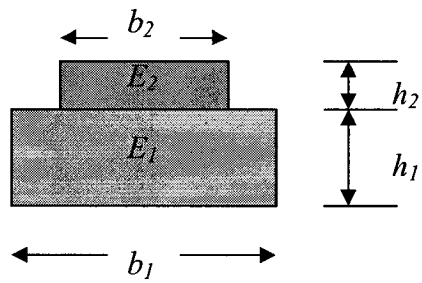

Figure 2.10. Cross-section of cantilever beam along width.

Instead of the moment-curvature relations for each material, an equivalent beam strength, $(EI)_{equiv}$ can be expressed as [54]:

$$(EI)_{equiv} = E_2 \frac{1 + 4m^*n + 6m^*n^2 + 4m^*n^3 + m^{*2}n^4}{12(1 + m^*n)} b_2 h_2^3 \tag{2.4}$$

From Equation (14) in Appendix A, we obtain

$$M = \frac{(EI)_{equiv}}{\rho} \tag{2.5}$$

where ρ is the radius of curvature of the beam. Therefore the relationship between the stress-induced internal forces and the radius of curvature of the cantilever beam can be obtained as

$$F = \frac{2(EI)_{equiv}}{\rho(h_1 + h_2)} \tag{2.6}$$

Since the two films share an interface, they maintain a zero slip condition at the interface. Therefore, the normal strains of material 1 and 2 are equal to each other, leading to:

$$\frac{\sigma_1}{E_1}+\frac{F}{E_1 h_1 b_1}+\frac{h_1}{2\rho}=\frac{\sigma_2}{E_2}-\frac{F}{E_2 h_2 b_2}-\frac{h_2}{2\rho} \tag{2.7}$$

where the first term is due to residual stresses σ_1 and σ_2, the second term is from the axial force F, and the last is from the beam curvature ρ.

Solving the problems using the equations (2.4), (2.6) and (2.7), the expression for the radius of curvature can be derived as

$$\frac{1}{\rho}=\frac{6\beta n(1+n)(m\sigma_2-\sigma_1)}{h_2 E_2\left[K+3m^* n(1+n)^2\right]} \tag{2.8}$$

where $K=1+4m^* n+6m^* n^2+4m^* n^3+m^{*2} n^4$.

The end deflection (δ) of the beam perpendicular to the pre-released position for a given length L can be obtained as:

$$\delta=\rho\left[1-\cos(\frac{L}{\rho})\right] \tag{2.9}$$

The resonant frequency of the switch built by a cantilever beam can be determined by the equation for a singly clamped cantilever beam expressed as [51]:

$$f_R=\frac{1}{2\pi}\sqrt{\frac{k}{m}}=\frac{1.03}{2\pi}\cdot\frac{h\nu}{L^2} \tag{2.10}$$

where $\nu=\sqrt{\frac{E}{\rho_D}}$, is longitudinal acoustic velocity, k is beam spring constant, m is beam mass in kg, h is beam thickness, L is the beam length, E is the Young's modulus of beam material, and ρ_D is the density of beam material.

2.2.3 Analytical Solutions and FEM simulations

According to Equation (2.8), the cantilever beam curvature ρ can be represented as following matrix expression:

$$\begin{pmatrix} \rho_1 \\ \rho_2 \\ \rho_3 \\ \mathrm{M} \\ \rho_n \end{pmatrix} = \frac{h_2 E_1 (1+n)}{2(m\sigma_2 - \sigma_1)} \begin{pmatrix} 1 \\ 1 \\ 1 \\ \mathrm{M} \\ 1 \end{pmatrix} + \frac{h_2 E_2}{6\beta n (1+n)(m\sigma_2 - \sigma_1)} \begin{pmatrix} K_1 \\ K_2 \\ K_3 \\ \mathrm{M} \\ K_n \end{pmatrix} \tag{2.11}$$

Similarly, from Equation (2.9), we can get the matrix expression of end deflection:

$$\begin{pmatrix} \delta_1 \\ \delta_2 \\ \delta_3 \\ \mathrm{M} \\ \delta_n \end{pmatrix} = \begin{pmatrix} \rho_1 \\ \rho_2 \\ \rho_3 \\ \mathrm{M} \\ \rho_n \end{pmatrix} - \begin{pmatrix} \rho_1 \\ \rho_2 \\ \rho_3 \\ \mathrm{M} \\ \rho_n \end{pmatrix} \bullet \left(\cos\left(\frac{L_1}{\rho_1}\right) \quad \cos\left(\frac{L_2}{\rho_2}\right) \quad \cos\left(\frac{L_3}{\rho_3}\right) \quad \Lambda \quad \cos\left(\frac{L_n}{\rho_n}\right) \right) \tag{2.12}$$

The mechanical property parameters of the materials are quite dependent on the fabrication process such as deposition, temperature, and time etc. In order to accurately model the designed device, the proper mechanical property parameters of poly and metal layers have to be determined. We chose typical mechanical property parameters for analytical solutions and modeling simulations. The parameter values and references are all listed in Table 2.2. Notice that some values used are reasonably within the range of the parameters presented by MUMPs foundry Cronos [2].

Table 2.2. Physical and Mechanical parameters of thin films for modeling

Films / Properties	Polysilicon [2][18]	Metal (gold)[19][20][27]
Thickness (μm)	2 (Poly1) or 1.5 (Poly2)	0.5
Young's Modulus (*Gpa*)	169	78.5
Residual Stress (*Mpa*)	-15	73
Poisson's Ratio	0.23	0.42
Density ($kg/\mu m^3$)	2.33×10^{-15}	1.93×10^{-14}
Sheet Resistance (Ω/square)	10 (Poly1) or 20 (Poly2)	0.06

It is known the metal layer is made of 500 nm *Au* (gold) layer with 200 nm adhesive layer of *Cr*. Nevertheless under specific temperatures (less than 200°C) the effect of *Cr* layer on beam curvature can be negligible compared with the effect of gold layer [21].

The designed devices are modeled and simulated by ANSYS finite element analysis. The material property parameters selected for ANSYS simulations are listed in Table 2.2. Simulation results of the beam end deflection are illustrated in Fig. 2.11 and Fig. 2.12 (The simulation program and some results are attached in Appendix B-1, B-2 and B-3).

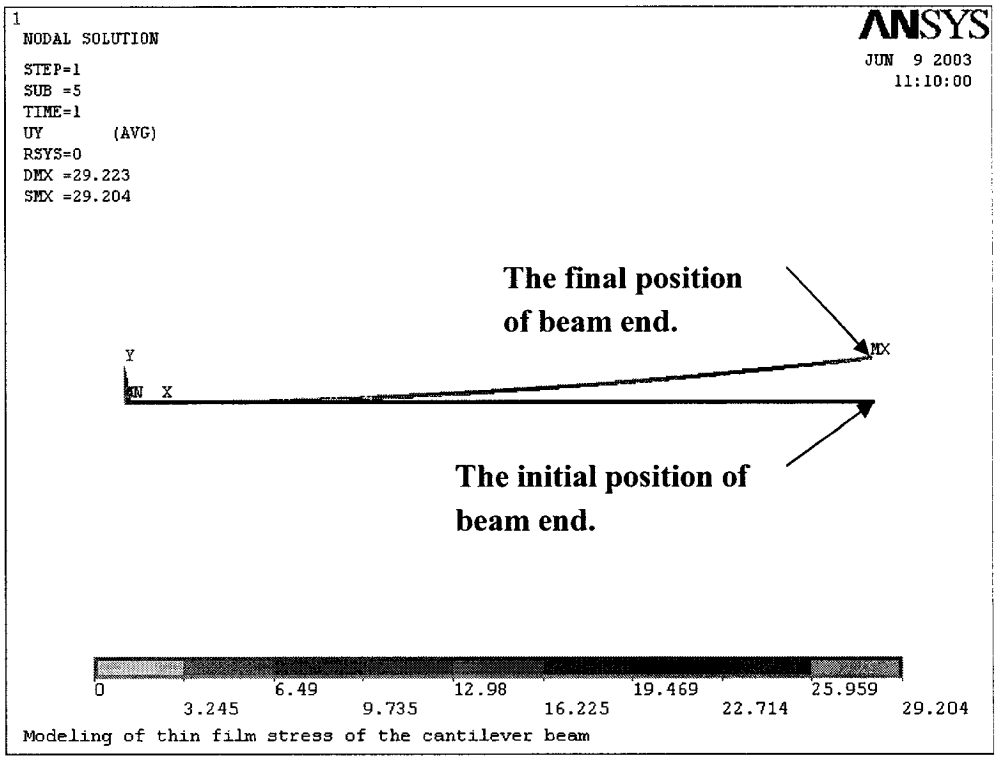

Figure 2.11. The simulation result of the end deflection of the cantilever beam by ANSYS.

The beam end deflection versus beam width & beam length determined analytically are shown in Fig. 2.12 and Fig. 2.13. From these figures, one can see that as the dimensions of the beam increase, beam end deflection increases. However, the end deflection increases much more rapidly with beam length increase than with beam width increase. For example, for 555 μm long beam, when the width of polysilicon increases from 40 to 60 μm, the end deflection increases only from 34.1 to 35.2 μm, or 3.2%; whereas for 40 μm wide beam, when the length of polysilicon increases from 455 to 555 μm, end deflection increases dramatically from 21.8 μm to 34.1 μm, or 56.4%.

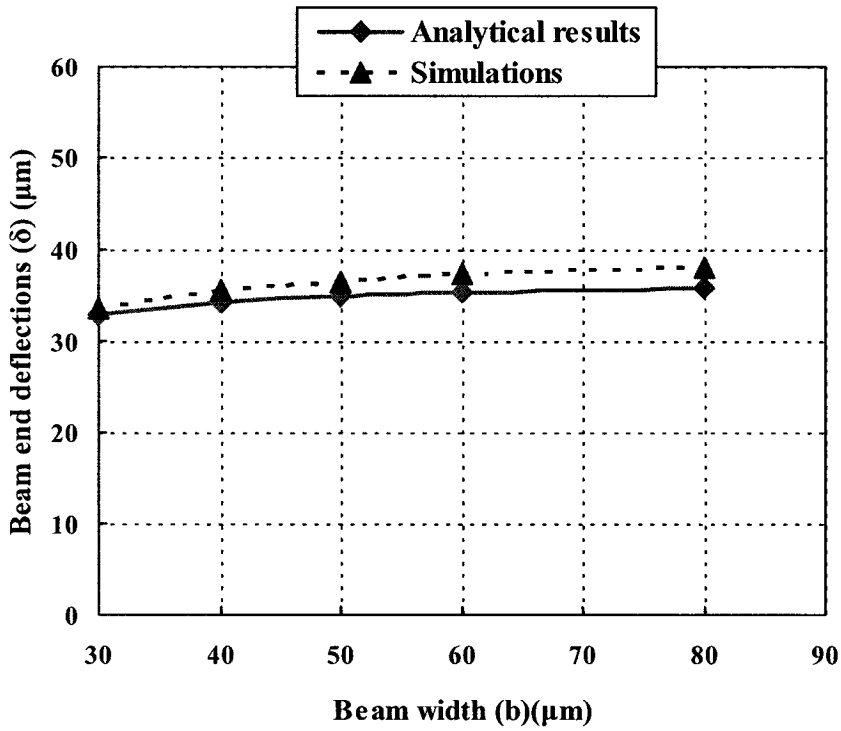

Figure 2.12. Comparisons of analytical results with simulation results under 555μm long beam.

Fig. 2.12 also illustrates the beam end deflection simulation results versus beam width whereas Fig. 2.13 illustrates the beam end deflection simulation results versus beam length. By comparison, one can figure out that simulation modeling correctly predicted the end deflection due to preload thin film residual stress. However, the beam end deflections determined by simulation are just a little bit higher than those obtained by the analytical solutions, even though both follow the same trends. The discrepancy could be attributed to simulation specification options, changing of aspect ratio of structure, physical and mechanical properties, etc.

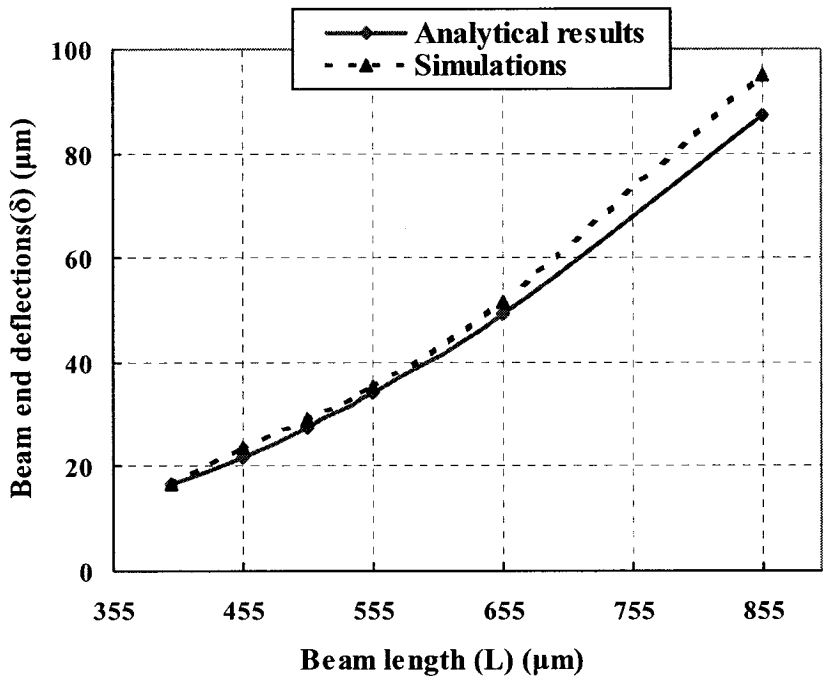

Figure 2.13. Comparisons of analytical results with simulation results under 40μm wide beam.

On the other hand, the discrepancy between the end deflections determined by simulation and those determined by analytical solutions are getting larger when the beam is getting longer, and particularly wider. The main reason is that as the length and width of the beam increases, the aspect ratio of the beam decreases, and then it is prone to alter the physical and mechanical properties of the structure. Therefore it may be better for people to choose a certain width of a beam and design different length of the beam for the different application purposes.

The analytical and modeling results of the beam end deflection under different geometries are listed in Table 2.3.

Table 2.3. Analytical and simulation results of the beam end deflection

Beam Length (μm)	*Metal length (μm)*	*Poly Width (μm)*	*Metal Width (μm)*	*Deflection (μm) (analytical)*	*Deflection (μm) (simulation)*	*Variation (%)*
400	350	30	22	16.145	15.896	1.5
		40	32	16.739	16.805	0.4
		50	42	17.068	17.321	1.5
		60	52	17.277	17.655	2.2
		80	72	17.528	18.066	3.1
455	400	30	22	21.082	22.308	5.8
		40	32	21.858	23.561	7.8
		50	42	22.288	24.269	8.9
		60	52	22.561	24.726	9.6
		80	72	22.888	25.282	10.5
505	450	30	22	26.675	27.405	2.7
		40	32	27.657	28.966	4.7
		50	42	28.200	29.845	5.8
		60	52	28.546	30.407	6.5
		80	72	28.959	31.066	7.3
555	500	30	22	32.924	33.517	1.8
		40	32	34.134	35.417	3.8
		50	42	34.805	36.489	4.8
		60	52	35.230	37.177	5.5
		80	72	35.740	37.979	6.3
655	600	30	22	47.380	48.836	3.1
		40	32	49.120	51.451	4.7
		50	42	50.083	52.981	5.8
		60	52	50.694	54.058	6.6
		80	72	51.427	55.257	7.4
855	800	30	22	84.094	90.195	7.3
		40	32	87.172	94.982	9.0
		50	42	88.875	99.432	11.9
		60	52	89.956	99.778	10.9
		80	72	91.251	101.996	11.8

2.3 Modeling and Simulation of The Micro Plate

2.3.1 Electromechanical Theories of The Micro Plate

Fig. 2.14 shows two parallel plates with applied voltage. The capacitance between

these two parallel plates (fringing fields are neglected) is given by

$$C = \varepsilon A / g \tag{2.13}$$

where A is the area of the capacitor plate, g is the gap spacing between the plates, ε is the permittivity of the material between the gap.

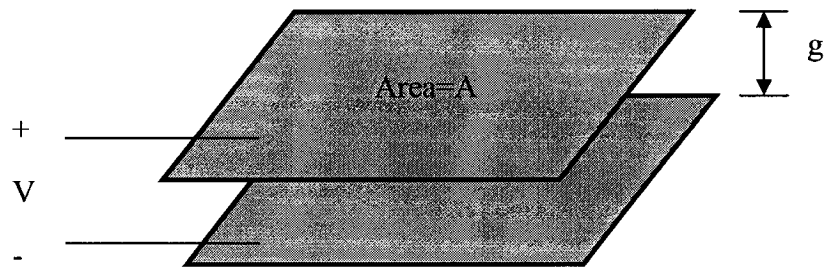

Figure 2.14. Schematic of a parallel plate capacitor.

(1) Voltage Control of Electrostatic Actuator

In general, the stored energy for a lumped capacitive element is [1]

$$W(q) = \int_0^q e(q)dq \tag{2.14}$$

where e is one conjugate power variables called effort, q is the deflection.

For the electrical capacitor, the store energy can be expressed as

$$W(Q) = \int_0^Q V dQ \tag{2.15}$$

In general, for a linear capacitor, we have $Q = CV$, leading to

$$W(Q) = \int_0^Q \frac{Q}{C} dQ = \frac{Q^2}{2C} = \frac{Q^2 g}{2\varepsilon A} \tag{2.16}$$

Energy (W) stored in a capacitor is a function of total charge, Q, and gap space, g.

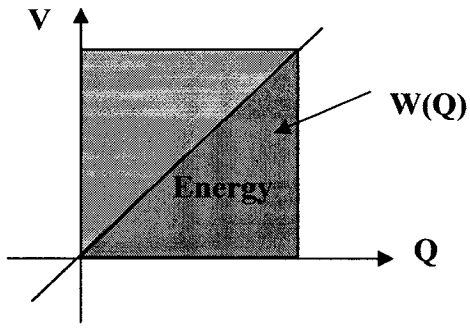

The basic definition of stored energy in each energy domain is expressed as $dW = F \cdot dg + V \cdot dQ$. Electrostatic force generated by the charge under constant charge condition is expressed by:

$$F = \left.\frac{\partial W(Q,g)}{\partial g}\right|_{Q}$$

leading to

$$F_{electrosta\,tic} = \frac{Q^2}{2\varepsilon A} \tag{2.17}$$

From Equation (2.17), one can notice electrostatic force is independent of gap (g) and proportional to the square of the charge (Q).

For the nonlinear capacitor, we use the co-energy of the system [1] instead of the energy to determine the electrostatic force (shown as Fig. 2.16). The purely electrical co-energy is defined as

$$W^*(V) = QV - W(Q)$$

Considering gap g is the mechanical domain independent variable, the co-energy

definition for the electrostatic domain can also be expressed as

$$W^*(V,g) = QV - W(Q,g)$$

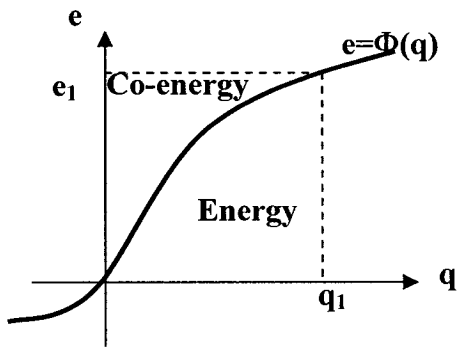

Nonlinear Capacitor

Figure 2.16. Schematic of energy systems stored in a nonlinear capacitor.

Differentially, it becomes

$$dW^*(V,g) = (Q \cdot dV + V \cdot dQ) - dW(Q,g)$$

Combining the given relationship $dW = F \cdot dg + V \cdot dQ$, one obtain

$$dW^*(V,g) = Q \cdot dV - Fdg \tag{2.18}$$

which leads to

$$F = -\left.\frac{\partial W^*(V,g)}{\partial g}\right|_V = \frac{\varepsilon A}{2} \cdot \left(\frac{V}{g}\right)^2 \tag{2.19}$$

Electrostatic force with voltage control is directly proportional to V^2 and inversely proportional to g^2.

(2) Pull-in Voltage of The Micro Plate

For electrostatically driven micro plate, pull-in voltage is one of the key properties. This section will present the basic analytical solutions of pull-in voltage.

Fig. 2.17 illustrates the schematic of a movable plate with a spring applied between it and the fixed support.

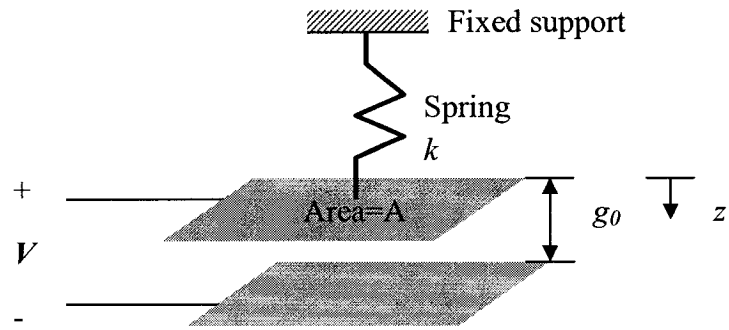

Figure 2.17. Schematic of a movable plate with a spring applied between it and the fixed support.

Where g_0 is the natural position gap (with zero spring force and zero capacitor charge), and z is the displacement of the movable plate.

From the characteristic of the spring, we have

$$F_{elastic} = kz \tag{2.20}$$

Under equilibrium, electrostatic force is balanced by elastic force and it leads to

$$kz = \frac{\varepsilon A}{2}\left(\frac{V}{g}\right)^2 \tag{2.21}$$

From gap between the parallel plates $g = g_0 - z$, one can derive

$$V = (g_0 - z)\sqrt{\frac{2kz}{\varepsilon A}} \tag{2.22}$$

Equation (2.22) can be solved to determine the required voltage for specific vertical displacement of the movable plate.

The voltage-controlled parallel-plate electrostatically driven micro plate exhibits a behavior called pull-in. The stability of the equilibrium must exist between the electrostatic force pulling the plate down and the spring elastic force pulling the plate up. Since the equilibrium gap decreases with increasing voltage, there will be a specific voltage value at which the stability of the equilibrium is lost. This is called pull-in voltage.

Specifically, we normalize the voltage to the pull-in voltage V_{PI} as

$$v = \frac{V}{V_{PI}} \tag{2.23}$$

and normalize the displacement of the moveable plate from its equilibrium position as

$$\varsigma = 1 - \frac{g}{g_0} \tag{2.24}$$

Fig. 2.18 shows the two sides of the equation plotted simultaneously for the specific value of v = 0.8. The two intersections mean two equilibrium points. However, only one of them is stable.

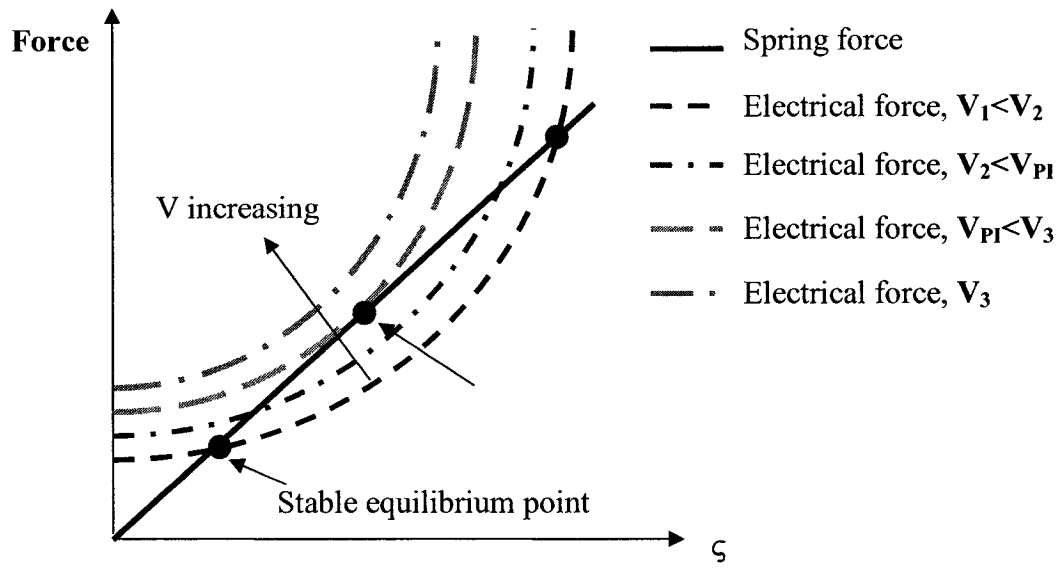

Figure 2.18. Normalized displacement analysis of voltage-controlled electrostatic actuator.

As the voltage increases, the electrical force curves move upward, and the equilibrium points move toward each other. When voltage arrives at pull-in voltage, the equilibrium points merge exactly. This point is call pull-in point. For all $v>1$, i.e $V>V_{PI}$, the curves never intersect, thus there is no stable equilibrium.

Fig. 2.19 displays the curve of the normalized equilibrium gap (g/g_0) as a function of normalized voltage. One can notice that the stable displacement occurs when normalized gaps are greater than 2/3, the unstable state collapse to zero gap once the pull-in voltage is reached.

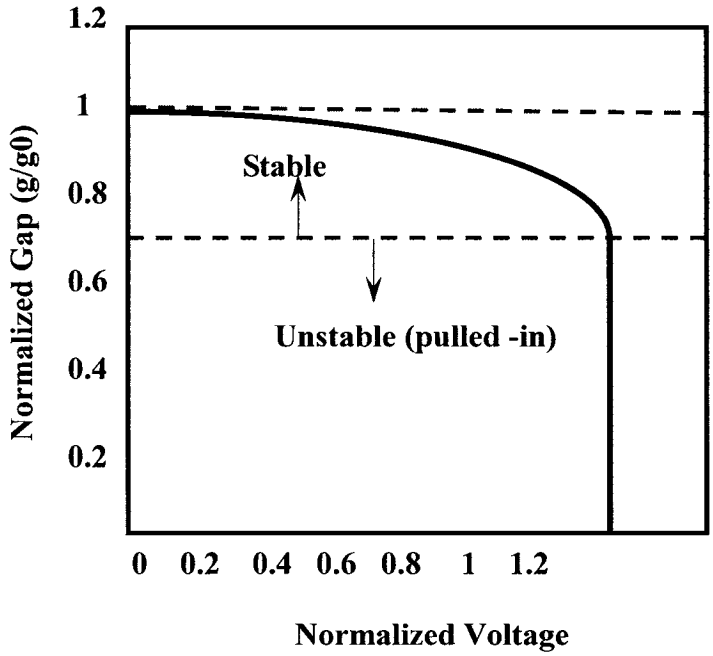

Figure 2.19. Curve of normalized equilibrium gap (g/g_0) as a function of normalized voltage.

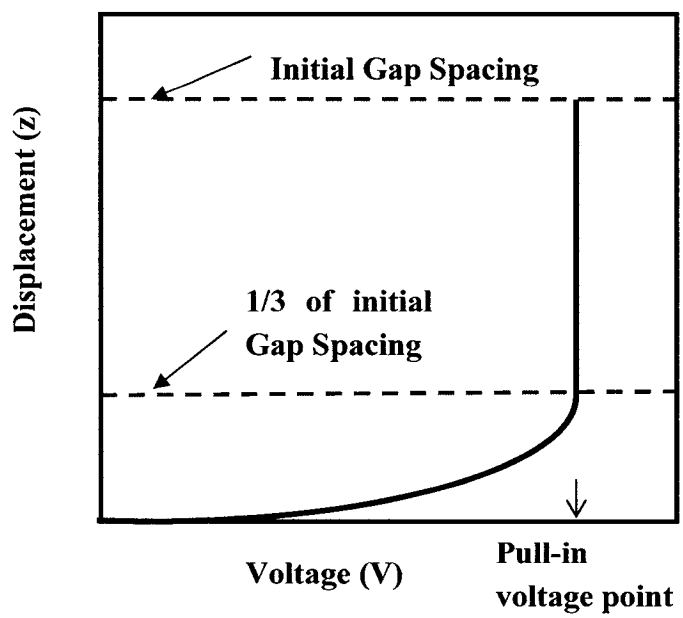

Figure 2.20. Relationships between applied voltage and the displacement of the movable plate.

Fig. 2.20 illustrates the change trend of the actual displacement of the movable plate as the function of the applied voltage. When applied voltage is less than pull-in voltage, the displacement is slowly and stably increased. Once the voltage reaches pull-in voltage, while the displacement is just 1/3 of the initial gap spacing, the displacement instantaneously jumps to the initial gap spacing. In the process of displacement events of the electrostatic actuators, actually there exists a bi-stability process as shown in Fig. 2.21.

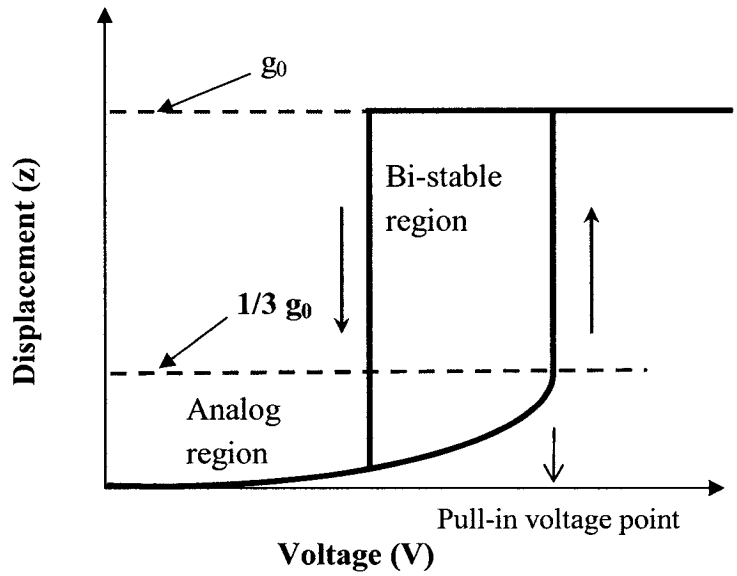

Figure 2.21. Bi-stability phenomenon existed in actual electrostatic actuator displacement.

In order to determine the pull-in voltage, we apply stability analysis which involve perturbing the position slightly and evaluate if the net force tends to return to the equilibrium position.

The net force can be expressed as

$$F_{net} = \frac{-\varepsilon A V^2}{2g^2} + k(g_0 - g) \tag{2.25}$$

At an equilibrium point, F_{net} is zero. However, an equilibrium point is unstable if in the presence of small perturbation, the net force does not tend to return it back to equilibrium position. With a small perturbation of the gap is $g + \Delta g$, the variation of F_{net} can be solved and written as

$$\Delta F_{net} = \left.\frac{\partial F_{net}}{\partial g}\right|_V \partial g \tag{2.26}$$

By evaluating it using Equation (2.25), we obtain

$$\Delta F_{net} = \left(\frac{\varepsilon A V^2}{g^3} - k\right)\partial g \tag{2.27}$$

For stable equilibrium point, the variation of the net force should be of opposite sign with the perturbation, so

$$\frac{\delta F_{net}}{\partial g} < 0 \Rightarrow \left(\frac{\varepsilon A V^2}{g^3} - k\right) < 0 \tag{2.28}$$

or

$$k > \frac{\varepsilon A V^2}{g^3} \tag{2.29}$$

At pull-in, the following requirements have to be satisfied:

$$F_{net} = 0, k = \frac{\varepsilon A V_{PI}^2}{g_{PI}^3} \tag{2.30}$$

where V_{PI} is pull-in voltage, g_{PI} is the gap spacing at pull-in voltage point.

The pull-in occurs at

$$g_{PI} = \frac{2}{3} g_0 \tag{2.31}$$

At this value of gap, the equilibrium voltage is actually

$$V_{PI} = \sqrt{\frac{8kg_0^3}{27\varepsilon A}} \tag{2.32}$$

2.3.2 FEM Simulation of The Micro Plate

This section employs coupled-field electrostatic-structural FEM analysis to simulate the surface profile and the displacement of the micro plate.

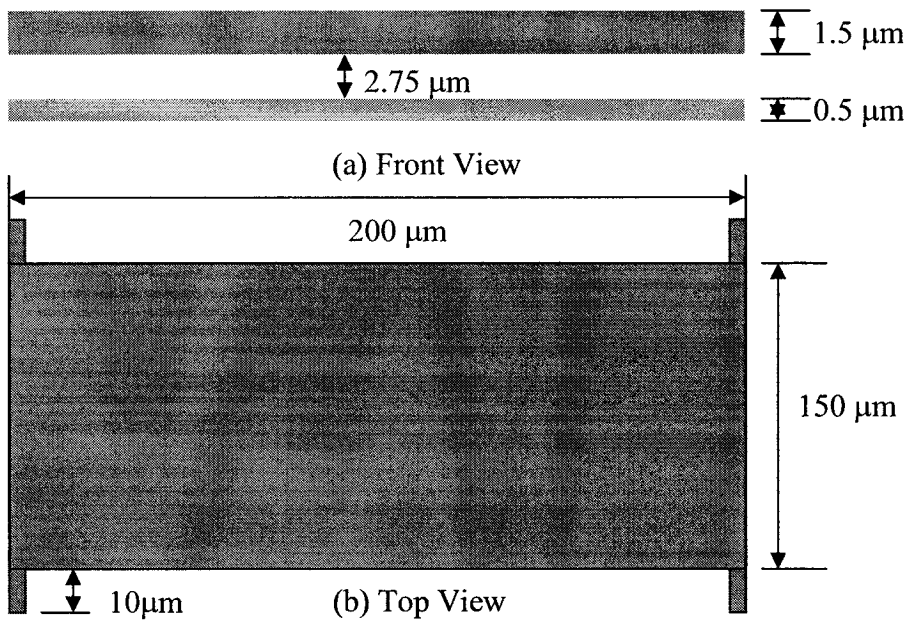

Figure 2.22. Schematic of the modeled micro plate with four springs, (a) Front view, (b) Top view.

Firstly we use the geometry shown in Fig. 2.22 for the coupled-field FEM analysis. In Fig. 2.22 we use four simpler springs to suspend the micro plate. Fig. 2.23 displays the contour plot of the displacement of the micro plate when applying 40 *V*. We can see when applied voltage, the micro plate doesn't deflect linearly. Its displacement profile appears

to be like regular annual ring. The maximum vertical displacement of the micro plate is 0.5375 μm, and appears in the center of the plate.

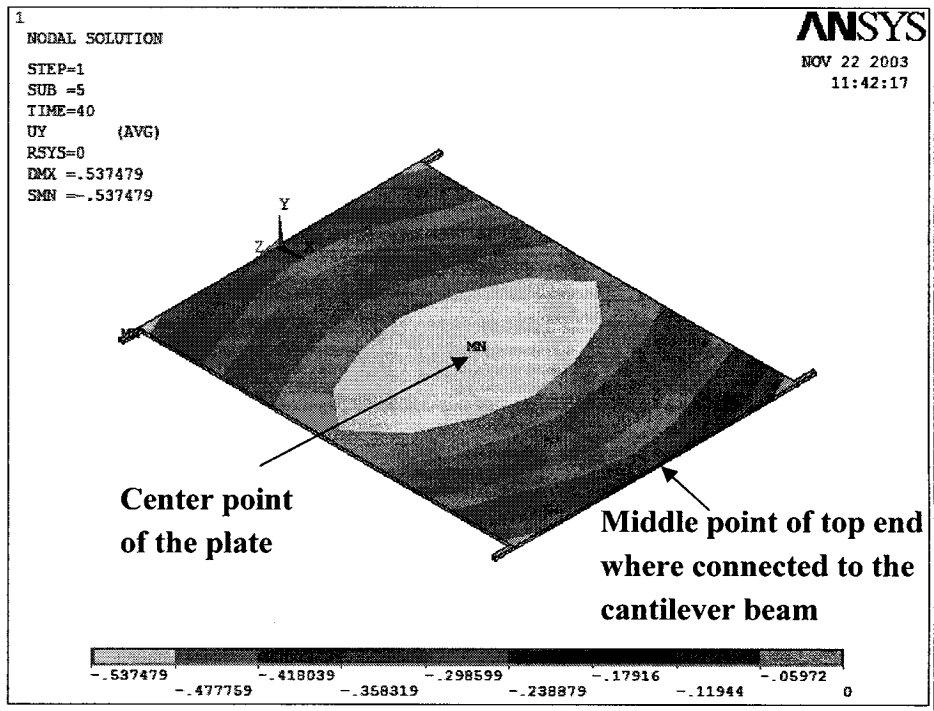

Figure 2.23. Contour plot of the displacement of the micro plate (200μm x150μm) done by FEM analysis.

Fig. 2.24 shows the vertical displacements at the center point and at the middle point of top end when applied voltage. It illustrates that at the same applied voltage, the displacement of the middle point of top end is much less than that of center point. For an instance, at 32 *V* applied voltage, the center point has around 0.275 μm displacement, whereas the middle point of top end only has around 0.012 μm displacement.

(a)

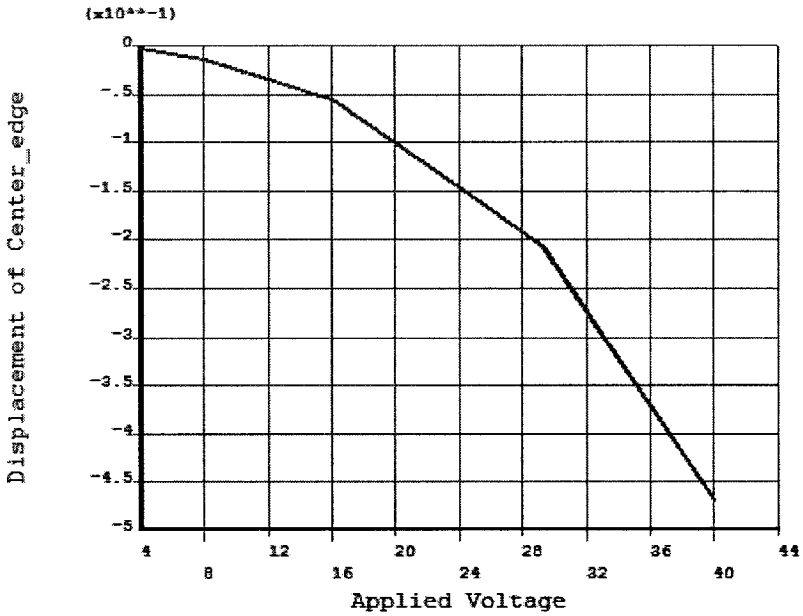

(b)

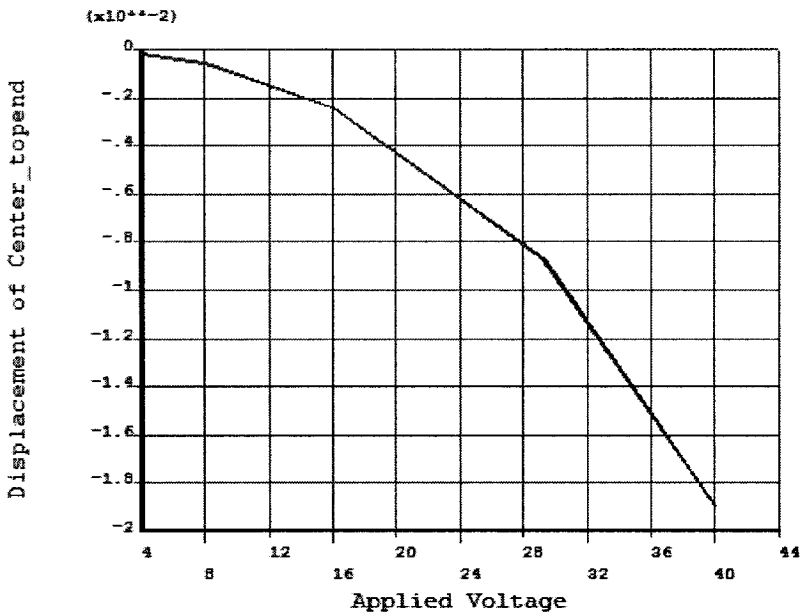

Figure 2.24. Plot of the relationship between the vertical displacement of the micro plate and the applied voltage (200μm x 150μm) done by FEM analysis, (a) at center point, (b) at middle point of top end.

Then we changed the geometries of the micro plate to 150 μm long x 200 μm wide and performed the same FEM analysis. Fig. 2.25 displays the contour plot of the

displacement of the micro plate when applied the same 40 *V*. The maximum vertical displacement of the micro plate is 0.5934 μm, a little bit larger than that of the micro plate with 200 μm long x 150 μm wide, and also appears in the center of the plate. In addition, we can notice that the maximum area has reached the top end of the plate. This result illustrates that the micro plate like this shape can easily and effectively transfer the initial actuation to the other microstructures like cantilever beams.

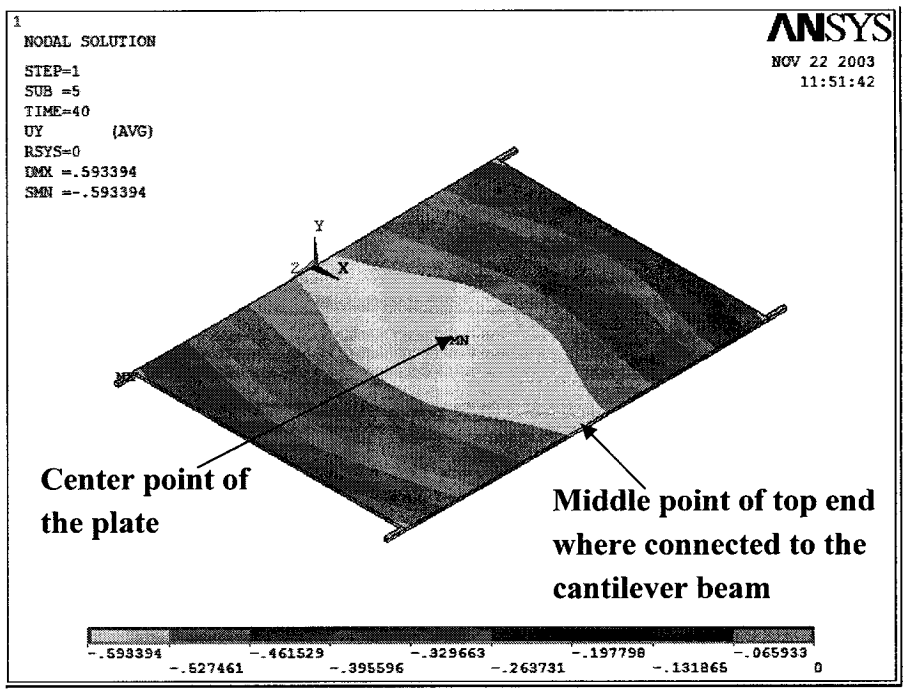

Figure 2.25. Contour plot of the displacement of the micro plate (150μm x 200μm) done by FEM analysis.

Finally, the FEM analysis of the micro plate with 200 μm long x 200 μm wide was performed and the result was shown in Fig. 2.26. The applied voltage is 35 *V*. Its surface profile appears to be like the regular annual ring. The maximum vertical displacement of

the micro plate is 0.6743 μm, appearing almost in the center area of the micro plate.

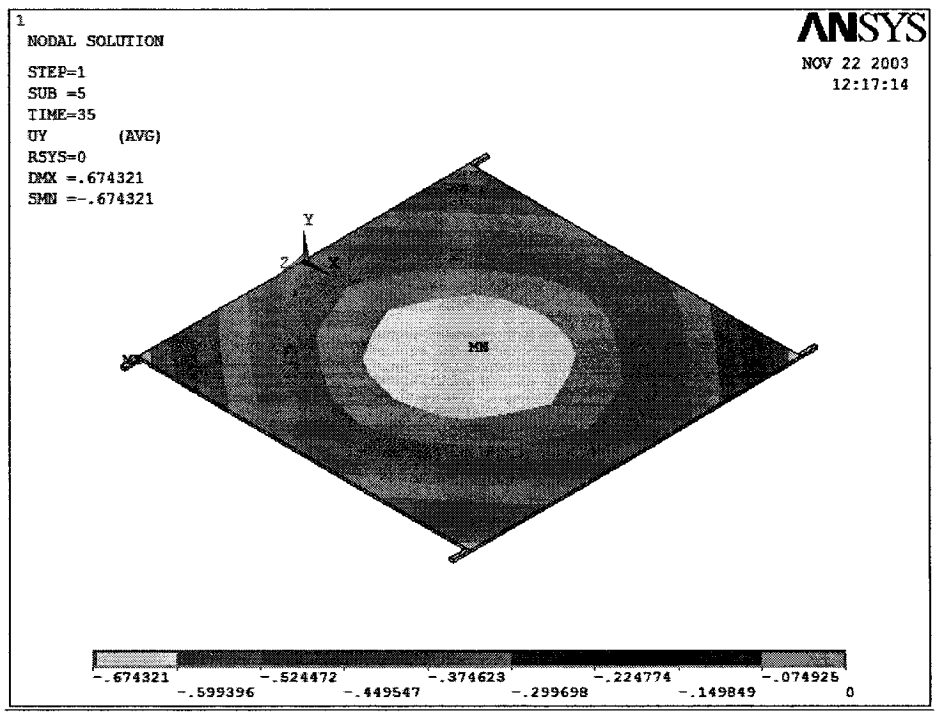

Figure 2.26. Contour plot of the displacement of the micro plate (200μm x 200μm) done by FEM analysis.

From the different modeling results of the different geometries of the micro plate, we can realize that the displacement properties of the suspended micro plate are dependent on its shape. From the displacement profiles of the suspended micro plate, we can obtain that the micro plate with the geometries of 150 μm long x 200 μm wide is appropriate to be the initial actuation for the other microstructures like cantilever beams, whereas the other two shapes of the micro plate are a little difficult to transfer the initial actuation to the microstructure connected to them. The programs of modeling in this section are developed and listed in Appendix B-4.

2.4 Modeling and Simulation of The Cantilever Beam under Electrostatic Force

This section analyzes and investigates the electrostatic properties of the cantilever beam. All the analyses are based on the designed cantilever beam presented on Section 2.1.4.

Coupled-field FEM analysis was employed to simulate the displacement of the cantilever beam. The geometry used is shown in Fig. 2.27.

Fig. 2.28 displays the simulation result when applying 5 *V*. The vertical displacement of the right end of a 400 μm long, 30 μm wide cantilever beam is 0.933μm. The programs of modeling are developed and list in Appendix B-5.

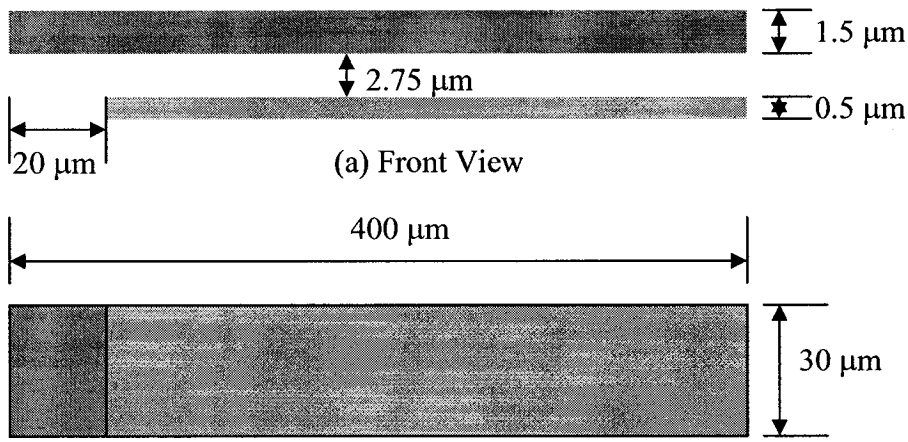

Figure 2.27. Coupled-field analysis of cantilever beam, (a) Front view, (b) Top view.

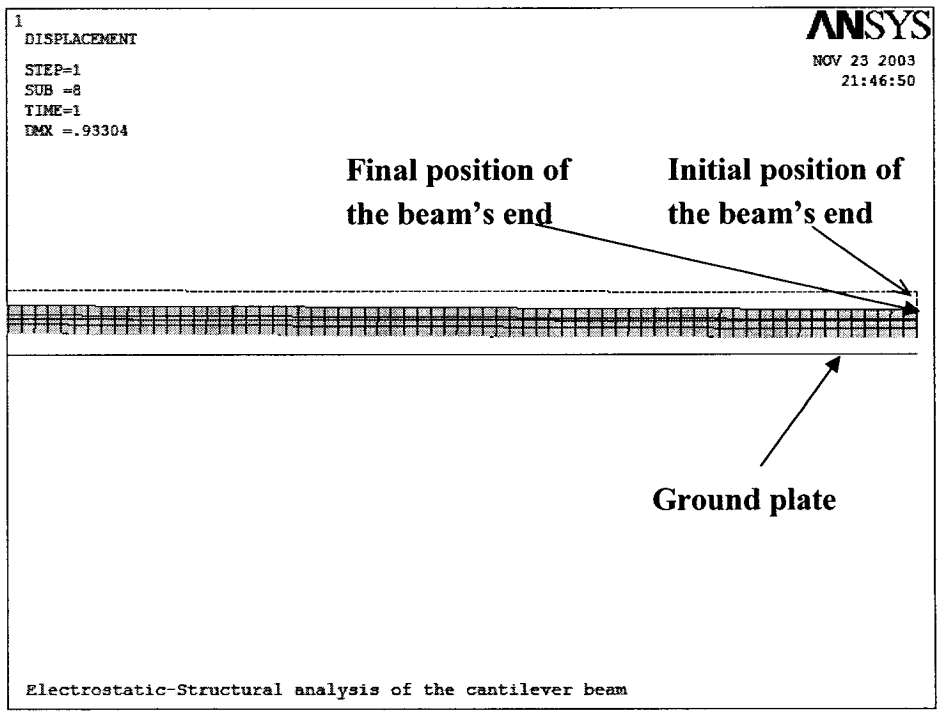

Figure 2.28. Simulation results of the displacement of cantilever beam by electrostatic-structural coupling analysis.

In this chapter, we presented the design schemes of the electrostatically driven micro actuator, and its main functional parts. Then the cantilever beam associated with thin film stresses was modeled and simulated. The simulation results match analytical solutions very well. Furthermore we presented the coupled-field electrostatic-structural FEM analysis of the micro plate and the cantilever beam. In order to verify the simulation results with practical devices, we will fabricate the proposed devices by a standard surface micromachining process - MUMPs process technology. Next chapter will discuss the details about the fabrication.

Chapter 3 Fabrication of The Micro Actuator

In this chapter, we focus on the fabrication and post-processing of the proposed devices. We use the MUMPs process technology to fabricate the proposed devices. Some issues about fabrication are described. Furthermore, some experimental discussions are presented.

3.1 Main MUMPs Processes

MUMPS is a three-layer polysilicon surface micromachining process. The process consists of 7 physical levels and 8 lithography levels. The physical levels are composed of a non-patternable nitride isolation layer, a ploysilicon ground (plane) layer (Poly 0), two structural ploysilicon layers (Poly 1 and Poly 2), two oxide release layers (PSG) and one metal layer for electrical connection and reflectivity enhancement.

Generally the MUMPs process starts from 100 mm thick n-type silicon wafers of 1-2 Ω-cm resistivity. In order to prevent or reduce charge feedthrough to the substrate from electrostatic devices on the surface, these wafers are heavily doped with phosphorus. Next, a 600 nm silicon nitride layer is deposited on the wafers as an electrical isolation layer. This is followed by the deposition of a 500 nm polysilicon film-Poly 0. The Poly 0 is the layer not released in the MUMPs process, so it is typically used as a ground plane or for routing purposes. Poly 0 is then patterned by photolithography, a process that includes the coating of the wafers with photoresist, exposure of the photoresist with the

appropriate mask and developing the exposed photoresist to create the desired etch mask for subsequent pattern transfer into the underlying layer. After the photolithography process, the poly 0 layer is etched in a RIE system. A 2.0 μm phosphosilicate glass (PSG) sacrificial layer is then deposited and annealed. The layer of PSG, known as First Oxide, will be removed at the end of the whole MUMPs process to free the first mechanical layer of polysilicon. This sacrificial layer can be patterned by photolithography with masks such as Dimple and Anchor 1.

After patterning the first oxide, the first structural layer of polysilicon (Poly 1) is deposited at a thickness of 2.0 μm. The polysilicon is lithographically patterned using a mask designed to form the first structural layer Poly 1.

After Poly 1 is etched, a second PSG layer (Second Oxide) is deposited and annealed. The second oxide can be patterned by two different etch masks: Poly 1_Poly 2_VIA and Anchor 2, with different objectives. The Poly 1_Poly 2_VIA level provides the etch holes in the second oxide down to the Poly 1 layer in order to make mechanical and electrical connections between Poly 1 and Poly 2 layers. The second structural layer, Poly 2, is then deposited with 1.5 μm thickness. As Poly 1 patterned, Poly 2 structural layer is patterned by the second designed mask Poly 2. Finally a 0.5 μm metal layer is deposited for use of probing, bonding, electrical routing and highly reflective mirror surfaces. The wafer is lithographically patterned by Metal mask and the metal layer is deposited and patterned using lift-off. Finally the chips will be performed HF release to

release the structural layers.

3.2 Fabrication of The Micro Actuator

3.2.1 Some Fabrication Issues

Most of the structural layers of the micro actuator are made from the Poly 2 layer, which is 1.5 μm thick. The cantilever beams with two thin films are made from the Poly 2 layer and a thin metal film deposited atop the Poly 2 layer. Since the fabricated devices are electrostatically driven micro actuator, both the electronic isolation and the mechanical support have to be considered. In order to electronically and mechanically isolate the main structural layer (Poly 2) from the ground layer (Poly 0), dimple type of structure has been considered. Figure 3.1 shows how the dimples make electronically and mechanically isolation. When the structural layer of the cantilever beam moves down to ground layer, the dimples underneath the structural layer contact the isolation layer before the structural layer contacts the ground layer. Thus it electronically and mechanically protects the structural layer from the ground layer. According to the MUMPs design rules, dimple structures are designed to create dimples and bushings for Poly 1 layer. Whether or not dimples can be designed underneath Poly 2 layer brought out a challenge for the MUMPs fabrication. After elaborate research and discussion of MUMPs fabrication process with technical staff at CMC (Canadian Microelectronics Corporation) and Cronos Integrated Inc. (original MUMPs foundry service provider), some solutions of this issue

were obtained as presented in Table 3.1.

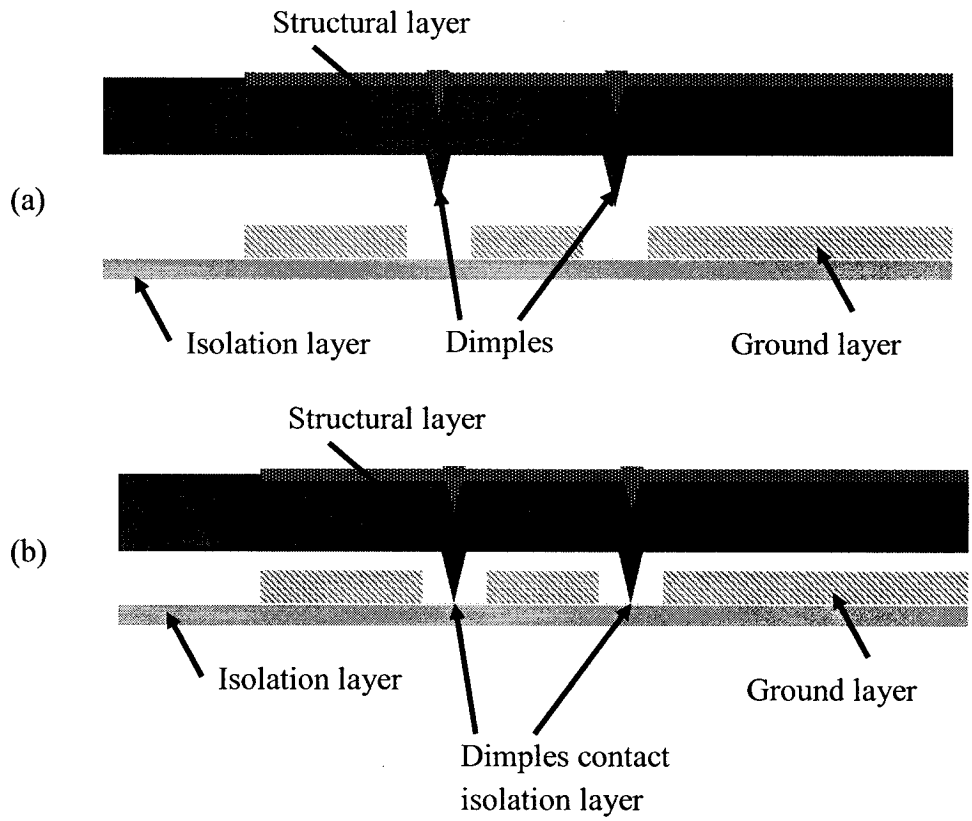

Figure 3.1. Schematic of isolation functions of dimples, (a) before applied electrostatic force, (b) after applied electrostatic force.

Table 3.1. Solutions of dimples underneath Poly 2 layer

Solutions	Dimple Depth (μm)	Comments
Dimple etch and Poly 2	Approximate ~0.6	Dimple depth very dependent on its size
Anchor1 etch and Poly 2	Approximate ~1.9	Dimple depth dependent on its size
P1P2_VIA etch and Poly 2	Approximate ~1.125	
Dimple etch and P1P2_VIA etch and Poly 2	Approximate ~1.7	Dimple depth very dependent on its size
Anchor1 etch and P1P2_VIA etch and Poly 2	Approximate ~2.75	Will anchor Ploy 2 layer

As one can see from the above table, the different solutions lead to different depth

of the dimples. One reason is that Dimple, Anchor1 and P1P2_VIA three layers have different thickness, further the situations which oxide2 sacrificial layers fill up the dimple area after etching in different solutions are quite unpredictable and much dependent on the feature size of the designed dimple. In addition, if P1P2_VIA mask is used, there will be some overetch (about 50%) during the P1P2Via etch.

The depth of the dimples can extremely affect the performance and function of fabricated devices. While the dimples are considered to electronically and mechanically isolate the structural layer from the ground layer, they are also considered to be the support point of lever amplification mechanism. In order to make downward movement of the structural layer (Poly 2) to the ground layer (Poly 0) as much as possible, the depth of the dimples should be as little as possible, therefore we chose the first solution which has the least deep dimple to fabricate the dimples underneath Poly 2 layer.

3.2.2 Fabrication Results

The proposed devices have been fabricated by Cronos Integrated Inc. MUMPs foundry service via CMC's BEAM program. Normally each run (fabrication cycle) takes about 3-4 months. In total we participated two MUMPs runs from September 2002 to July 2003 to fabricate our devices by CMC. Fig 3.2 shows parts of our devices fabricated by CMC.

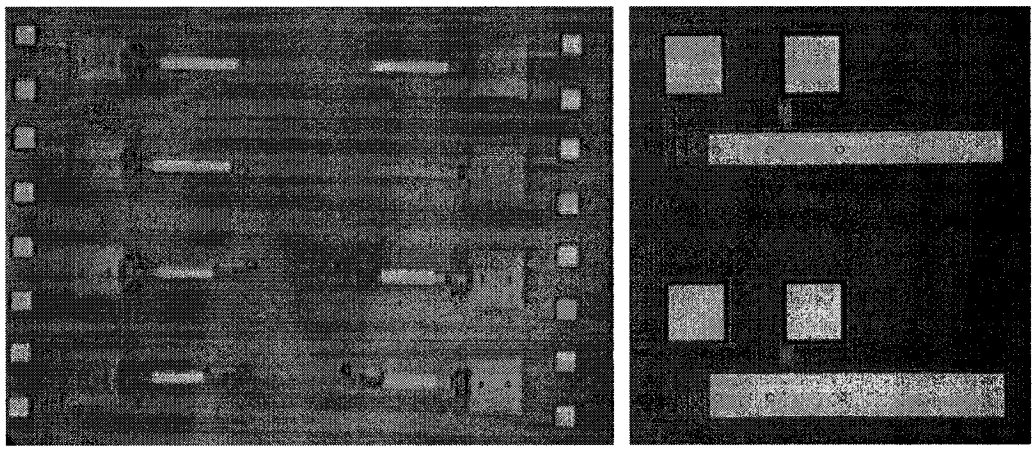

(a) (b)

Figure 3.2. Digital picture of the devices fabricated by CMC, (a) the electrostatically driven micro actuators, (b) the cantilever beams with thin film stress.

3.3 Post-processing

After the device fabrications were completed, the chips were shipped back to Concordia University for post-processing. The main post-processing is to perform HF release. HF release is the process which uses concentrated (49% resolution) HF etchant to etch away the PSG sacrificial layer between polysilicon structural layers and thus free the mechanical structures. The release procedures can be performed as recommended in MUMPs Handbook [2]: firstly chips are immersed in acetone for 3 minutes, and then in De-ionized (DI) water for 30 seconds. These two steps strip photoresist off. After that, chips are put in the 49% HF (room temperature) for 1.5-2 minutes to etch oxide off. This is followed by several minutes in DI water and then alcohol for 5 minutes to reduce stiction followed by at least 10 minutes in an oven at 110° C. However, when we

performed HF release in the microelectronic lab of Concordia University, based on the procedures recommended by MUMPs handbook, we adjusted some items and got some extension about HF release time according to the different conditions.

3.4 Experimental Discussions

In the course of HF release, some related phenomena have been observed.

Firstly after performed one etching cycle, the structural layers were not released as expected due to the incomplete removal of the oxide between the ploysilicon layers. Then the chips were re-etched about 5 minutes. However it did not make much difference. After the total etching time was increased to 15-20 minutes, the devices can be observed to have larger flexure at the end of the cantilever beam. Since the cantilever beams are composed of two thin films which will produce large flexure after complete release, it proves that the devices have been completely released. Fig. 3.3 (a) and (b) show the fabricated cantilever beams before and after release, respectively. It clearly shows that after complete release the micro cantilever beams are curved up on the free end by thin film residual stress. Fig. 3.4 is another digital photograph showing that part of the structural layers of the micro actuator has been released.

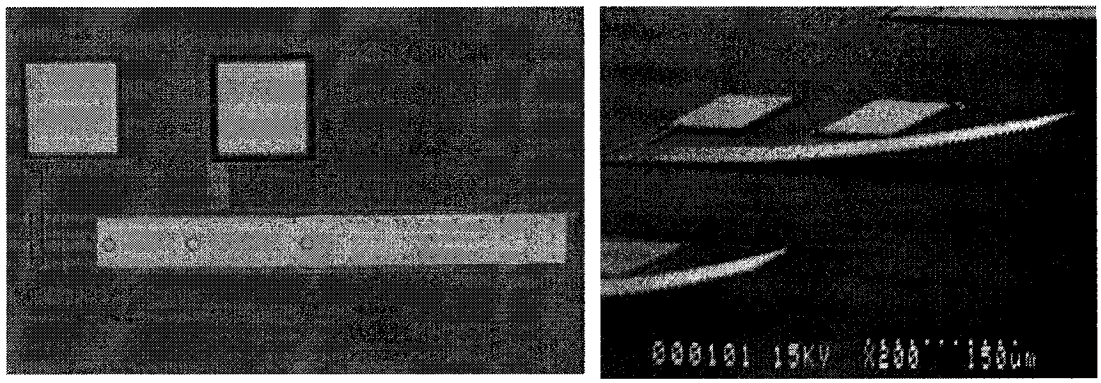

(a) (b)

Figure 3.3. Fabricated cantilever beams. (a) Before release (digital photograph), (b) after release (SEM).

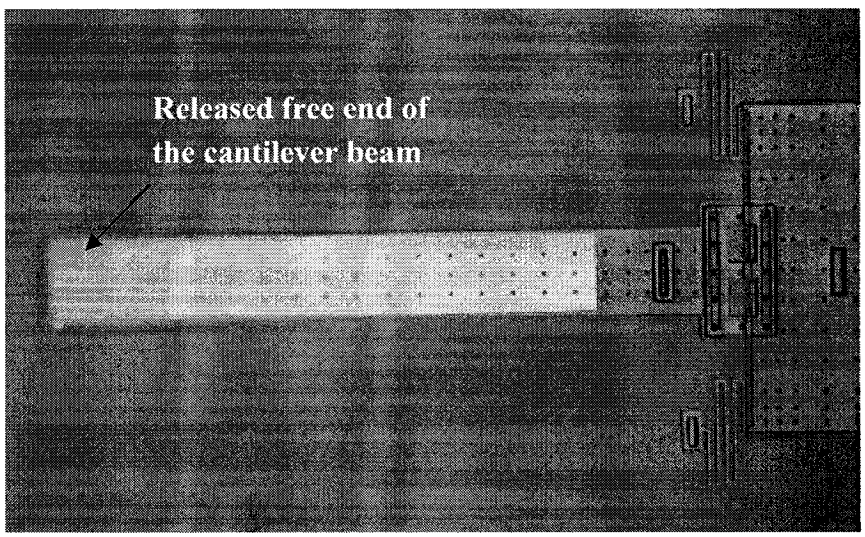

Figure 3.4. Part of the fabricated micro actuator after release (digital photograph).

The reasons of using longer etching time are various. Since there was no HOLEMs (the release hole for the Metal layer) designed on the metal layer atop the polysilicon layer in our first design, HF etchants cannot effectively penetrate through the structural layer into sacrificial oxide layer via metal layer, thus it takes longer time to get the

sacrificial oxide released. In addition, the lab equipment and experiment environment constraint (such as temperature control, time control) also led to the longer etching time.

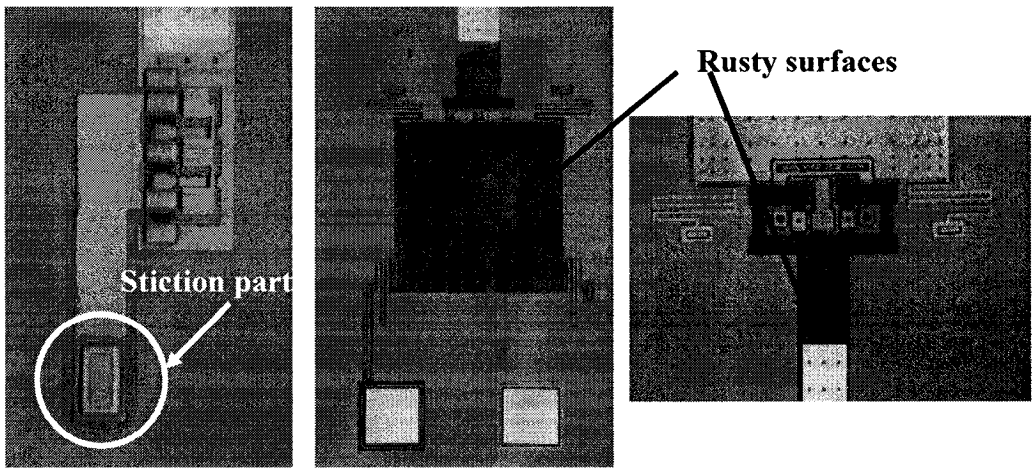

(a) (b) (c)

Figure 3.5. Some typically observational phenomena after post-processing performed in our lab, (a) stiction of micro shutter, (b) rusty surface of micro plate fabricated by Poly 2 layer, (c) rusty surface of cantilever beam fabricated by Poly 2 layer.

Furthermore, by visual inspection we noticed that during the release processing of the devices, the surface color and profile of the chip were changed and much dependent on the release time. The substrate after less than 5 minutes release appeared maroon-colored. It altered to be jade-green after 15 minutes release. After 20 minutes release, the substrate color dramatically changed to be deeply green. Accompanying with these phenomena, some part structures were stictioned (as shown in Fig. 3.5 (a)), the surface color of some parts of the polysilicon layers changed from grey to rusty (as shown in Fig. 3.5 (b) & (c)). In addition, we also observed that some chips performed HF release by CMC have the different color from that of the chips released in our lab. Fig. 3.6 shows

parts of the chips released by our lab and CMC. The surface color of the substrate on the chips released by our lab is brown, and the surface of poly structural layer appears to be rusty. Whereas the surface color of the substrate on the chips released by CMC is slight green, and there are no rusty mess on the surface of poly structural layer.

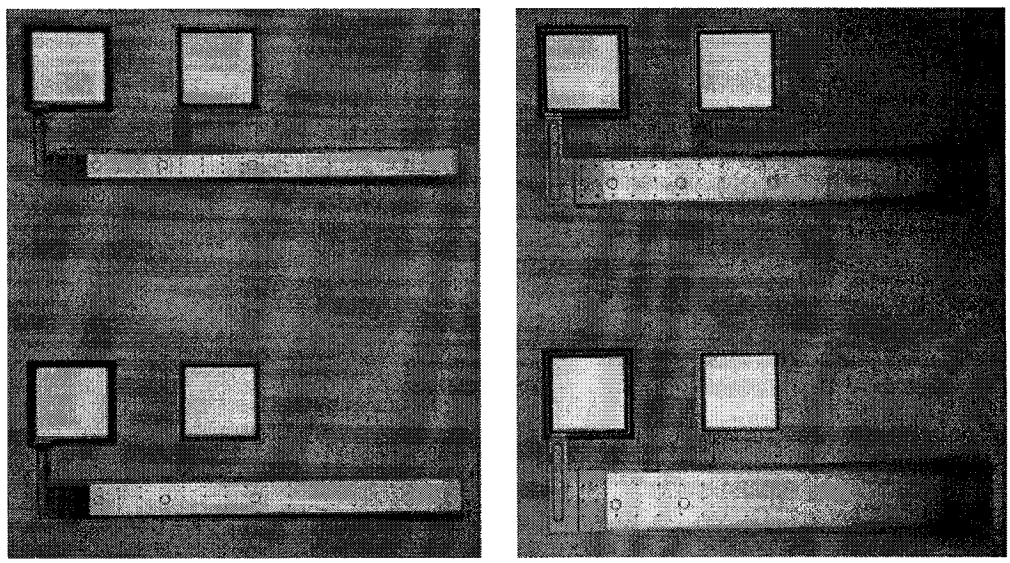

(a) (b)

Figure 3.6. Comparison of surface profile and color of parts of chips. (a) released by our lab, (b) released by CMC.

The reasons of surface color change and different surface profiles are various. The key reason is focused on the different HF release condition. On one hand, due to the extra release time leading to some overetching of polysilicon structural layer and silicon nitride layer, the physical properties of the material are changed, such as the surface profiles, the thickness of the layer, the refraction index or reflecting index. Therefore the material's surfaces appear different color. On the other hand, HF releases were implemented on different facilities and cleaning room condition, performed by different time and different

people. As a result, it led to the different results.

This chapter described the fabrication and post-processing of the proposed devices. Some post-processing issues and experimental phenomena are analyzed and discussed. After post-processing, the structural layers of the fabricated devices have been released. In next chapter, we will test and observe our devices in our microelectronic lab, functional experimental results will be presented and some key issues will be analyzed.

Chapter 4 Experimental Results and Discussions

In this chapter, functional experimental results and experimental observations are described, and based on these results and observations, some discussions and analyses are presented.

4.1 Experimental Results and Discussions of the Cantilever Beam

The released devices were tested and observed in our microelectronic lab. Since the flexure of the cantilever beams is out of plane, which is vertical, it is more difficult to measure the value of vertical flexure of the cantilever beam end than that of lateral displacement of MEMS devices like in-plane thermal actuator.

Fig. 4.1 shows the experimental setup for the measurement. Firstly we put the chips on the platform of the microscope, zoom in or zoom out to focus on the fixed end of the cantilever beam by adjusting the fine focusing knob, and read the value of the reference position of the knob, secondly we turn around the knob along the same direction gently to focus on the top free end, read the second value of the position of the knob, then we obtain the difference of the read values. For the microscope used in Concordia microelectronic lab, the focusing knob is calibrated to be 2 μm per graduation vertical displacement of the sample platform. So the actual value of flexure of the cantilever beam can be obtained.

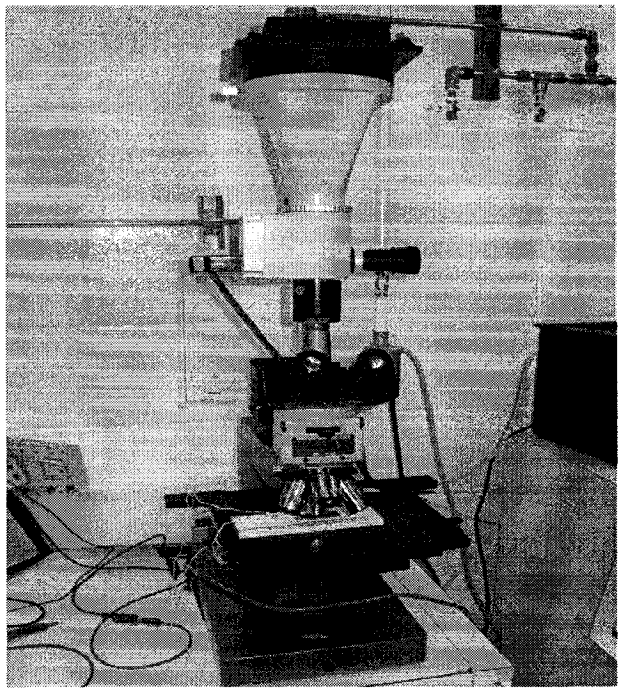

Figure 4.1. Experiment setup for the measurement.

4.1.1 End Deflections of Preload Cantilever Beam

First the preload end deflection of the cantilever beam due to thin film stresses has been measured. Table 4.1 lists the experimental results of end deflection of the preload cantilever beam released by CMC.

Figure 4.2 shows the comparison of analytical, simulation and experimental results for a 40 μm wide beam. It indicates that the simulation results are in good agreement with the analytical and experimental results, although the variation is a little larger as the cantilever beam is shorter. It has furthermore proven that the simulation modeling accurately estimated the real physical and mechanical issues. Besides that, the reasonability and correctness of selected material parameters, such as Young's Modulus,

residual stress, and Poisson's ratio, etc, has also been testified.

Table 4.1. Beam end deflections (δ) determined by experiment and by simulation

Beam (metal) Length (μm)	*Poly (metal) Width (μm)*	*δ (simulation) (μm)*	*δ (experimental) (chips released by CMC) (μm)*			*Variation (%)*
			Average	*Chip1*	*Chip2*	
555 (500)	30(22)	**33.517**	**32**	31	33	**4.5**
	40(32)	**35.417**	**39**	38	40	**10**
	50(32)	**36.489**	**43.5**	45	42	**19**
	60(52)	**37.177**	**51**	56	46	**37**
	80(72)	**37.979**	**58**	66	50	**53**
400(350)	40(32)	**16.805**	**18.5**	19	18	**10.1**
455(400)		**23.561**	**28**	28	28	**18.8**
505(450)		**28.966**	**30.5**	31	30	**5.3**
555(500)		**35.417**	**39**	38	40	**10**
655(600)		**51.451**	**53.5**	55	52	**4**
855(800)		**94.982**	**95.5**	100	91	**0.02**

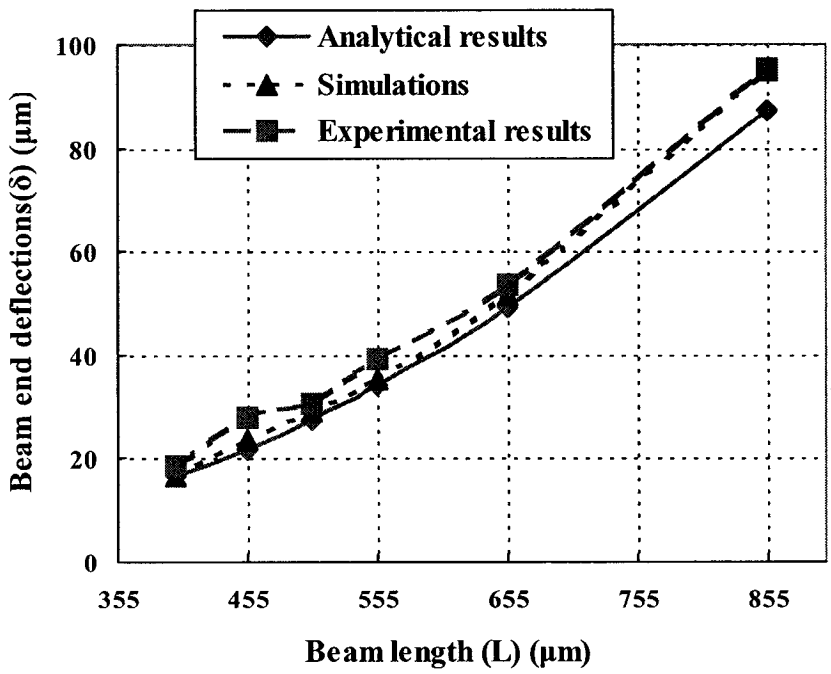

Figure 4.2. Comparison of experimental results with analytical and simulation results under 40μm wide beam.

The variation can attribute to the constraints of experiment facilities, measurement errors, and fabrication errors and uncertainties of some materials' mechanical and physical properties such as residual stress, Young's modulus, and geometric dimensions like thickness, width and length. Fortunately the improved MEMS process technologies have been performing better to achieve the feature accuracy and functional reliability and flexibility. Due to little discrepancy between the experimental results and the simulation results under the given width of the poly and metal layers, it provides a practical and flexible design solution for the preload cantilever beam. One can design certain cantilever beams which have certain preload end deflection by defining the corresponding geometries based on the simulation modeling: firstly choose reasonable poly and metal layer widths, then design specific beam length to match specific preload deflection demands.

The experimental results of the end deflection of the cantilever beams released in Concordia microelectronic lab have also been listed in Table 4.2 for comparison with those of the cantilever beam released by CMC.

Table 4.2. End deflections (δ) experiment results of cantilever beams released by CMC and Lab

Beam (metal) Length (μm)	*Poly (metal) Width (μm)*	*δ (experiment) (released by CMC) (μm)*			*δ (experiment) (released by Lab) (μm)*		
		Average	*Chip1*	*Chip2*	*Average*	*Chip3*	*Chip4*
555 (500)	30(22)	**32**	31	33	67	50	84
	40(32)	**39**	38	40	n/a	58	n/a
	50(32)	**43.5**	45	42	76.5	59	94
	60(52)	**51**	56	46	79.5	57	102
	80(72)	**58**	66	50	80	56	104
855(800)	40(32)	**95.5**	100	91	153.5	90	217
655(600)		**53.5**	55	52	119	80	158
555(500)		**39**	38	40	n/a	58	n/a
505(450)		**30.5**	31	30	n/a	n/a	n/a
455(400)		**28**	28	28	43	46	40
400(350)		**18.5**	19	18	25.5	30	21

As shown in Table 4.2, the experimental results of cantilever beams released by our microelectronic lab are much larger than those of devices released by CMC. The main reasons are attributed to the HF release processing. It is well known that etching is a quite sensitive process. The physical and mechanical functions of the etched MEMS devices will directly be affect by HF release result and quality, which furthermore are very dependent on a variety of factors, such as environment temperature, etchants use and etching time, the methods used to avoid stiction of released devices, etc. On one hand, the facilities and cleaning room condition of Concordia microelectronic lab are different from those of CMC. On the other hand, some specific post-processing procedures are also different, for instances, CMC use supercritical CO_2 drying process to avoid stiction from

the released chips, whereas we used oven in our lab to bake the chips for 10-15 minutes at around 120°C right after methanol rinse. In addition to our longer etching time and probably invalid etchants, therefore the release results are expected to be quite different. Nevertheless, The real reasons that results of us are larger than those of CMC are still uncertain. In future work, we will try to focus on this field.

4.1.2 Top End Displacements by Applied Voltage

The top end displacement of the preload cantilever beam has also been tested by applied bias voltage. The test method is the same as above described. Tested cantilever beam is 555 μm long, 80 μm wide. In initial state (before applied bias voltage) the top end of the cantilever beam is 66 μm high over the ground layer. After applied bias voltage, the top end of the cantilever beam vertically moved downward to the ground layer by the electrostatic force.

Figure 4.3 plots the relationship between the top end displacements and applied voltages. It is noticed that the top end displacement arrives to its peak value (51 μm) at 8 *V* applied voltage. When applied voltage is less than 8 *V*, the top end displacement increases as the applied voltage increases; whereas when applied voltage is more than 8 *V*, the top end displacement decreases as the applied voltage increases. However, when applied voltage increases from 9 to 12 *V*, the top end displacement stabilizes at the same value (41 μm) without any change. When applied voltage arrived to 13 *V*, the tested

cantilever beam did not present any movement. By observation it was found that parts of the tested cantilever beam were broken.

One can notice that the relationship of end displacement and applied voltage indicated in Fig. 4.3 is different from that of the theoretical relationship illustrated in Fig. 2.21. One reason is that the tested cantilever beams are bended upward by thin film stresses before applied voltage. This characteristic partly altered the premises and assumptions of the theoretical relationship. In addition, the initial thin film stresses also have distinct influence on the pull-in voltage of the tested devices [55]. Exactly how the initial thin film stresses change the theoretical pull-in voltage and how they influence the theoretical relationship of end displacement and applied voltage will be investigated in future work.

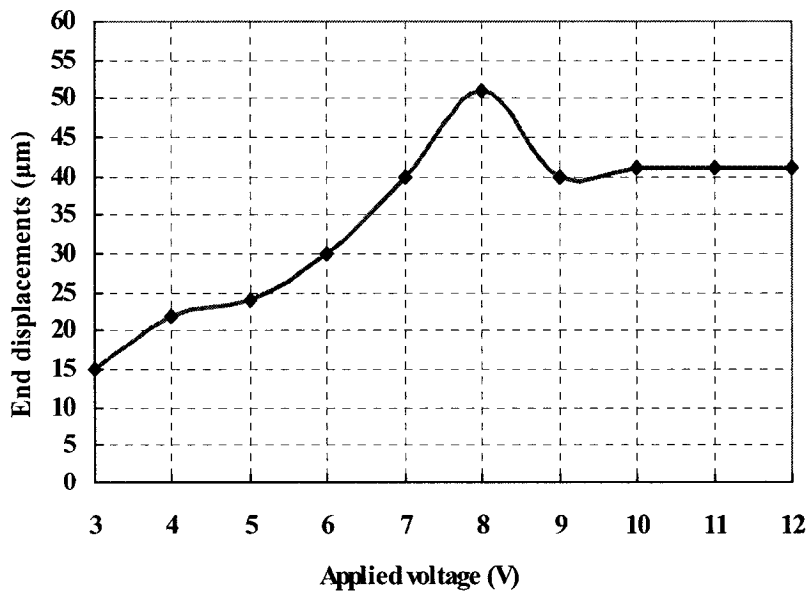

Figure 4.3. Experimental results of the top end displacement of the preload cantilever beam (555 μm long x 80 μm wide) vs. applied voltage.

4.2 Observations and Discussions of the Micro Actuator

The fabricated electrostatically driven micro actuators have been observed and analyzed in our lab. Fig. 4.4 and Fig. 4.5 respectively exhibit the main part of the device before and after release.

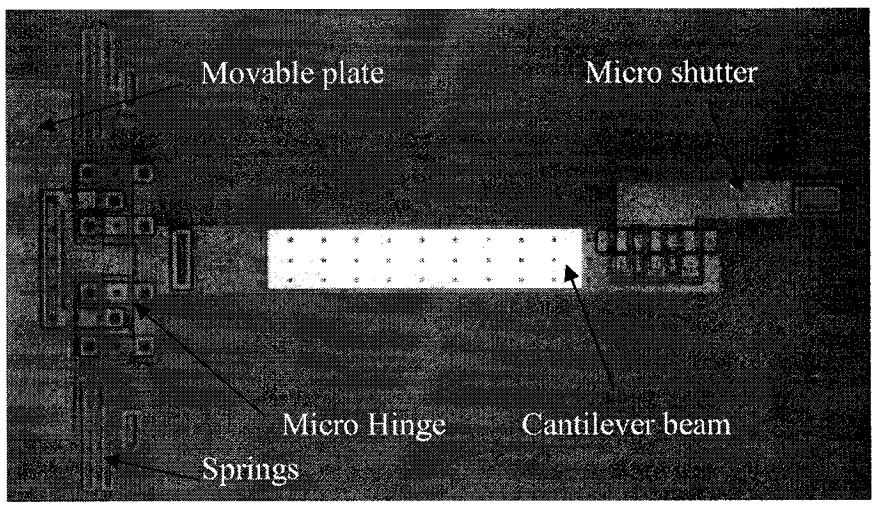

Figure 4.4. Digital photograph of electrostatically driven micro actuator (Before release).

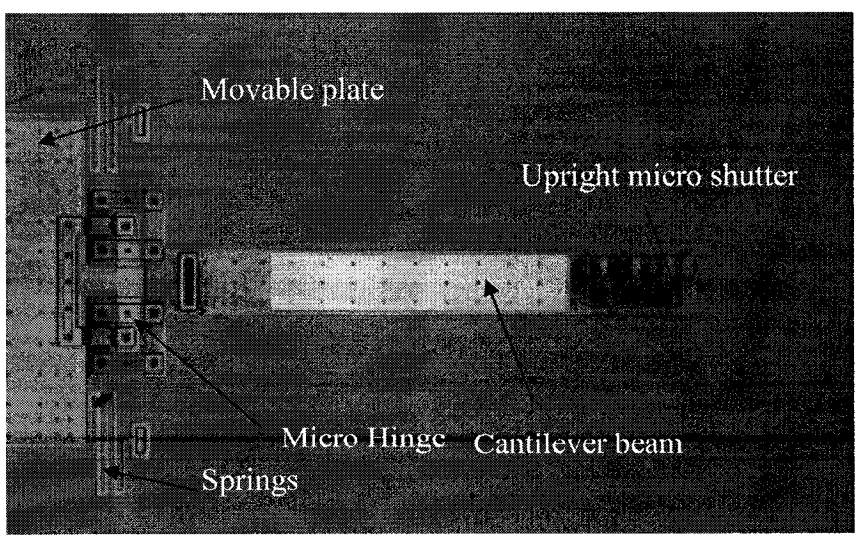

Figure 4.5. Digital photograph of electrostatically driven micro actuator (After release).

4.2.1 Observation of The Main Parts

(1) The micro shutter connecting the micro plate and the cantilever beam

Fig. 4.6 shows the pictures of micro hinge design for connection of the micro shutter and the cantilever beam, one is before release, and the other is after release. The SEM shows the micro shutter has erected up over the top of the cantilever beam. It proves that the reasonability and feasibility of our design. The upright of the micro shutter makes it possible to effectively block parts of or whole lateral optical signal in optical networking. Furthermore, if a micro mirror can be designed and fabricated on the micro shutter, it is also possible that the micro shutter could be used to reflect the optical input signal to certain output direction. However, our design still needs some modifications to make it stable and steady.

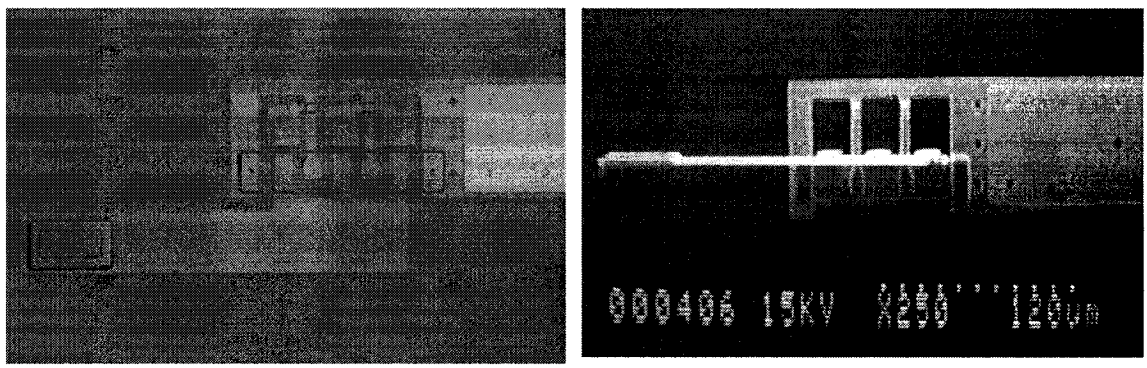

(a) (b)

Figure 4.6. Micro hinge design for the connection of the micro shutter and the cantilever beam, (a) before release (digital photograph), (b) after release (SEM).

(2) The connection mechanism between plate and cantilever beam

As we mentioned before, the joint connecting the movable plate and the cantilever beam is the key part to transfer and apply the electrostatic force to actuate the cantilever beam. Three designs were observed, and the performance of different designs was compared. Fig. 4.7 to Fig. 4.10 display the device pictures of the three different designs.

The micro concaved-up scissor hinge design is shown in Fig. 4.7. Fig. 4.8 shows a cantilever beam connected to the micro plate by the micro hinge has been turned over. It partly illustrates this design is flexible, and easy to apply the force on the end of the beam. However, the complexity of this design makes it unsteady.

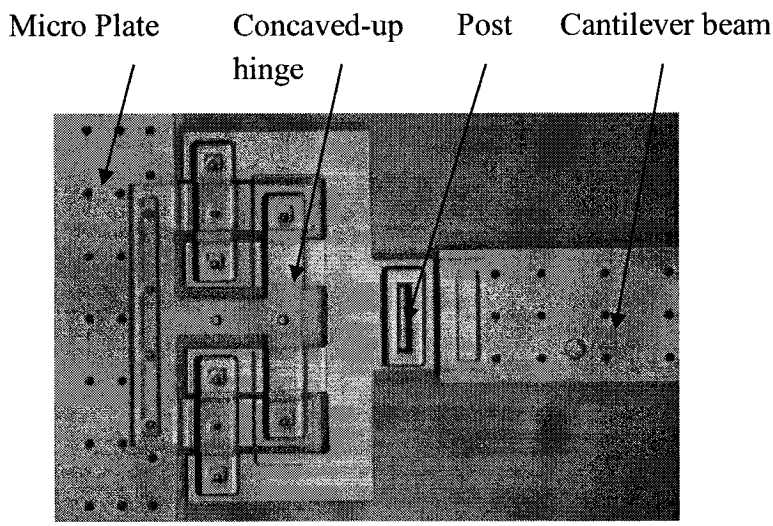

Figure 4.7. Digital photograph of the concaved-up hinge designed for connection of micro plate and cantilever beam.

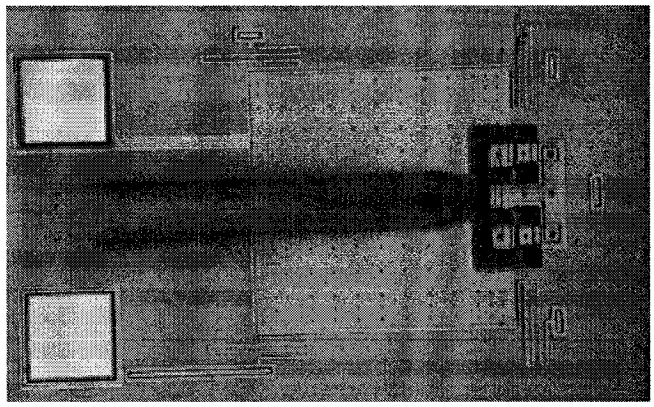

Figure 4.8. Digital photograph of a turnover cantilever beam connected to micro plate by concaved-up hinge designed.

The three micro strips connection is shown in Fig. 4.9, and the two narrow strips connection is shown in Fig. 4.10. These two designs are relatively simple, steady and feasible. But due to their more stiffness, they are less flexibility than concaved-up scissor hinge design.

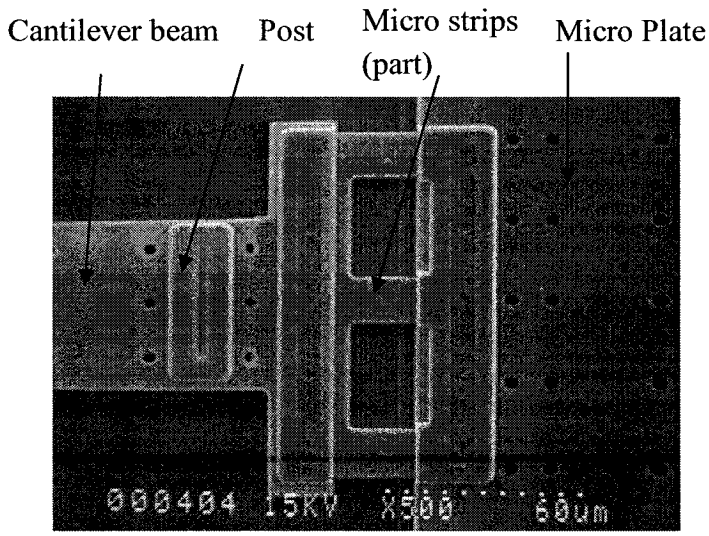

Figure 4.9. SEM of the micro strips designed for connection of micro plate and cantilever beam.

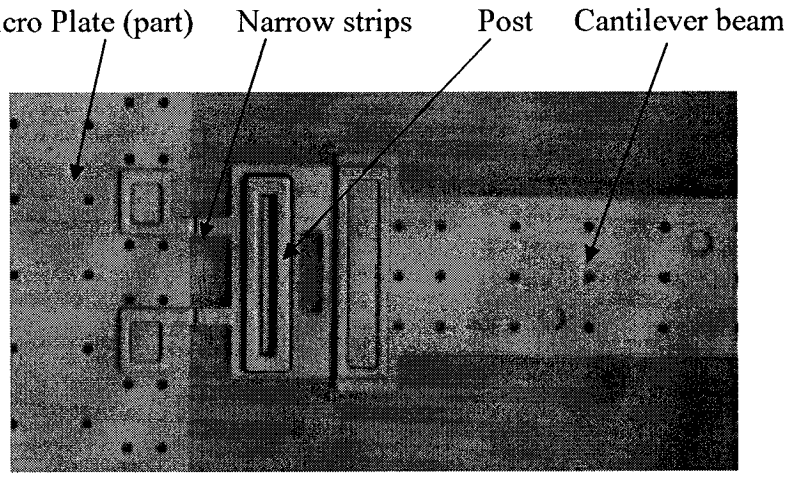

Figure 4.10. Digital photograph of two strips designed for connection of micro plate and cantilever beam.

(3) The micro springs

The SEM of the micro spring is displayed in Fig. 4.11. Next section we will discuss this design in detail.

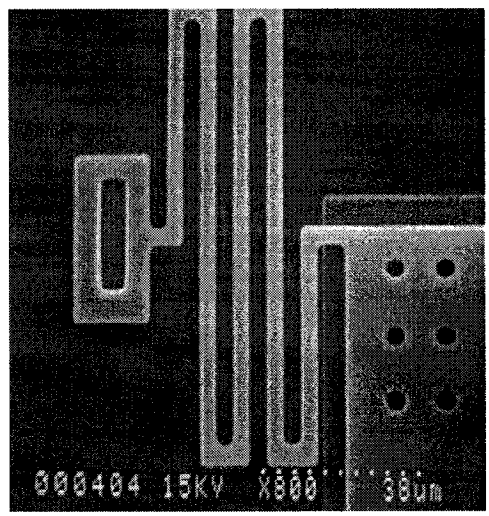

Figure 4.11. SEM of designed micro springs (fabricated in the Poly2 layer).

4.2.2 Observations and Discussions

The electrostatically driven micro actuators are observed and tested at our microelectronic lab. The equipment used to observe and measure is the probe station shown in Fig. 4.12. The applied voltages range from 0 to 20 *V*. Three chips were observed.

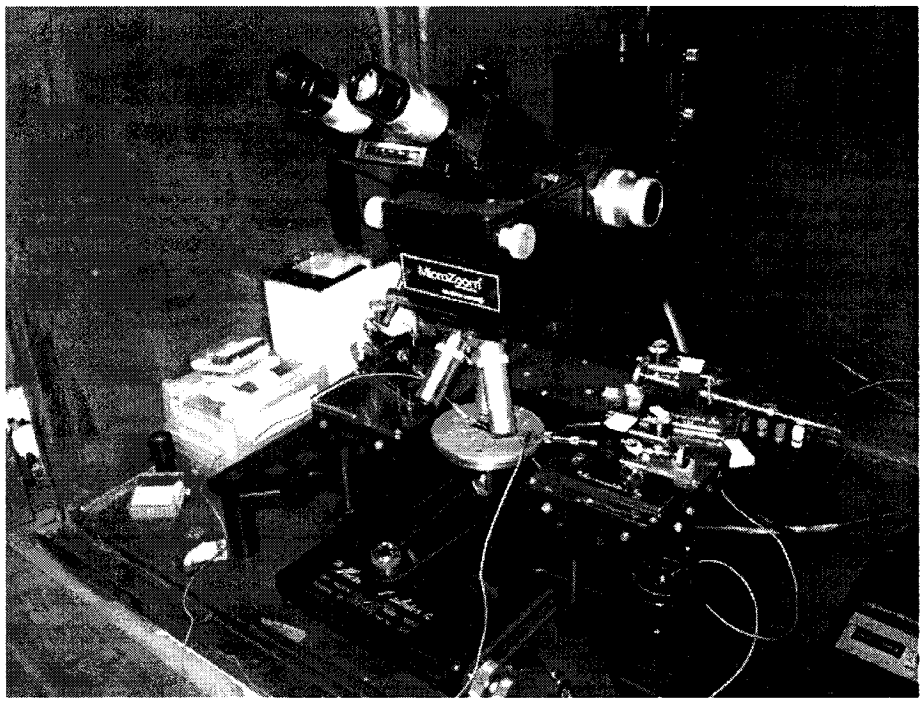

Figure 4.12. Photograph of the probe station used to observe and measure the devices.

We have to mention there exist some constraints of experiment equipment. For examples, the probe bases are magnetized on a fixed platform while sample device is actually sucked on a differently movable platform. In order to keep the contact constant and stable between probes and the pads of the sample, the relative position of the sample and the probe cannot be changed. That is to say, we can't move the sample flexibly to

observe and measure it from the microscope. In addition, due to the relatively larger size of the probe comparing with the dimension of the measured chips, the vertical space between microscope and the surface of the chips is dramatically limited. Thus the option of magnification is limited.

The distinct movement of the device has been observed from 5X zoom objective of the microscope when applied voltage on the micro actuator. Also the observed flexure of the micro springs indicated the displacement of the micro actuator. However, due to the smaller displacement of the micro actuator, it is difficult to obtain the experimental results by our current test equipment. One of the reasons that cause smaller displacement of the micro actuator is the connection mechanism connecting micro plate and cantilever beam cannot effectively transfer initial actuation of the micro plate. In addition, the displacement of micro plate was not so much to effectively actuate the connected cantilever beam. More focus on the design of the micro plate and the connection mechanism need to be done in the future work.

As the applied voltage increased, the displacement of the micro actuator was more distinct. When applied voltage arrived to around 20 volts, the micro spring nearest to the pad appeared bright glowing and kept glowing for several seconds when we continued applying the voltage. Then no displacement happened even if gradually applied voltage. Observational result showed the spring was partly broken by short circuit (as shown in Fig. 4.13).

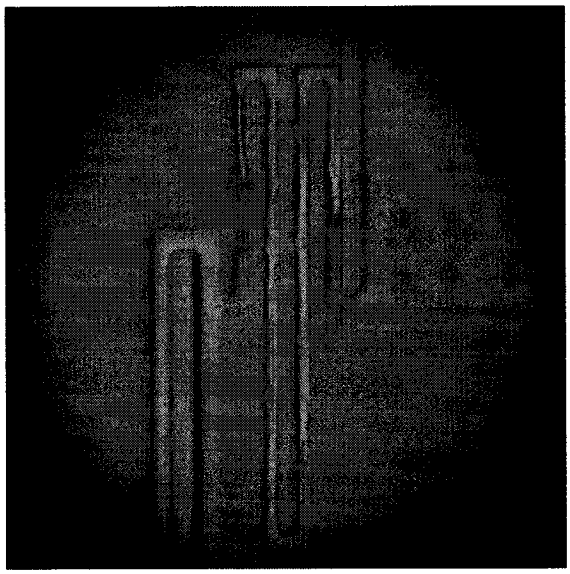

Figure 4.13. The photograph of the broken micro spring caused by short circuit after applied voltage 20 *V*.

In order to explore the probable reasons of short circuit, some calculations have to be done firstly.

The spring constant can be determined by using the following formula:

$$K = C^{-1} \tag{4.1}$$

where

$$C = \frac{L^3}{E \cdot I}\left(\frac{N}{12} + \frac{1}{48}\right) \tag{4.2}$$

where C is the compliance of the spring, L is the length of the spring bars, E is Young's Modulus for the spring material, and I is the 2nd moment of the spring bars determined by Equation (2.15), and N is the number of the spring bars, excluding the two half-bars at the top and bottom of the spring [45].

The Equation (4.1) and (4.2) make several approximations, such that neglecting the

flexing in the sections connecting the bars. For the spring bar dimension like 2 μm bar width, 2 μm gap spacing, and 100 μm long springs, the error rate of the solution of the equation is merely less than 2.6% comparing to the solution modeled in ANSYS [45].

The totally spring constant of the micro electrostatic actuator is approximately the sum of each individual spring constant, $k = k_1 + k_2 + \mathrm{K} + k_n$.

For our 120 μm long spring, we can obtain $k_1 = 0.587N/m$, for 100 μm long spring, we can obtain $k_2 = 1.014N/m$, which lead to the total spring constant

$$k = 2(k_1 + k_2) = 3.202N/m \tag{4.3}$$

After obtaining the total spring constant, the pull-in voltage can be determined next. The typical micro plate dimension is 350 μm long x 350 μm wide. According to the MUMPs process characteristic, we can also obtain that $g_0 = 2.75\mu m$. Thus from Equation (2.32) we can obtain

$$V_{PI} = \sqrt{\frac{8kg_0^{\ 3}}{27\varepsilon A}} = \sqrt{\frac{8\times 3.202\times (2.75\times 10^{-6})^3}{27\times 8.854\times 10^{-12}\times (350\times 10^{-6})^2}} \approx 4.27V \tag{4.4}$$

After analytical calculations and experimental observations, we summarize some possible reasons of short circuit: on one hand, from the previous calculation of pull-in voltage, we know the expected pull-in voltage of the typical device is around 4.27 *V*. Although some dimples are designed underneath the movable plate to isolate the movable plate and the ground plane from being shorted, it is reasonable to deduce that nonlinearly deforming or some unexpected things will be happening if applying much more voltage

than 4.27 *V* to the device.

On the other hand, as shown in Fig. 4.14, the nearest vertically projected spacing between the designed spring and the ground plate is just 1 μm. While the voltage is applied to the device, the spring is flexed down by electrostatic force. At one certain voltage value its flexure made it unexpectedly contact the ground plane to shorten the circuit. In addition, because of the self-mass of the larger movable plate, the springs have been drawn down a bit in advance before applying the voltage. These reasons caused the unexpected contact and thus led to the short circuit phenomenon.

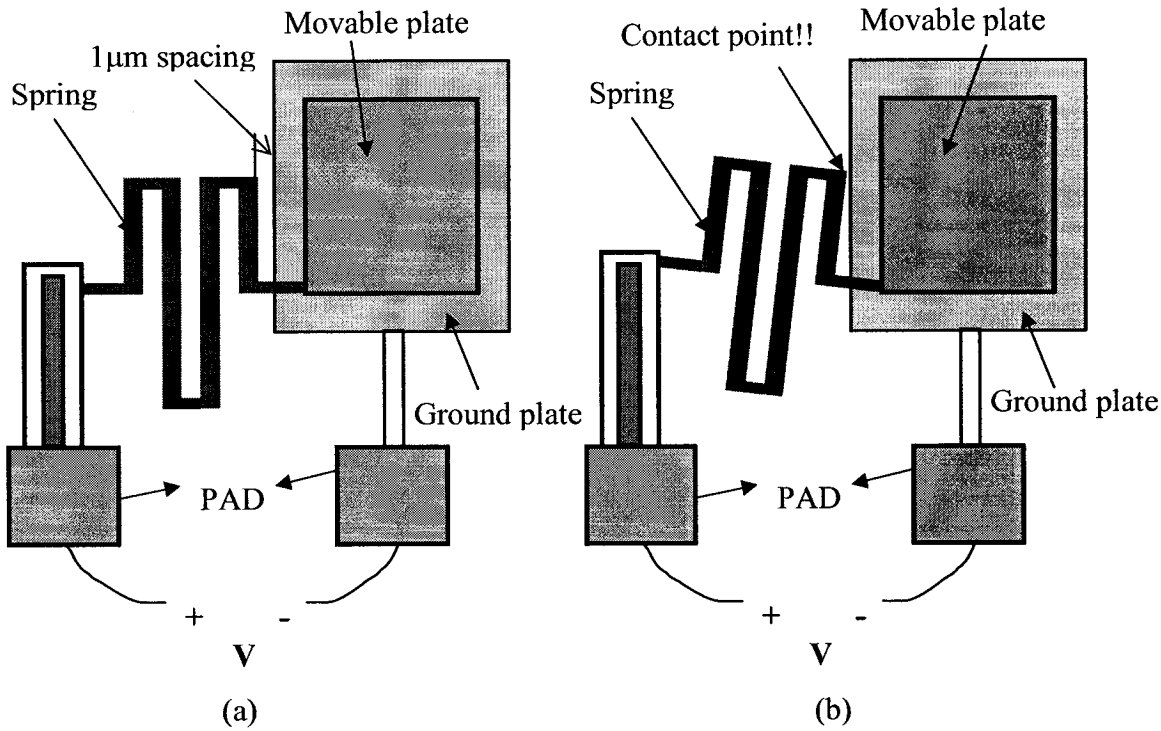

Figure. 4.14. Schematic of spring design problem of the device (Top view). (a) Before applying voltage. (b) After applying some voltage.

4.2.3 Design Modifications

Based on the experiment phenomena and release results of the devices fabricated on the previous runs, some modifications have been proposed as follows:

- Adding HOLEM on metal layer for easy post processing release.
- Reduce the area of the micro plate to reduce the effect of the mass of it; use rectangular shape instead of square shape to improve it initial actuation.
- Change the size and position of the micro springs. The two near the cantilever beam will be smaller and simpler which have smaller spring constant; the other two will be a little bit larger, but smaller than previous design. Besides, the position of the springs near the cantilever beam can be adjusted to improve the initial actuation.
- Increase the distance between the springs and the ground plane (POLY0 layer) to reduce the possibility of short circuit.
- Design POLY0 layer underneath the micro springs to make the spring surface smoother and flatter.
- Use POLY0 layer to make wires connecting PAD and the related structural layers to eliminate the possible disconnection between wires and PAD due to the broken wires. Increase the size of the pad to make measurement easy.

Chapter 5 Conclusions

In this thesis, we have studied and analyzed some fundamental physical and mechanical properties of an electrostatically driven micro actuator comprising a micro plate and a cantilever beam associated with thin film stresses. We investigated the mechanical and physical properties of the individual parts, the cantilever beam and the micro plate.

Prior to fabrication of the devices, the proposed devices were modeled and simulated. Firstly the cantilever beam with thin film stresses was modeled and simulated to explore the effect of the thin film stress on the microstructure. We elaborated the relationship between the end deflection of the cantilever beam and the geometric dimensions of the cantilever beam, and concluded that the end deflection increases much more rapidly with beam length increase than with beam width increase. Furthermore, we developed simulation solutions which correctly predicted and estimated the practical deflections of the cantilever beam due to the preloaded thin film residual stress. To the best of our knowledge, these results have not been previously reported in the literature.

We then performed coupled-field electrostatic-structural FEM analyses to obtain some electrostatic and mechanical properties of the cantilever beam and the micro plate. We performed several coupled-field electrostatic-structural FEM analyses according to different geometries of the micro plate and obtained some displacement profiles of the

micro plate. Our investigations show that micro plates with rectangular shape transfer the initial actuation to the cantilever beam much better than those with square shape.

The designed devices were fabricated using MUMPs technology and then the post-processing was performed. Based on some important HF release phenomena, we summarized that HF release is a very sensitive process. The different release time influences the primary physical properties of the devices, such as the color, the vertical deflection due to thin film stress, the layer thickness, the surface profile, etc. Also it was found that the release is dependent on the release temperature, clean room conditions, and the person who perform the release, etc.

Finally the fabricated devices were tested and their functions were observed in our lab. The experimental results proved that the modeling results correctly predicted and estimated the practical effect of the thin film stress. The movement of the devices has been observed in our lab, the designs of some key parts are proven to be reasonable and feasible, such as micro shutter, and micro hinges. However we did not obtain the data of the exact vertical displacement of the electrostatically driven micro actuator due to the limited conditions in our lab.

The main contributions of this research work are listed as follows:

- Design of a generic electrostatically driven micro actuator consisting of a micro plate and a cantilever beam associated with thin film stress.
- Fabrication of the designed devices in a standard surface micromachining

process technology with post-processing.

- Summary of the basic design procedures for the cantilever beam with thin film stress.
- Analysis, design and layout of an out-of-plane micro shutter based on a standard surface micromachining process technology.
- Demonstrated vertical displacement of the designed electrostatically driven micro actuators.
- Investigation of the effect of thin film stresses on surface micromachined bi-layers. Analytical results and FEM modeling results match the experimental results.

As this research work is part of an on-going research program, some suggestions and proposals have been proposed as follows for the future research:

- Modifications to the device structure have been proposed for performance improvement. More attention needs to be paid on the design of the micro plate, the connection mechanism, and the micro shutter.
- Investigation on how the different post-processing conditions, such as release time and etchants, influence the mechanical and physical properties of the devices.
- Development of FEM modeling for the pull-in voltage of large dimension electrostatically driven microstructures. Development of FEM modeling for the

performance of different connection mechanisms used for connecting micro plate and the cantilever beam.

- Development of FEM modeling for the natural frequency of the micro plate and the whole microstructures.
- Research on how the initial thin film stresses change the pull-in voltage of microstructures and how they influence the relationship of end displacement and applied voltage.

References

[1] Stephen D., Senturia, *Microsystem Design*, Kluwer Academic Publisher, Norwell, 2001.

[2] David A. Koester, R. Mahadevan, Busbee Hardy, and Karen W. Markus, *MUMPs Design Handbook (Revision 7.0)*, Cornos Integrated Microsystems, A JDS Uniphase Company, Research Triangle Park, NC 27709.

[3] Kovacs, G T A, Maluf, N I, Petersen, K E, "Bulk micromachining of silicon," *Proc. IEEE*, Vol. 86, (8), pp. 1536–1551, 1998.

[4] Sergej Fatikow and Ulrich Rembold, *Microsystem Technology and Microrobotics*, Springer, New York, 1997.

[5] Defense Advanced Research Projects Agency (DARPA), http://www.darpa.mil/MTO/

[6] Smith, J H, Montage, S and Sniegowski, J J, "Material and processing issues for the monolithic integration of microelectronics with surface-micromachined polysilicon sensors and actuators," *Proc. SPIE*, Vol. 2639, 1995.

[7] Http://www.luncent.com

[8] Shi-sheng Lee, Ming C. Wu, UCLA, 1998.

[9] Http://www.memrus.com

[10] A. Q. Liu, Nanyang Technological University, Singapore.

[11] C.T.C. Nguyen, et al., IEEE Trans. MTT, 1999.

[12] Schmidt, M A, 'Wafer-to-wafer bonding for microstructure formation,' *Proc. IEEE*, 86 (8), pp. 1575–1585, 1998.

[13] Madou, M, *Fundamentals of microfabrication*, CRC Press, Boca Raton, Fla., 1997.

[14] Young, W., *Roark's Formulas for Stress and Strain*, 6th edition, McGraw-Hill, 1989.

[15] Michael W. Judy, Young-Ho Cho, Roger T. Howe, and Albert P. Pisano, "Self-Adjusting Microstructures (SAMS)," *Proceedings IEEE Micro Electro Mechanical Systems,* pp. 51-56, Nara, Japan. Jan. 1991.

[16] Chia-Lun Tsai and Albert K. Henning, "Out-of-plane microstructures using stress engineering of thin film," *Proceedings of the SPIE-The International Society for Optical Engineering*, Vol. 2639, pp. 124-132, 1995.

[17] Joseph H. Faupel, Franklin E. Fisher, "*Engineering design: a synthesis of stress analysis and materials engineering*," 2nd Edition, John Wiley & Sons, New York, 1981.

[18] William N. Sharpe, Jr., Bin Yuan, Ranji Vaidyanathan, and Richard L. Edwards, "Measurements of Young's Modulus, Possion's Ratio, and Tensile Strength of Polysilicon", *Proceedings of the Tenth IEEE International Workshop on Microelectromechanical Systems*, pp. 424-429, Nagoya, Japan, 1997.

[19] http://www.kasap.usask.ca/server/kasap/Tables/Mechanical.html

[20] http://www.matweb.com/search/SpecificMaterial.asp?bassnum=MEAu00

[21] Vamsee K. Pamula, Anand Jog, and Richard B. Fair, "Mechanical Property Measurement of thin-film gold using thermally actuated bumetallic cantilever beams", *Modeling and Simulation of Microsystems 2001.*

[22] K. S. J. Pister, M. W. Judy, S. R. Burgett, and R. S. Fearing, "Microfabricated hinges," *Sensors and Actuators A: Physical*, Vol. 33, no. 3, pp. 249-256, 1992.

[23] M. C. Wu, L.-Y. Lin, S.-S. Lee, K. S. J. Pister, "Micromachined free-space integrated micro-optics," *Sensors and Actuators A: Physical*, Vol. 50, no. 1-2, pp. 127-134, Aug. 1995.

[24] M. C. Wu, "Micromachining for Optical and Optoelectronic Systems," *Proceedings of the IEEE*, Vol. 85, No. 11, pp. 1833-56, Nov. 1997.

[25] Gary J. O'Brien, David J. Monk, and Liwei Lin, "MEMS cantilever beam electrostatic pull-in model", Proceedings of SPIE, Vol. 4593, pp. 31-41, 2001.

[26] R. T. Chen, H. Nguyen, M. C. Wu, "A High-Speed Low-Voltage Stress-Induced Micromachined 2 x 2 Optical Switch," *IEEE Photonics Technology Letters*, Vol. 11, No. 11, pp. 1396-98, Nov. 1999.

[27] R. T. Chen, H. Nguyen, M. C. Wu, "A Low Voltage Micromachined Optical Switch by Stress-Induced Bending," *12th IEEE Micro Electro Mechanical Systems International Conference, MEMS'99*, pp. 424-428, 17-21 Jan. 1999.

[28] B. Barber, C. R. Giles, V. Aksyuk, R. Ruel, L. Stulz, and D. Bishop, "A Fiber Connectorized MEMS Variable Optical Attenuator," *IEEE Photonics Technology Letters*, Vol. 10, No. 9, pp. 1262-64, Sept. 1998.

[29] V. Aksyuk, C. R. Giles, A. Dentai, E. C. Burrus, C. A. Burrus, L. Stulz, D. Bishop, "Optically-powered optical power limiter for use in lightwave networks," *MEMS'99, The 12th IEEE Micro Electro Mechanical Systems International Conference,* pp. 344-348, 17-21 Jan. 1999.

[30] C. R. Giles, V. Aksyuk, B. Barber, R. Ruel, L. Stulz, and D. Bishop, "A Silicon MEMS Optical Switch Attenuator and Its Use in Lightwave Subsystems," *IEEE Journal of Selected Topics in Quantum Electronics*, Vol. 5, No. 1, pp. 18-25, Jan./Feb. 1999.

[31] V. Aksyuk, B. Barber, C. R. Giles, R. Ruel, L. Stulz, and D. Bishop, " Low Insertion Loss Packaged and Fiber-Connectorized Surface-Micromachined Reflective Optical Switch," *Solid-State Sensor and Actuator Workshop*, Hilton Head Island, South Carolina, pp. 79-82, June 8-11, 1998.

[32] H. C. Nathanson, W. E. Newel, R. A. Wickstrom, and J. R. Davis, "The Resonant Gate Transistor," *IEEE Transaction on Electron Devices*, Vol. ED-14, No. 3, pp. 117-133, 1967.

[33] K. E. Petersen, "Dynamic Micromechanics on Silicon, Techniques and Devices," *IEEE Transaction on Electron Devices*, Vol. ED-25, No. 10, pp. 1241-1250, 1978.

[34] Rick Clayton, "Integrated Optoelectronics," *GaAs MANTECH, Inc.*, 2001.

[35] Kevin Affolter, "Integrating Active Components Improves System Design," *WDM Solutions - wavelength division multiplexing,* Pennwell Corp., June. 2001.

[36] John D. Grade, and Hal Jerman, "MEMS Electrostatic Actuators for Optical Switch Applications," OPA-Optical Society of America, pp. WX2-1, 2000.

[37] Cornel Marxer, Patrick Griss, and Nicolaas F. de Rooij, "A Variable Optical Attenuator Based on Silicon Micromechanics," *IEEE Photonics Technology Letters*, Vol. 11, No. 2, pp. 233-35, Feb. 1999.

[38] Neilson, D.T., "Micromachines for optical networking," *Lasers and*

Electro-Optics Society, 2001 (LEOS 2001), The 14th Annual Meeting of the IEEE, Vol. 1, No. 7, pp. 12-13, Nov. 2001.

[39] Wen-Hwa Chu, Mehran Mehregany, and Robert L Mullen, "Analysis of tip deflection and force of a bimetallic cantilever microactuator", *J. Micromechanics and Microengineering*, Vol. 3, pp. 4-7, 1993.

[40] M. Adrian Michalicek, Darren E. Sene, and Victor M. Bright, "Advanced Modeling of Micromirror Devices", *International Conference on Integrated Micro/Manotechnology for Space Applications*, pp. 214-229, 1995.

[41] Tze-Wei Yeow, K. L. Eddie Law, and Andrew Goldenberg, "MEMS Optical Switches," *IEEE Communication Magnizine*, Nov. 2001.

[42] Katsuhiko Hirabayashi, Masato Wada, and Chikara Amano, "Liquid Crystal Variable Optical Attenuators Integrated on Planar Lightwave Circuits," *IEEE Photonics Technology Letters,* Vol. 13, No. 6, June 2001.

[43] Nabeel A. Riza, Zahid Yaqoob, "Submicrosecond Speed Variable Optical Attenuator Using Acoustooptics," *IEEE Photonics Technology Letters,* Vol. 13, No. 7, July 2001.

[44] M. J. Mughal and N. A. Riza, "Compact Acoustooptic High-Speed Variable Attenuator for High-Power Applications," *IEEE Photonics Technology Letters,* Vol. 14, No. 4, April 2002.

[45] http://www.mece.ualberta.ca/tutorials/ansys/.

[46] http://www.darpa.mil/.

[47] Peterson, K E, "Silicon as a mechanical material," *Proc. IEEE*, pp.420-457, Vol. 70, 1982.

[48] Aeidel, H, "The mechanism of anisotropic silicon etching and its relevance for micromachining," *Proceedings of the international conference on Solid-State Sensors and Actuators*, Tokyo, Japan, pp. 120-125, 1987.

[49] Shaw, K W, Zhang, Z L andMacDonald, N C, "SCREAM: a single mask, single-crystal silicon, reactive ion etching process for microelectromechanical structures," *Sensors and Actuators A*, Vol. 40, pp. 63-70, 1994

[50] Bryzek, J, Peterson, K and McCulley, W, "Micromachines on the march," *IEEE*

Spectrum, pp. 20-31, May 1994.

[51] Kovacs, G.T.A., *Micromachined Transducers Sourcebook*, McGraw-Hill, New York, NY, 1998.

[52] University of Stanford, http: // www.stanford.edu /group/ SML/ee321/ ho/ MEMS-01-intro.pdf.

[53] Lin, L Y, Lee, S S, Wu, M C and Pister, K S J, "Micromachined integrated optics for free space interconnection," *Proc. IEEE MEMS*, pp. 77-82, 1995.

[54] J.E. Shigley and L. D. Mitchell, *Mechanical Engineering Design*, Mcgraw-Hill, New York, 1983.

[55] Ansys Training Manual – Multiphysics Simulation for MEMS, Jan., 2003

Appendices

Appendix A: Basic mechanical theories of MEMS actuators

1 Stress and Strain for Isotropic Materials [1]

Stress is defined as the force per unit area acting on the surface of a differential volume element of a solid body. $\sigma_x, \sigma_y, \sigma_z$ denote individually normal stresses perpendicular to the differential face shown as Fig. 1.

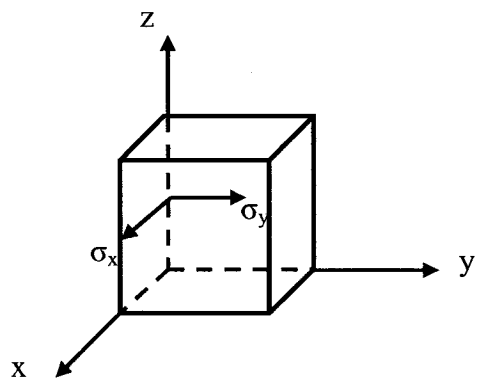

Figure 1. Normal stresses on a solid volume (the stress in z directions is not included).

If a force is applied to a solid body, it will deform. The differential deformation is called strain denoted as ε_x, expressed as change in the length per unit length. The stress and strain of isotropic materials do not change with direction due to internal ordering of the structure. Therefore for an isotropic material, a uniaxial stress results in a uniaxial strain proportional to the stress.

1.1 Some Concepts

- Young's Modulus

Isotropic materials are those with no internal ordering or structure that would make the stress-strain responses depend on direction. For these materials, a uniaxial stress results in a uniaxial strain that is proportional to the stress. The proportional constant is called Young's modulus, denoted by E, and expressed as:

$$E = \frac{\sigma_x}{\varepsilon_x} \tag{1}$$

- Poisson's Ratio

Tensile stress in x direction results in compressive stress (strain) in y and z direction (object becomes longer and thinner). The ratio of y and x direction strain is call Poisson's Ratio:

$$\nu = -\varepsilon_y / \varepsilon_x \tag{2}$$

- Plane Stress

In MEMS devices, there exists some special plane stress in thin film materials when they are deposited or formed on a substrate. This kind of plane stress is brought out either from the details of the deposition process or from mismatches in thermal expansion between the film and the substrate. The equations expressing the plane stress are

$$\varepsilon_x = \frac{1}{E}(\sigma_x - \nu\sigma_y), \quad \varepsilon_y = \frac{1}{E}(\sigma_y - \nu\sigma_x) \tag{3}$$

1.2 Axial Stress and Strain

Fig. 2 is a slender beam with rectangular cross section loaded with a uniform axial stress on its end faces. The length of the beam is L, the width is W, the thickness is H, and

the force applied on the end of beam is F.

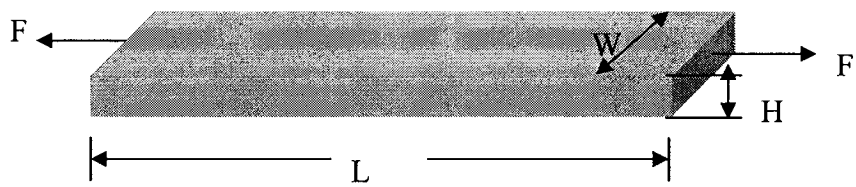

Figure 2. Slender beam with rectangular cross section loaded with a uniform axial stress.

Providing F is distributed as uniform tensile stress acting on the ends of the beam, we can obtain:

$$\sigma = \frac{F}{A} = \frac{F}{WH} \tag{4}$$

where σ is the thin-film axial stress, F is the force applied to surface, A is the cross section area of the beam, W and H are geometries dimension of the beam.

According to basic elastic knowledge, under the action of the axial load, the beam will extend. The strain created by the axial stress is

$$\varepsilon = \frac{1}{E}\sigma = \frac{F}{EWH} \tag{5}$$

where E is called Young's modulus.

And we also know the relationship between the beam length and the corresponding change in its length is $\varepsilon = \frac{\Delta L}{L}$, where ε is the strain, the ratio of deformation to length, L is the original length of the beam.

1.3 Spring Constant

If the beam functions as a spring element in a mechanical structure, under ideal condition, it will exhibit a proportional relationship between force and extension as the following form $F = k\Delta x$, where k is the spring constant, and Δx is the extension. Thus, from Equation (5), we can derive that

$$k = \frac{F}{\Delta x} = \frac{\sigma WH}{\varepsilon L} = E\frac{WH}{L} = E\frac{A}{L} \tag{6}$$

If the applied beam has a non-uniform cross-section, by applying a total force on the ends of it, the uniform force distribution across the area can approximately represent a uniform axial stress. Therefore we could solve it as

$$\Delta(dx) = \frac{Fdx}{EA(x)}$$

where $A(x)$ is the position-dependent cross-section area of the beam, leading to

$$\Delta L = \int_0^L \Delta(dx) = \int_0^L \frac{F}{EA(x)}dx$$

Thus the spring constant for the non-uniform beam is

$$k = \frac{F}{\Delta L} = \left[\int_0^L \frac{dx}{EA(x)}\right]^{-1} \tag{7}$$

2 Bending Properties of Cantilever Beam [1]

A beam with a fixed support and a free end is called cantilever beam. The behavior of a fixed support is that the beam cannot move vertically or horizontally at the support, nor can it have non-zero slope at the support shown as Fig. 3.

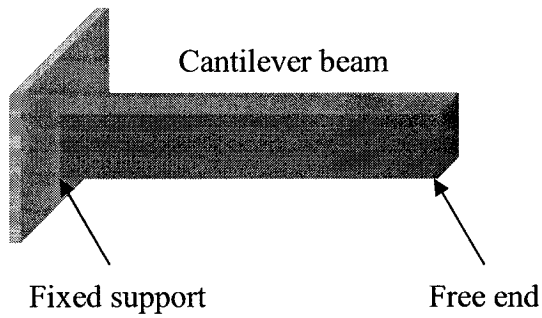

Figure 3. Schematic of a cantilever beam.

2.1 Reaction Forces and Moments of Bending Beams

Transverse loading of beams can cause them to bend. There are two basic types of external transverse loads that can be applied to beams. One is called point load which can be applied at any position along the length of the beam (shown as Fig. 4a), the other is called distributed load applied to a portion of the beam length (shown as Fig. 4b).

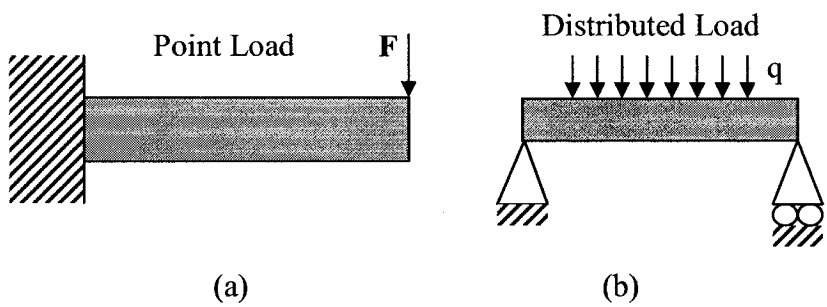

Figure 4. Two types of transverse loads applied to cantilever beam. (a) Point load, (b) Distributed load.

The total moment acting about a point is the sum of all forces weighed by their distance from that point. Referring to the Fig. 5 and using free end as a reference, one can

obtain the total moment acting on the beam is

$$M_T = M_R - F_R L \tag{8}$$

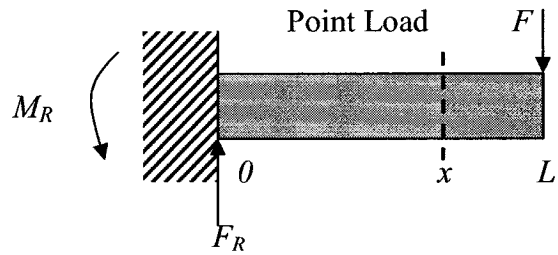

Figure 5. The total moment applied on the bending beam.

At static equilibrium condition of the bending beams, $M_T = 0$, so that

$$M_R = F_R L = FL \tag{9}$$

This equation establishes the values of the reaction forces and moments needed to assure static equilibrium.

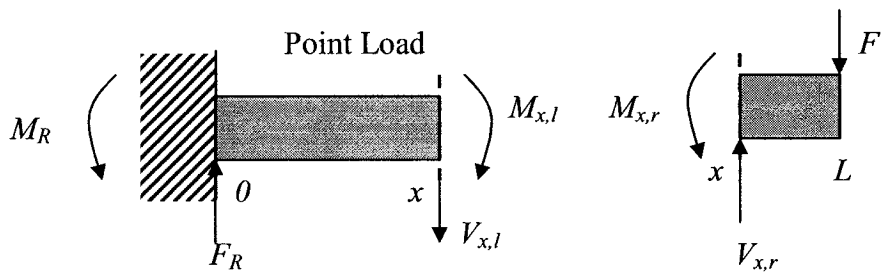

Figure 6. Schematic of the bending beam divided at position *x*.

If we hypothetically divide the beam into two parts at position x as Fig. 6, in order for both parts to be in static equilibrium, we must have

$$M_{x,l} = M_{x,r} = F(L - x) \tag{10}$$

Above analysis indicates that the equilibrium constraints (total force is zero, and total moment is zero) are applied anywhere in the beam.

2.2 Bending of a Transversely Loaded Beam [14]

Figure 7 illustrates a small section of a beam that has become bent after application of a transverse load. The applied moment M_0 is positive, the radius of curvature is ρ. The dash arc in the middle of the beam is known as the neutral axis. It is the axis whose length will stay unchanged before and after the bending. Portions of the beam above the neutral axis are extended longer in tension, whereas portions below the neutral axis are forced into compression by the bending.

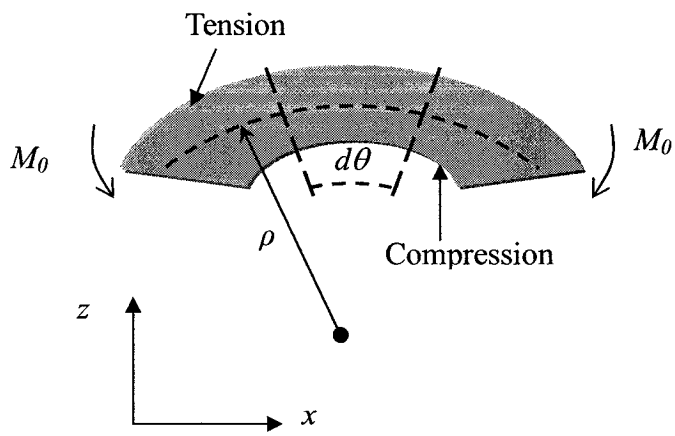

Figure 7. A small bending section of transversely loaded beam.

We define a coordinate system on the underformed beam where x is the distance along the length of the beam and z is the vertical distance above the neutral axis of the

beam. If the thickness of the beam is denoted as H, then we see that z varies from $-H/2$ to $H/2$.

From geometrical arguments we can show that the axial strain as a function of position along the beam at position z is

$$\varepsilon(x,y,z) = \varepsilon(x) = \frac{z}{\rho(x)} \tag{11}$$

where the radius varies as a function of position along the length of the beam.

From Equation (1), we can write an expression for the stress (in the x direction) as a function of position along the beam

$$\sigma_{xx}(x,y,z) = E\frac{z}{\rho(x)} \tag{12}$$

Note carefully that the upper part of the beam (positive z) is in tension, while the lower part of the beam (negative z) is in compression.

Integrating over the cross-section of the beam we can obtain the total internal bending moment $M(x)$:

$$M(x) = \int_{-H/2}^{H/2} Wz\sigma_{xx}dz = \int_{-H/2}^{H/2} \frac{EWz^2}{\rho(x)}dz = (\frac{WH^3}{12})\cdot\frac{E}{\rho(x)} \tag{13}$$

which is the relationship between internal bending moment and curvature of beams, and is usually written as

$$\frac{1}{\rho(x)} = \frac{M(x)}{EI(x)} \tag{14}$$

where ρ is the radius of curvature, $M(x)$ is internal bending moment, and

$$I(x) = \frac{WH^3}{12} \tag{15}$$

is the moment of inertia of the beam cross-section. The beam cross-sectional geometry can vary slowly as a function of position along the beam, making I a function of x. In principle, E can also be a function of x. Discontinuities or rapid changes in the cross section require more detailed modeling.

For small angle bending of slender beams, the curvature of the beam is approximately the second derivate of the position of the neutral axis $y(x)$ with respect to a fixed coordinate system x:

$$\frac{1}{\rho} = \frac{\frac{d^2y}{dx^2}}{\left(1+\left(\frac{dy}{dx}\right)^2\right)^{3/2}} \approx \frac{d^2y}{dx^2}$$

from which we see that

$$\frac{d^2y}{dx^2} \approx \frac{M(x)}{EI} \tag{16}$$

From Equation (10) and Equation (16), we can leads to

$$\frac{d^2y}{dx^2} \approx \frac{F(l-x)}{EI} \tag{17}$$

The cantilevered beam implies a boundary condition of

$$y(0) = 0, \left.\frac{dy}{dx}\right|_{x=0} = 0$$

After solving the above differential equation, finally we obtain that the maximum

deflection at the end of the cantilever is

$$y_{\max} = \left(\frac{L^3}{3EI}\right)F$$

If this maximum deflection were a key displacement in a device, we could assign spring constant to this cantilever of

$$k = \frac{EH^3W}{4L^3} \tag{18}$$

3 Bending Properties of The Micro Plate [1]

Beams are the kind of structures whose transverse dimensions are much smaller than the length. When a structure has transverse dimensions comparable to the length, it is altered to be a plate structure, which can be described with full three-dimensional theories.

The bending behavior of plates can be extended from bending of beams. Plates have two principle radii of curvature expressed in principle axis coordinates. The radii of curvature can be expressed as

$$\frac{1}{\rho_x} = \frac{\partial^2 \delta}{\partial x^2}, \frac{1}{\rho_y} = \frac{\partial^2 \delta}{\partial y^2} \tag{19}$$

where $\delta(x,y)$ is the deflection of the plate.

The bending strains of per unit width of plate are

$$\varepsilon_x = -\frac{z}{\rho_x}, \varepsilon_y = -\frac{z}{\rho_y} \tag{20}$$

From Equation (3), (19) and (20), we can obtain

$$\sigma_x = -\frac{Ez}{1-\nu^2}\left(\frac{1}{\rho_x}+\frac{\nu}{\rho_y}\right),\quad \sigma_y = -\frac{Ez}{1-\nu^2}\left(\frac{1}{\rho_y}+\frac{\nu}{\rho_x}\right) \tag{21}$$

And the bending moments per unit width are determined as

$$M'_x = -D\left(\frac{1}{\rho_x}+\frac{\nu}{\rho_y}\right),\ M'_y = -D\left(\frac{1}{\rho_y}+\frac{\nu}{\rho_x}\right) \tag{22}$$

where D, called flexural rigidity of the plate, is given by

$$D = \frac{1}{12}\left(\frac{EH^3}{1-\nu^2}\right)$$

and where H is the thickness of the plate.

Appendix B: Modeling Solutions Programmed by ANSYS

Appendix B-1: Modeling initial stress of designed device

```
/PMETH,OFF,1
KEYW,PR_SET,1
KEYW,PR_STRUC,1
KEYW,PR_ELMAG,1
KEYW,MAGELC,1
KEYW,PR_MULTI,1
/GO
/title, Modeling of thin film stress of the cantilever beam
*SET,poly_width,60
*SET,metal_width,52
*SET,poly_length,520
*SET,lp,20
/PREP7
BLC4,0,0,poly_length,1.5
BLC4,lp,1.5,poly_length-lp,0.5
AGLUE,all
ET,1,PLANE182
KEYOPT,1,1,0
KEYOPT,1,3,3
KEYOPT,1,4,0
KEYOPT,1,6,0
KEYOPT,1,10,0
R,1,poly_width
R,2,metal_width
MP,EX,1,169e+3
MP,PRXY,1,0.23
MP,DENS,1,2.33e-15
MP,EX,2,78.5e+3
MP,PRXY,2,0.42
MP,DENS,2,19.3e-15
asel,s,loc,x,0,poly_length
asel,r,loc,y,0,1.5
cm,poly_a,area              ! poly material layer
AATT,1,1,1,0
```

```
asel,s,loc,x,lp,poly_length
asel,r,loc,y,1.5,2
cm,metal_a,area              ! metal material layer
AATT,2,2,1,0
alls

SMRT,6
MSHAPE,0,2D
MSHKEY,0
FLST,5,2,5,ORDE,2
FITEM,5,3
FITEM,5,-4
CM,_Y,AREA
ASEL,,,,P51X
CM,_Y1,AREA
CHKMSH,'AREA'
CMSEL,S,_Y
AMESH,_Y1
CMDELE,_Y
CMDELE,_Y1
CMDELE,_Y2
/SOLU
LSEL,S,LOC,X,0
DL,ALL, ,ALL,0

ANTYPE,0
NLGEOM,1
NROPT,AUTO, ,
LUMPM,0
EQSLV, , ,0,
PRECISION,0
MSAVE,0
PIVCHECK,1
SSTIF,ON
TOFFST,0,
ISFILE,READ, thesis_initial_stress, ist, ,0
/STATUS,SOLU
SOLVE
```

```
FINISH
/POST1
SET,LAST
/EFACE,1
AVPRIN,0, ,
PLNSOL,U,Y,0,1
```

Appendix B-2: Creating the initial stress file of modeled device

```
esel,s,elem,,1,1067       ! The element range of material 1
cm,first,elem
SXX='-15'                 ! The initial residual stress of material 1
SYY=0
SZZ=0
SXY=0
SYZ=0
SXZ=0
*cfopen,,ist
cm, alle, elem
*get, nummer, elem, ,count
*do, loop,1,nummer
*get, maks, elem, , num, max
esel, ,elem, ,alle
esel, u, elem, ,maks
cm, alle, elem
*cfwrite, eis, maks,0
*cfwrite, sxx, syy, szz, sxy, syz, sxz
*enddo

esel,s,elem,,1068,2455     ! The element range of material 2
cm,first,elem
SXX='73'                   ! The initial residual stress of material 2
SYY=0
SZZ=0
SXY=0
SYZ=0
SXZ=0
*cfopen,,ist
cm, alle, elem
```

```
*get, nummer, elem, ,count
*do, loop,1,nummer
*get, maks, elem, , num, max
esel, ,elem, ,alle
esel, u, elem, ,maks
cm, alle, elem
*cfwrite, eis, maks,0
*cfwrite, sxx, syy, szz, sxy, syz, sxz
*enddo
```

Appendix B-3: Parts of initial stress results created by Appendix B-2

```
.....
eis,480,0
-15,0,0,0,0,0
eis,479,0
-15,0,0,0,0,0
eis,478,0
-15,0,0,0,0,0
eis,477,0
-15,0,0,0,0,0
eis,476,0
-15,0,0,0,0,0
eis,475,0
-15,0,0,0,0,0
eis,474,0
-15,0,0,0,0,0
eis,473,0
-15,0,0,0,0,0
eis,472,0
-15,0,0,0,0,0
eis,471,0
-15,0,0,0,0,0
eis,470,0
-15,0,0,0,0,0
eis,469,0
-15,0,0,0,0,0
eis,468,0
-15,0,0,0,0,0
```

```
eis,467,0
73,0,0,0,0,0
eis,466,0
73,0,0,0,0,0
eis,465,0
73,0,0,0,0,0
eis,464,0
73,0,0,0,0,0
eis,463,0
73,0,0,0,0,0
eis,462,0
73,0,0,0,0,0
eis,461,0
73,0,0,0,0,0
eis,460,0
73,0,0,0,0,0
eis,459,0
.....
```

Appendix B-4: The electrostatic-structural analysis of the micro plate

```
/COM,
/COM,Preferences for GUI filtering have been set to display:
/COM,   Structural
/COM,   High Frequency
/COM,   Electric

v_in = 40
coef = 1
wp   = 150   ! width of plate
lp   = 200    ! length of plate
tp   = 1.5     ! thickness of plate
gap = 2.75    ! air gap
wb   = 2     ! width of beam
lb   = 10     ! length of beam

/prep7
emunit,epzro,8.854e-6   ! Define free-space permittivity
```

```
! CREATE VOLUMES FOR BEAM AND MIRROR
block,0,lp/coef,0,-tp,0,wp/2
block,0,lp/coef,0,-tp,0,-wp/2
block,0,wb,0,-tp,wp/2,wp/2+lb
block,0,wb,0,-tp,-wp/2,-wp/2-lb
block,lp,lp-wb,0,-tp,wp/2,wp/2+lb
block,lp,lp-wb,0,-tp,-wp/2,-wp/2-lb
nummrg,kp

! *****************
! DEFINE COMPONENTS
! *****************
asel,s,loc,x,lp/coef
cm,symm_a,area

asel,s,loc,x,0,wb
asel,r,loc,y,0,-tp
asel,r,loc,z,wp/2+lb
cm,fixed_area1,area

asel,s,loc,x,0,wb
asel,r,loc,y,0,-tp
asel,r,loc,z,-wp/2-lb
cm,fixed_area2,area

asel,s,loc,x,lp,lp-wb
asel,r,loc,z,wp/2+lb
asel,r,loc,y,0,-tp
cm,fixed_area3,area

asel,s,loc,x,lp,lp-wb
asel,r,loc,z,-wp/2-lb
asel,r,loc,y,0,-tp
cm,fixed_area4,area

! ASSIGN ATTRIBUTES
vsel,all
vatt,1,,1
```

```
et,1,45
mp,ex,1,169e3              ! Material 1 is Silicon
mp,prxy,1,0.23
mp,dens,1,2.33e-15     ! (kg/mu^3)   density
mp,damp,1,9.3e-8         ! (kg*mu^2/s*rad)   damping coefficient

md = 0.5   ! mesh density parameter (0.5-coarse; 2-very fine)

! MESH MODEL
lsel,s,length,,lp/coef
lesize,all,,,20/coef*md
lsel,s,length,,wp/2
lesize,all,,,6*md
lsel,s,length,,tp
lesize,all,,,3*md
lsel,s,length,,wb
lesize,all,,,3*md
lsel,s,length,,lb
lesize,all,,,10*md
alls
vmesh,all

CMSEL,S,FIXED_AREA1
CMSEL,A,FIXED_AREA2
CMSEL,A,FIXED_AREA3
CMSEL,A,FIXED_AREA4
DA,ALL,ALL,0

asel,s,loc,z,-wp/2,wp/2
asel,r,loc,y,-tp
nsla,s,1
cm,trano,node
alls

EMTGEN,'trano','emtelm','emtpno', 'uy',-2.75,0.10,0.10,8.854e-6

/solu
nsel,s,loc,y,-tp-gap
d,all,volt,0
```

```
d,all,uy,0
cmsel,s,trano
d,all,volt,v_in
nsel,s,loc,y,-tp-gap
ic,all,volt,v_in/10
alls


ANTYPE,static
OUTRES,ALL,ALL
EQSLV,SPAR
NLGEOM,ON
AUTOTS,ON

TIME,v_in
NSUBST,10,100,3,1
assopt,frontal

/STATUS,SOLU
SOLVE

ESEL,S,TYPE,,1
NSLE,S
SET,LAST
/VIEW,,1
/ANG,1
PLDISP,2

/post26
*SET,nc,node(lp,-tp,wp/2)
nsol,2,nc,u,y
/axlab,x,Applied Voltage
/axlab,y,Displacement of Center-topend
plvar,2
```

Appendix B-5: The electrostatic-structural analysis of the cantilever beam

```
/COM,
```

```
/COM,Preferences for GUI filtering have been set to display:
/COM,   Structural
/COM,   Electric

*SET,beam_l,400          ! beam length
*SET,beam_h,1.5          ! beam thickness
*SET,beam_w,30           ! beam width
*SET,air_gap,2.75        ! gap over ground plane
*SET,target_off,0.1      ! offset of target surface from bottom electrode

/prep7
rect,0,beam_l,air_gap,air_gap+beam_h    ! beam
rect,0,beam_l,0,air_gap                 ! air gap
aglue,all
nummrg,kp
numcmp,all

asel,s,loc,x,0,beam_l
asel,r,loc,y,air_gap,air_gap+beam_h
aatt,2,,2                ! beam
lsla
lsel,s,loc,x,0,beam_l
lsel,r,loc,y,air_gap
cm,te_l,line             ! top electrode
lsel,s,loc,x,0,beam_l
lsel,r,loc,y,0
cm,be_l,line             ! bottom electrode

asel,s,loc,x,0,beam_l
asel,r,loc,y,0,air_gap
cm,gap_a,area            ! air gap
aatt,1,,1
lsla
lsel,s,loc,x,0,beam_l
lsel,r,loc,y,air_gap
cm,cont_l,line           ! contact line
latt,3,1,3

lsel,s,loc,x,0,beam_l
```

```
lsel,r,loc,y,0
lgen,2,all,,,0,target_off   ! create target line
lsel,s,loc,y,target_off
lreverse,all                ! reverse the direction of the target line
cm,targ_l,line              ! target line
latt,3,1,4
alls

et,1,200,7
et,2,200,7
et,3,200,1
et,4,200,1

md = 2          ! Mesh Density
esize,(2.8/2)/md
mshkey,1
amesh,all

cmsel,s,cont_l
cmsel,a,targ_l
lmesh,all

cmdele,cont_l
cmdele,targ_l

/title, Electrostatic-Structural analysis of the cantilever beam
/prep7
ET,1,0
ET,2,PLANE82,,,2
ET,3,CONTA172,,1
ET,4,TARGE169

MP,EX,2,169e3
MP,PRXY,2,0.23
MP,MU,3,0.0
R,1,,,0.1

LSEL,S,LOC,X,0
LSEL,R,LOC,Y,air_gap,air_gap+beam_h
```

```
DL,all,,all,0

NLGEOM,1
OUTRES,ALL,ALL
EQSLV,SPAR
/GST,OFF

PHYSICS,WRITE,struct
PHYSICS,CLEAR

/prep7
ET,1,PLANE121
ET,2,0
ET,3,0
ET,4,0
EMUNIT,EPZRO,8.854E-06
MP,PERX,1,1

CMSEL,S,TE_L
DL,all,,VOLT,5
CMSEL,S,BE_L
DL,all,,VOLT,0
alls

PHYSICS,WRITE,elect
ESSOLV,'elect','struct',2,0,'GAP_A',,0.5E-02,0.5E-02,1
PHYSICS,READ,elect
/POST1
SET,LAST
PLNSOL, EF, SUM

/PREP7
PHYSICS,READ,struct
UPCOORD, -1
/DSCALE,,1
/POST1
SET, LAST
PLDISP, 2
```